Energy Transfer in Lanthanide-based Nanomaterial

Ilias Halimi

A thesis submitted in partial fulfillment of the requirements for the
Master's degree in science

Department of Chemistry and Biomolecular Sciences
Faculty of Science
University of Ottawa

To my family

Abstract

The respective fields of lanthanide-based nanoparticles and microwave-assisted synthesis are well established, but still ongoing, topics of research. Yet, there has been scarce attempts to join these areas of research together. The first part of the thesis presented here is the result of an effort to develop the very first phase-selective, microwave-assisted synthesis of small (sub-10 nm) and ultrasmall (sub-5 nm) photoluminescent $NaGdF_4:Yb^{3+}(20\%),X^{3+}$-based nanoparticles (X= Er, Tm). The choice of these lanthanide ions is important, as it endows the nanoparticles with the capacity to undergo upconversion and downshifting, two optical processes that allow for visible and near-infrared emission upon near-infrared excitation. The approach described here focuses on the precursor chemistry to control the size, the crystalline phase, and therewith the optical properties of $NaGdF_4:Yb^{3+}(20\%),Er^{3+}(2\%)$ nanoparticles. Furthermore, the precursor-dependent growth mechanism was investigated as a function of the microwave-assisted reaction temperature and time. Upconverting nanoparticles are well known for their long photoluminescent lifetime and as such, are often used to transfer energy to energy acceptor-like fluorescence dyes and other nanomaterials. Little work has been done on a hybrid system made of upconverting nanoparticles and inorganic lanthanide complexes. To address this, the second part of the work presented here describes a straightforward method to prepare a hybrid system containing $NaGdF_4:Yb^{3+}(20\%),Tm^{3+}(0.5\%)$ nanoparticles and either $[Tb_2(bpm)(tfaa^-)_6]$ or $[Eu_2(bpm)(tfaa^-)_6]$ complexes. The optical behavior of the hybrid system was assessed with steady-state and lifetime analysis. Furthermore, this is the first report of hyperspectral imaging used to characterize energy transfer process in thin film. The last part of this thesis describes some strategies to modify the surface of $NaGdF_4:Yb^{3+}(20\%),Tm^{3+}(0.5\%)$ nanoparticles, so they become water-dispersible. Furthermore, the effect of the aqueous solvents on the photoluminescence is also described.

Table of Content

List of Figures

List of Tables

Abbreviations

Ac^-	Acetate
Bpm	2,2-bipyrimidine
DRS	Diffuse reflectance spectroscopy
EDX	Energy dispersive X-ray
FTIR	Fourier-transform infrared spectroscopy
G/R	Green-to-red ratio
Ln	Lanthanide
$[Ln(Ac)_3]$	Lanthanide acetate
$[Ln_2]$	Lanthanide complex
$[Ln(OA)_3]$	Lanthanide oleate
$[Ln(TFA)_3]$	Lanthanide trifluoroacetate
NPs	Nanoparticles
NIR	Near-infrared
ODE	1-octadecene
OA^-	Oleate
OA	Oleic acid
OAm	Oleylamine
PAA	Polyacrylic acid
PL	Photoluminescence
PEG	Polyethylene glycol
SEM	Scanning electron microscopy
NaAc	Sodium acetate
NaTFA	Sodium trifluoroacetate
NaOA	Sodium oleate
TEOS	Tetraethyl orthosilicate
TGA	Thermogravimetric analysis
TEM	Transmission electron microscopy
TFA^-	Trifluoroacetate
TFA	Trifluoracetic acid

$tfaa^-$	1,1,1-trifluoroacetale acetonate
UV	Ultraviolet
UC	Upconversion
UCNPs	Upconverting nanoparticles
XRD	X-ray diffraction

Contributions

This thesis is mostly based on two research papers:

i) Halimi, I.; Martinazzo Rodrigues, E.; Maurizio, S. L.; Sun, T.; Grewal, M.; Boase, E. M.; Liu, N.; Marin, R.; Hemmer, E. Pick Your Precursor! Tailoring Size and Crystal Phase of Microwave-Synthesized Sub-10 Nm Upconverting Nanoparticles. *J. Mater. Chem. C* **2019**. This work is described in chapter 4 of this thesis.

ii) Marin, R.; Halimi, I.; Errulat, D.; Mazouzi, Y.; Lucchini, G.; Speghini, A.; Murugesu, M.; Hemmer, E. Harnessing the Synergy between Upconverting Nanoparticles and Lanthanide Complexes in a Multiwavelength-Responsive Hybrid System. *ACS Photonics* **2019**, *6* (2), 436–445. This work is described in chapter 5 of this thesis.

My contribution to the first paper was on the preparation of NPs and part of the subsequent steady-state PL and XRD analysis. My contribution to the second paper was on the synthesis of the NPs and the XRD and part of the PL (solid-state) analysis of the NPs. I further contributed to the writing of both manuscripts, especially Halimi *et al., J. Mater. Chem. C* **2019**. Chapter 6 is based on non-published results, and I was responsible for the preparation of the NPs, their surface modifications and all subsequent FTIR and PL analysis.

Dr. Emille M. Rodrigues contributed to the paper i) through NP synthesis as well as the subsequent part of the steady-state PL, TEM and XRD analysis. She courtesy provided several figures shown in this document and was one of the main co-authors of paper i). Nan Liu's contribution to paper i) was on the development of the protocol for cubic-phase NPs. She also helped the preparation of core/shell architectures, together with Manjot Grewal and Tina Sun. Steven Maurizio contributed

through preliminary work, demonstrating the importance of the 3:1 Na^{+}-to-Ln^{3+} ion ratio, while Emma M. Boase helped with the establishment of the [$Ln(OA)_3$] route.

Dr. Riccardo Marin contributed to the paper ii) through the preparation of the hybrid system, as well as the steady-state PL (solid-state and solution), absorbance spectroscopy, profilometry, SEM, and TEM. He courtesy provided several figures shown in this document and was the main writer of the paper ii). Furthermore, he acquired the TEM data presented in chapter 6. Dylan Errulat, from the Murugesu group at uOttawa, supplied the [Ln_2] used in paper ii).

Dr. Eva Hemmer helped through TEM analysis of the NPs in both papers as well as the excitation spectroscopy of the [Ln_2] in paper ii). She guided and led the writing of both manuscripts.

Acknowledgments

I am grateful to Dr. Eva Hemmer, Dr. Emille M. Rodrigues, and Dr. Riccardo Marin for their help, support, and training during the past two years, as well as for providing several figures used in this thesis. Furthermore, I would like to thank my colleagues Nan Liu, Nikita Panov and Fadi Oussta for their support and help. I want to extend my gratitude to the current and former members of the Hemmer group for their support: Nathaniel Leslie, Kinna Zhao, Steven Mauricio, Emma M. Boase, Camille Laot, Dr. Isabel Gessner, Itzel Lopez, Manjot Grewal, Nelson Rutajoga, and Tina Sun. Last but not least, I would like to thank Dr. Jeffrey Ovens for helping with XRD characterization, Dr. Juan Scaiano for providing access to the excitation spectrofluorometer (Varian Cary Eclipse), Dr. Jaclyn Brusso for providing access to UV-vis absorbance and DRS spectrometry (Cary Varian 5000), Dr. Javier Giorgi for allowing us to use the KBr bench press in his lab, as well as Dr. Adolfo Speghini and Giacomo Lucchini for solid-state lifetime measurements performed on the hybrid system

1. Introduction

Lanthanides (Ln) are a group of 15 heavy elements that fall under the qualification "rare earth," a series of chemical elements in the periodic table that also includes Y and Sc.[1] In their trivalent state, Ln^{3+}, they possess uncommon optical properties, *e.g.*, upconversion (UC).[2] Based on their optical properties, there is a large range of applications, ranging from the security sector to laser-generating crystals.[3,4] This diverse portfolio has resulted in numerous studies on the preparation of Ln-based materials. Since the beginning of this millennium, there has been a push for nanotechnology, which has impacted the Ln-based material field as well. In this context, Ln-based nanoparticles (NPs) are considered as candidates for various applications, such as photocatalysis, optoelectronics, optogenetics and bioimaging.[5–8] Thus, the development and improvement of fast and reliable synthesis strategies for luminescent Ln-based NPs remains an ongoing research topic. It is achievable by understanding the fundamental chemistry process that takes place during the synthesis. Furthermore, implementing Ln-based NPs in optoelectronics or as bioprobes is a currently very active research field. In this context, focus is set, for instance, on energy transfer (ET) between the NPs – acting as an energy donor – and another moiety acting as energy acceptor.[9,10] There is a need in that field for a better understanding of the mechanism and the nature of the ET, so that more efficient devices and bioprobes can be developed.[11]

1.1 Optical behavior of lanthanide-based materials

1.1.1 Theory of lanthanide trivalent cation (Ln^{3+}) photoluminescence (PL)

The optical behavior of Ln-based materials, nanoscale or not, is derived from their electronic transitions within the 4f orbital-based energy levels, which are shown in Figure 1.[12]

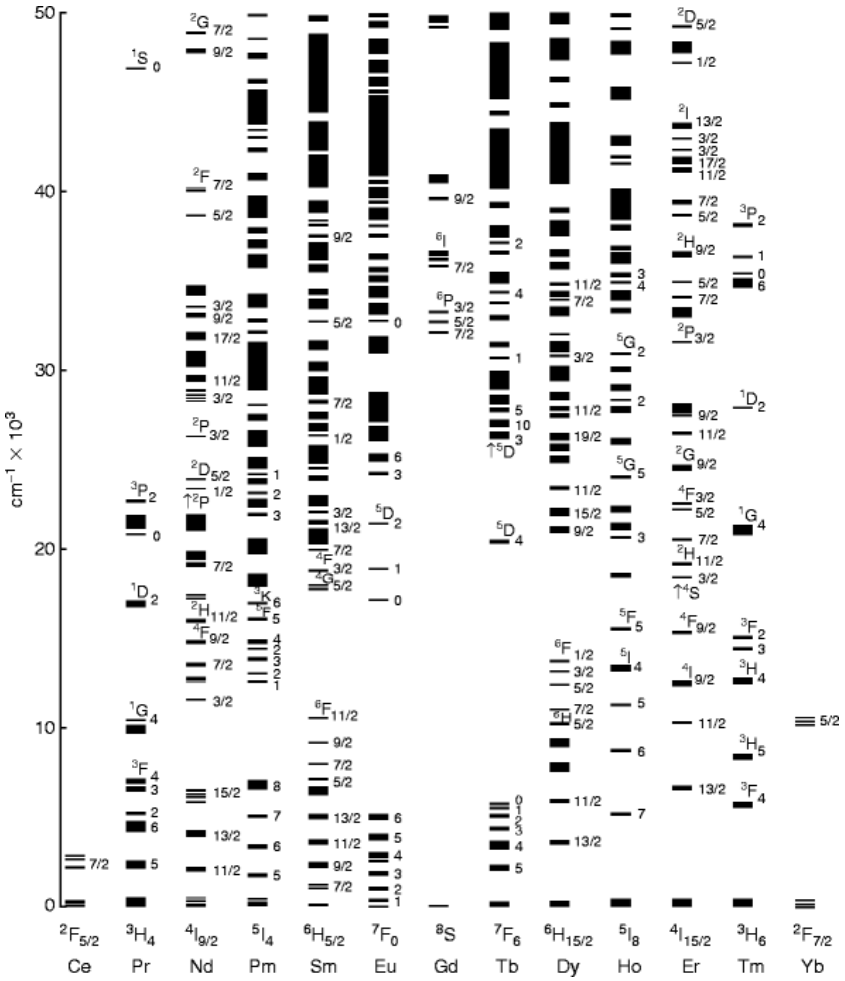

Figure 1. Dieke diagram for trivalent lanthanide (Ln^{3+}) ions in LaF_3. Reprinted with permission from Springer Nature Customer Service Centre GmbH: Springer Nature Physics of Light Emission from Rare-Earth Doped Phosphors by R. Withnall and J. Silver [COPYRIGHT] (2019).[13]

Upconversion (UC)

f-f transitions are forbidden by the Laporte transition rule, which results in low molar absorptivity of Ln^{3+} ions.[14] Usually, if the Ln^{3+} ion is placed in a low-symmetry environment (like doping in an asymmetric crystal), the Laporte selection rule can be bypassed.[15] Furthermore, these ions usually exhibit long photoluminescent lifetimes, large Stokes / anti-Stokes shifts, and multiple narrow excitation and emission bands.[16] Unlike fluorescent dyes and quantum dot, they do not photobleach or photoblink.[17] Depending on which Ln^{3+} ions are doped into the suitable crystalline

host; it is possible to observe photoluminescence from at least one of the following optical phenomena: upconversion (UC) and downshifting (DS).[2,18]

UC was first proposed by Bloembergen in 1959 and experimentally demonstrated in 1966 by Auzel using the Yb^{3+}/Er^{3+} ion dopant system.[19,20] The UC process is commonly defined as a nonlinear optical process that converts multiple lower-energy photons into a single higher-energy photon. There are various mechanisms behind the UC process: excited state absorption (ESA), energy transfer upconversion (ETU), cooperative upconversion (CUG), photon avalanche (PA) and energy migration upconversion (EMU), as seen in Figure 2.[16,13]

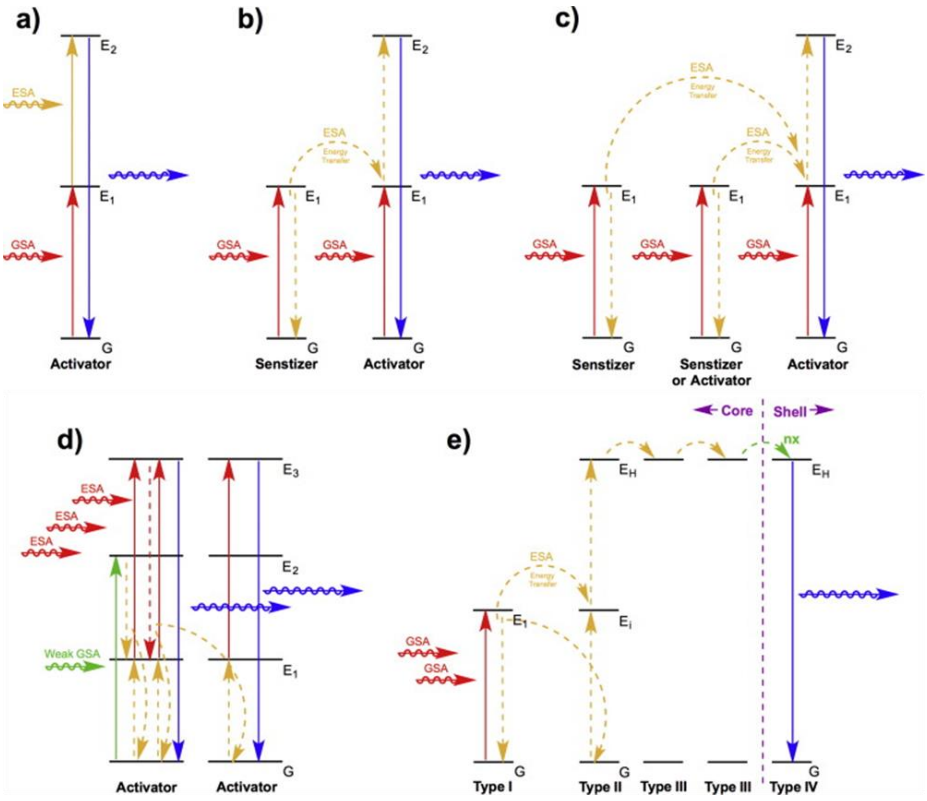

Figure 2. Schematic representation of UC processes: a) excited state absorption (ESA), b) energy transfer upconversion (ETU), c) cooperative upconversion CUC), d) photon avalanche (PA), and e) energy migration upconversion (EMU). E_i (i=1,2,3) represents an excited state. GSA stands for ground state absorption. Line colors are not indicative of wavelengths. Reprinted from *Analytica Chimica Acta*, 832, MV DaCosta, S Doughan, Y Han, UJ Krull, **Lanthanide upconversion nanoparticles and applications in bioassays and bioimaging: A review**, 1-33, Copyright (2019), with permission from **Elsevier**.[16]

ETU is often assumed to be the main mechanism responsible for the observed upconversion in Ln-based materials. In short, in this mechanism, a so-called sensitizer specie absorbs the excitation light and then transfers the energy to a so-called activator specie through a resonant (*i.e.*, non-radiative) process. If multiple energy transfer (ET) steps take place sequentially before the activator's radiative relaxation, then UC emission shall be observed. Yb^{3+} ions are chosen as sensitizers, due to their capacity to absorb near-infrared (NIR) light of around 980 nm, while Er^{3+} acts as the activator. Following absorption of a NIR photon, the promotion of Yb^{3+} from its ground level ($^2F_{7/2}$) to its sole excited level $^2F_{5/2}$ takes place (Figure 3a).[21] If Er^{3+} is in close enough proximity to the excited Yb^{3+}, it receives energy from the Yb^{3+} through resonant energy transfer, which causes excitation of the Er^{3+} from its ground level ($^4I_{15/2}$) to its $^4I_{11/2}$ excited energy level. Subsequently, following the absorption of a second NIR photon by the same Yb^{3+} ion, energy is supplied again to the already excited Er^{3+} ion. The result is the promotion of the electrons to the higher $^4F_{7/2}$ Er^{3+} energy level. Afterward, non-radiative relaxation can occur to either the $^2H_{11/2}$, $^4S_{3/2}$ or $^4F_{9/2}$ Er^{3+} levels. The f-f transitions $^2H_{11/2} \rightarrow {}^4I_{15/2}$, $^4S_{3/2} \rightarrow {}^4I_{15/2}$, $^4F_{9/2} \rightarrow {}^4I_{15/2}$ are responsible for the visible emission at 520 nm, 550 nm and 650 nm, respectively (Figure 3b). Alternativity, another ET from an excited Yb^{3+}ion to the twice-excited Er^{3+}, can occur, resulting in electron promotion to the Er^{3+} $^2H_{9/2}$ level. The subsequent f-f transition $^2H_{11/2} \rightarrow {}^4I_{15/2}$ is responsible for the – typically weak – emission around 410 nm.[12,22] Strictly speaking, Er^{3+} is capable of self-upconversion upon excitation with 980 nm, but this process is rather inefficient due to the ion's small absorption cross section, roughly $2.5 \cdot 10^{-20}$ cm^{-2}.[12,23] Yb^{3+} has an absorption cross section of $25 \cdot 10^{-20}$ cm^{-2}.[23] Thus, co-doping with Yb^{3+} is a common strategy to enhance photoluminescence, leading to the ETU prevalence.[22] Other often used activators are Tm^{3+} and Ho^{3+}.[24]

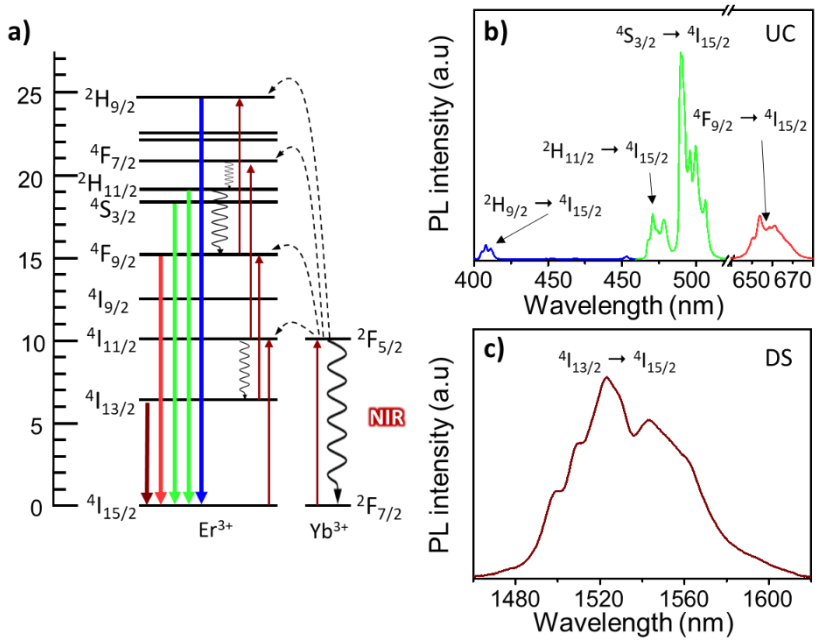

Figure 3. UC and DS as found for Er^{3+}/Yb^{3+} pair under NIR (980 nm) excitation. a) Energy scheme of the UC and DS processes. Excitation and emission processes (solid upward and downward arrows), non-radiative processes (solid downward wavy arrows), ET mechanisms within each moiety (dotted arrows). Characteristic b) visible (upconverted) and c) NIR (downshifted) emission spectra for the Yb^{3+}/Er^{3+} ion pair.

As Ln^{3+} photoluminescence is dependent on f-f transitions, changing the activator will immensely affect the emission spectra, based on the Ln^{3+}-specific energy scheme (Figure 1). The here described upconversion process also happens in nanoscale materials. NPs capable of upconversion are often referred as upconverting nanoparticles (UCNPs).

Downshifting (DS)

DS is a more classical (Stokes-shifted optical process, which corresponds to the absorption of one higher energy photon and the subsequent emission of one lower energy photon. It is observed in single ion system (*e.g.*, Eu^{3+} under UV excitation, Nd^{3+} under 808 nm excitation, Er^{3+} under 1550 nm excitation) and in co-doped systems (*e.g.*, Yb^{3+}/Er^{3+} under 980 nm, Figure 3a and Figure 3c).[25–28] In the latter, under NIR excitation, resonant energy transfer will occur from the Yb^{3+} excited state to the Er^{3+} $^4I_{11/2}$ excited state. Subsequently, non-radiative relaxation takes place from the

$^4I_{11/2}$ to the $^4I_{13/2}$ levels of Er^{3+}. The subsequent f-f transition $^4I_{13/2} \rightarrow {}^4I_{15/2}$ will occur afterward, which results in an emission centered at 1520 nm, falling in the NIR spectral region (Figure 3c).[29]

As mentioned above, the f-f transitions responsible for Ln^{3+}-based photoluminescence are forbidden by the Laporte selection rule. Consequently, to enhance the brightness of UCNPs, or Ln-based NPs in general, a few criteria must be met: i) the Ln^{3+} ions should be in a low-symmetry environment, ii) the host lattice should have a low phonon energy to reduce phonon-assisted relaxation, iii) quenching induced by surface defects and solvents must be minimized, and iv) the molar absorption cross-section should be improved as much as possible.[16,30,31] Criteria i) and ii) are achieved by choosing the proper crystalline host, but this shall be covered in more detail in section 1.2. Criterium iii) – of particular importance at the nanoscale – is addressed by growing a protective shell around the NPs to heal the surface and to prevent direct interaction with the solvent molecules, increasing photoluminescence emission and lifetime.[32] It shall be discussed in more detail in section 1.3. Increasing the amount of sensitizer (*e.g.*, Yb^{3+}) is a strategy to meet criterium iv), but this is a double edge sword. High doping levels of Yb^{3+} are known to facilitate surface-induced quenching, thus potentially nullifying any photoluminescence gain.[33] Furthermore, it can affect the phase purity of the NPs, but this will explain in more details in section 1.2.

1.1.2 Energy transfer (ET) theory

An energy transfer can only occur if a pair of energy donor and acceptor is present. The energy donor must absorb the light from the excitation source. Once it is in its excited state, it can transfer the energy to the acceptor.[16] There are three possible mechanisms behind the transfer: a) Dexter energy transfer, b) Förster resonance energy transfer (FRET), and c) energy transfer based on emission/re-absorption (Figure 4a-c). Dexter energy transfer is based on electron exchange between the excited donor and the acceptor in its ground state (Figure 4a).[34,35]

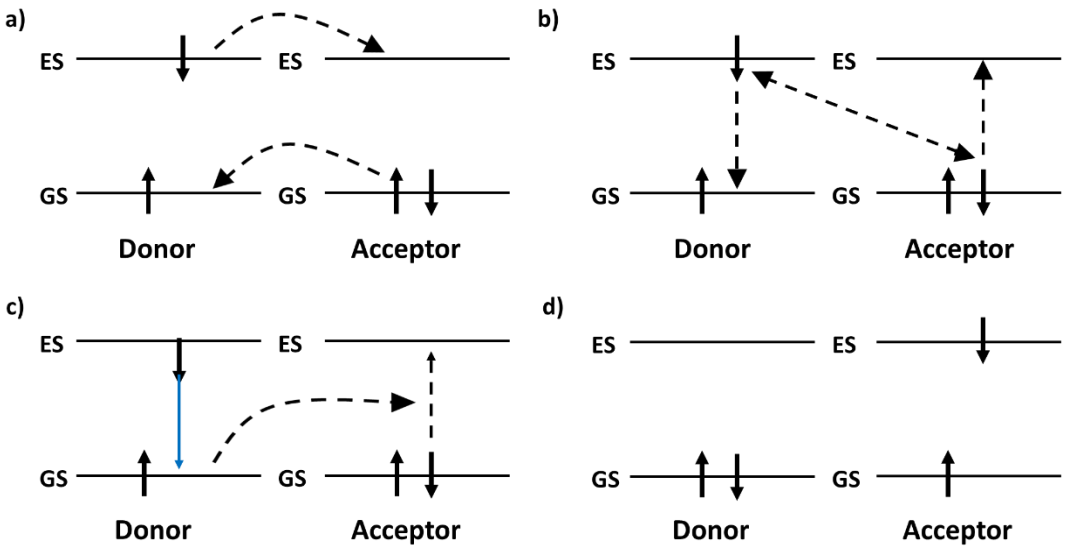

Figure 4. Common ET mechanisms between donor and acceptor moieties: a) Dexter mechanism, b) FRET mechanism, and c) emission and re-adsorption, resulting in d) relaxation of the donor and excitation of the acceptor.

FRET is based on dipole-dipole interaction between the excited donor and the ground state acceptor (Figure 4b).[36,37] These two pathways are non-radiative (resonant) and thus will decrease the donor excited state lifetime of the energy donor.[38]

Their efficiencies are also extremely distance sensitive, up to a few Å (Dexter) or nm (FRET).[36,39] Emission and re-absorption processes are observed when the acceptor absorbs the photoluminescence generated by the donor. It is a radiative process that does not decrease the excited state lifetime of the donor and it is less distance sensitive than FRET.[40] No matter the mechanism, the result of the energy transfer is the quenching of the donor emission and the excitation of the acceptor (Figure 4d). In some cases, the acceptor will emit following the energy transfer. Non-radiative energy transfers are also happening within UCNPs, where the sensitizer serves as the energy donor while the activator act as an energy acceptor. UCNPs themselves can be used as energy donor, with fluorescent dyes, quantum dots and plasmonic NPs.[9,10,41–43] Fewer

attention has been paid to energy transfers between Ln-based NPs and Ln-based complexes, despite the overall potential as sensing agent.[11]

1.2 Lanthanide-based nanoparticles

1.2.1 Choice of the crystalline host material

As briefly mentioned above, the crystalline host is responsible for the symmetry around the Ln^{3+} ions. Moreover, its phonon energy has to be taken into account when aiming for bright emitters.[44,45] Thus, selecting the right crystalline host is of great importance when addressing requirements i) and ii) described on page 11. Various host materials have been used for Ln-based NPs, such as lanthanide sesquioxide (Ln_2O_3), trifluoride (LnF_3), sodium tetrafluoride ($NaLnF_4$), phosphate ($LnPO_4$), yttrium aluminum oxide garnet (YAl_5O_{12}), vanadate ($LnVO_4$) and oxysulfide (Ln_2O_2S).[46–51] $NaLnF_4$ offers low symmetry and low phonon energy (around 400 cm^{-1}), but it is also a stable material that won't completely degrade if dispersed in organic solutions or aqueous solvent (as for instance $LnCl_3$, which has even lower phonon energy around 250 cm^{-1}).[16,52,53] For these reasons, $NaLnF_4$ was chosen among the crystal hosts listed above as the target for material synthesis described in this thesis.

Within the $NaLnF_4$ family, the most used and investigated crystalline hosts for UCNPs are $NaYF_4$ and $NaGdF_4$.[44,54] These materials crystallize in two different polymorphs: the hexagonal (β) phase and the cubic (α) phase (Figure 5).[55]

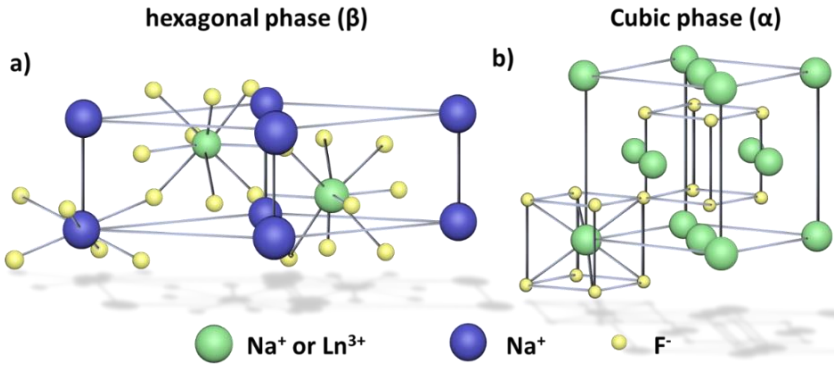

Figure 5. Schematic of the two crystalline phases of $NaLnF_4$. a) the hexagonal lattice b) the cubic lattice. The hexagonal phase has two types of sublattice sites: one for Na^+ and one for Ln^{3+}. The coordination number around the Ln^{3+} ions is 9. In the cubic phase, there is one type of sublattice site. Na^+ and Ln^{3+} are randomly distributed across the sublattice, and they have the same coordination number, 8. Redrawn from reference [56].

The difference between these polymorphs comes from the lattice positions assigned to cations. In the hexagonal phase, the Na^+ has two selected sublattice sites, while the Ln^{3+} ions only have one available sublattice site (Figure 5a). With the cubic phase, there are no assigned sublattice sites, and the Ln^{3+} and Na^+ are randomly distributed across the crystal on the cations sites (Figure 5b).[56] Since the hexagonal phase offers the lower symmetry among the two polymorphs, it is considered as the more efficient host material for upconversion processes and, thus, typically preferred for optical-based applications.[16,44] As mentioned in section 1.1, Yb^{3+} and Er^{3+}, Tm^{3+} or Ho^{3+} must be doped into the $NaGdF_4$ to obtain UCNPs. However, these ions, along with Lu^{3+}, will push $NaGdF_4$ and $NaYF_4$ toward their cubic phase if present at high doping level. Usually, the doping level of these ions is around 20% for Yb^{3+}, 2% for $Er^{3+,}$ and 0.5% for Tm^{3+}.[57–59] It is not only based on the phase purity requirement; it is also optimized to get the highest upconversion photoluminescence. As mentioned in section 1.1, high Yb^{3+} doping level can increase the molar absorption coefficient of the UCNPs, but due to Yb^{3+} preference for the cubic phase over the hexagonal phase (sought after for optical application), it is not a suitable strategy for solving this criterium.

Nonetheless, the cubic phase should not be discarded. Undoped $NaGdF_4$ NPs are promising magnetic resonance imaging (MRI) contrast agent.[60] Recent publication by the Hemmer group showed that the undoped α-$NaGdF_4$ NPs performed better as contrast agent for MRI than the hexagonal analogue.[52] Thus, $NaGdF_4$-based NPs are potential candidates for multifunctional (optical and magnetic) bioimaging.[61] As such, there is a need to develop a rapid and phase-selective, synthesis routes to upconverting and NIR-emitting $NaGdF_4$:Yb^{3+},X^{3+} NPs (X^{3+} = Er^{3+},Tm^{3+}).

1.2.2 Biomedical applications of lanthanide-based nanoparticles

The UCNPs described above will emit under NIR (980 nm) excitation and are considered as candidates for bioimaging and photodynamic therapeutic agents.[16,62] The NIR spectral region extends from 700 nm to 1800 nm and it overlaps with the so-called "biological optical window", shown in Figure 6.[63]

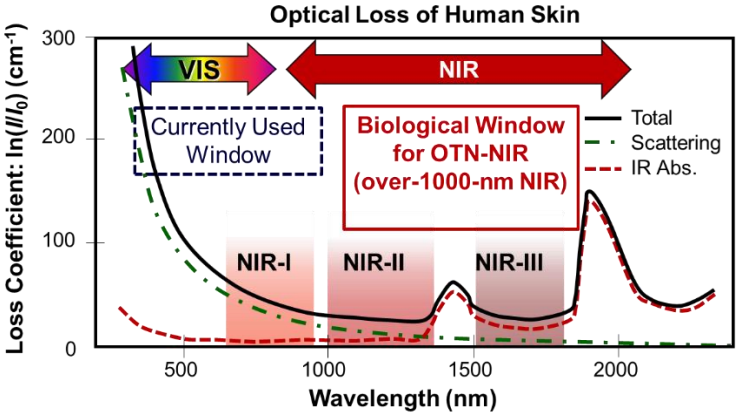

Figure 6. Absorption spectrum of human skin. NIR-I corresponds to the 700-950 nm spectral region, NIR-II to 1000-1350 nm, and NIR-III to 1550-1870 nm.[64] Reprinted from Ref [63] with permission from The Royal Society of Chemistry.

Excitation wavelengths within the NIR-I (700-950 nm) region suffer less scattering and generate less autofluorescence on biological tissue than visible or UV irradiation.[8,16] Consequently, it

penetrates more deeply into (human) biological tissue than visible or UV light. As such, it is possible to excite UCNPs within a biological tissue.[29] To study $NaGdF_4:Yb^{3+}(20\%),X^{3+}$ ($X=Er^{3+}$, Tm^{3+}), a 980 nm laser is usually employed. However, water can absorb at this wavelength and so instead, it has been recommended to use a 915 nm laser (with Yb^{3+} as a sensitizer) or a 808 nm laser (Nd^{3+} as a sensitizer).[65,66] While the NIR-triggered upconverted visible and UV emission will not be detectable directly through a thick biological tissue, it has been demonstrated that UCNPs can be employed in photodynamic therapy.[66] Herein, radical species are generated inside cancerous cells through the activation of a photosensitizer dye grafted on the UCNPs.[66] However, the Ln-based NPs' NIR emission can be used for imaging in the NIR-II and NIR-III windows (Figure 6).[67] As such, Ln-based NPs are promising candidates as diagnostic and therapeutic agents for treating various diseases, like, *e.g.* cancer. Furthermore, the size of the NPs should remain small, close to the scale of intracellular features and other biomolecules. Ensuring this size regime allows the application of $NaLnF_4$ NPs in nanomedicine and the assessment of nano-bio-interactions.[30,68–70] Many of these applications – in particular in bioassays – are FRET-based processes using Ln-based NPs as energy donor and an energy acceptor, such as fluorescent dyes or plasmonic NPs.[10,11,41,42]

1.3 Conventional synthesis approaches toward lanthanide-based nanoparticles

Some of the most popular synthesis methods for Ln-based NPs include thermal decomposition, hydrothermal, and precipitation methods.[71–74] Hydrothermal and precipitation are performed in aqueous solvents, while thermal decomposition approach requires the use of high boiling point organic solvents and takes place at high temperature (above 300 °C). Nonetheless, thermal decomposition is usually preferred for the synthesis

of $NaLnF_4$ NPs, as it offers small NPs with more homogeneous morphology.[71] The groups of Mai and Capobianco were the first to demonstrate the potential and versatility of thermal decomposition with lanthanide trifluoroacetate precursors ($[Ln(TFA)_3]$).[55,75] These precursors are decomposed in high boiling point organic solvents (*e.g.*, oleic acid, 1-octadecene, and oleylamine) at a temperature above 300°C under an inert atmosphere (N_2 or Ar), which leads to nucleation and growth of the NPs.[55,75] Typically, experimental protocols for the thermal decomposition require the dissolution of the precursors in the high boiling point organic solvents before heating of the reaction mixture to the target temperature. Alternatively, the precursor solution (in high boiling point organic solvents) can be added dropwise to a hot mixture of high boiling point solvents. The latter route is often referred to as hot injection method. Furthermore, thermal decomposition is sometimes referred to as co-precipitation when $[Ln(Cl)_3]$ is used as precursor (not be confused with precipitations in aqueous solution).[76] Thermal decomposition follows the La Mer principle, which states that to obtain a narrow particle size distribution, the growth process should only follow after the nucleation process is finished.[77]

The thermal decomposition approach can be adapted to grow a protective $NaLnF_4$-based shell around the core, resulting in the so-called core/shell architectures. As mentioned in section 1.2, quenching induced by surface defects and solvents is a major reason for photoluminescent loss. The protective shell will heal the surface and block the solvent, which in turn increases the brightness and lifetime.[32] A common procedure for shell growth consists of hot-injecting the shell precursor solution right after the core has been grown (without any washing steps of the NPs).[33] Alternatively, the core-only NPs can be washed, followed by redispersion in the shell precursor solution and subsequent heat treatment.[78]

Furthermore, it is possible to grow more complex core/shell architecture where different Ln^{3+} ions are doped into the different layers of the NPs. The growth of multiple shells is a viable strategy to tune the excitation and emission of the NPs.[57,67] At last, it is also possible to grow shell through the Ostwald ripening in which a mixture of small and large NPs is mixed heated to high temperature, which has been often reported in the literature.[79] The small NPs will dissolve and their content will precipitate on the surface of the large NPs, forming the shell.[80]

Beside $[Ln(TFA)_3]$ and $[Ln(Cl)_3]$, other precursors have been used to carry out the thermal decomposition approach. The preparation of $[Ln(TFA)_3]$ is time-consuming and expensive (around 6.4 CAD to make 1 mmol of $[Ln(TFA)_3]$, not including energy and equipment). An example of alternative precursors are lanthanide oleates, $[Ln(OA)_3]$, which can be used to grow UCNPs of both polymorphs in the sub-10 nm range.[80,81] Lanthanide acetate, $[Ln(Ac)_3]$, has also been used to synthesize $NaLnF_4$ NPs.[78,82] This precursor is directly available from chemical suppliers and is less expensive than its trifluoroacetate counterpart (1.17 CAD per 1 mmol of $Gd(Ac)_3 \cdot xH_2O$).[i]

While the versatility of the thermal decomposition route has been more than demonstrated, it is not a perfect method. It is based on convection heating (heat mantle or oil bath), and it is a relatively time-consuming approach (a few hours).[30,83] Given the interest and demand in Ln-NPs of controlled morphology, size, and crystalline phase, it is important to fasten and ease the synthesis of UCNPs and the shell growth process.

[i] Based on Alfa Aesar price on 2019-01-11

1.4 Microwave-assisted synthesis of lanthanide-based nanoparticles

The groups of Gedye and Giguere were the first to describe a microwave-assisted synthesis protocol in 1986, albeit for organic reactions.[84,85] The principle behind the non-convectional heating mechanism applied in this approach is relatively simple: microwaves can interact with the dipole of a polar molecule (dipole polarization) or the charge on an ionic molecule or ion (ionic conduction). In the event of dipole polarization, the oscillation of the microwave causes a realignment of the dipoles, which makes the polar molecule move. In turn, there is molecular friction and dielectric loss, which generates heat.[86] By continuously irradiating the solution, enough energy to heat the solution is produced (Figure 7a).

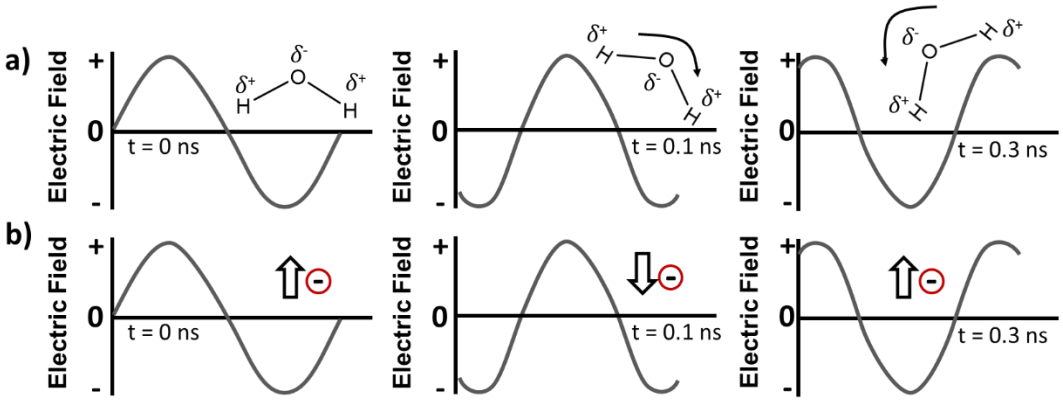

Figure 7. The mechanisms behind the heating caused by microwave irradiation: a) Dipolar polarization with water as example and b) ionic conduction. Redrawn from Ref[87] with permission from The Royal Society of Chemistry.

Ionic conduction works similarly, but the charged molecule or ion can follow the microwave's oscillation more quickly than a polar molecule and is, thus, releasing more heat (Figure 7b).

Generally speaking, the microwave efficiency of a given substance, which is the capacity to transform microwave energy into heat, is based on a loss factor called tanδ. In mathematical term, it corresponds to:

$$tan\delta = \frac{\varepsilon''}{\varepsilon'} \qquad (1)$$

where ε'' is the dielectric loss (*i.e.,* heat generated by the microwave irradiation) and ε' is the dielectric constant (*i.e.,* the polarization susceptibility under microwave radiation) of the substance (*e.g.,* molecule, ion, solvent or solute).[88,89] A tanδ factor above 0.5 is the threshold for high capacity microwave solvents.

The versatility of a microwave reactor has been demonstrated throughout the years. It has been used to synthesize organic and inorganic products. Examples of nanomaterial prepared through microwave-assisted synthesis include carbon dots, plasmonic NPs, and quantum dots.[90–92] Microwave-assisted approaches are expected to shorten the reaction time, suppress certain side products, improve the homogeneity of the NP size distribution, and batch-to-batch reproducibility, which are common issues with conventional synthesis.[87] As such, it has also attracted interest for the synthesis of $NaLnF_4$ NPs. The first example of microwaved-assisted synthesis of UCNPs was reported by H.Q-Wang *et al.,* 10 years ago.[93] The protocol used $[Ln(TFA)_3]$ as precursor, and yielded 11-nm sized α-$NaGdF_4$:Yb^{3+}(20%),Er^{3+}(2%) NPs. Following this publication, Quintanilla *et al.* reported a microwave-assisted shell growth procedure for α-$NaGdF_4$:Yb^{3+}(20%),Er^{3+}(2%) and α-$NaGdF_4$:Yb^{3+}(20%),Tm^{3+}(0.5%) NPs.[94] In short, the $[Ln(TFA)_3]$ precursors were injected in a microwave vessel after the core step and were microwaved again, resulting in core/shell/shell UCNPs that were still in the sub-10 nm realm.[94] However, these examples with $[Ln(TFA)_3]$ are only adapted for the synthesis of α-$NaLnF_4$ NPs. Guzzetta *et al.* achieved the microwave-assisted synthesis of β-$NaGdF_4$:Yb^{3+}(20%),Er^{3+}(2%) NPs in aqueous solvents (water/benzyl alcohol) within 10 min.[95] The downside of this approach was the relatively large dimensions (50 nm) of the UCNPs. On the plus side, they were immediately water-dispersible, which is required for any

bioapplications.[16,62] The microwave-assisted synthesis of sub-10 nm β-$NaGdF_4$:Yb^{3+}(20%),Er^{3+}(2%) NPs was reported by Amouroux *et al.* earlier this year.[31] Using [$Ln(OA)_3$] as precursors resulted in small (sub-10 nm) and even ultrasmall (sub 5-nm) β-UCNPs. The authors highlighted that their approach yielded highly homogeneous NPs in a significantly shorter time when compared to the thermal decomposition approach.[31]

While these are promising results, many of the reported protocols either lack phase-selectivity or do not offer UCNPs within the sub-10 nm region. The Hemmer group (Liu *et al.*) reported a phase-selective microwaved-assisted synthesis of sub-10 nm undoped $NaGdF_4$ NPs.[52] Yet, similar control over the crystalline phase and size of upconverting and NIR emitting $NaLnF_4$-based NPs remained an ongoing topic of research, being addressed in this thesis.

1.5 Hyperspectral imaging

Hyperspectral imaging is an imaging technology developed to record spectral information over a specific area.[96] Originally, it was developed for agricultural, astronomical, and environmental purposes,[97] while it only recently attracted attention as an alternative method for the characterization for, *e.g.,* nanomaterial distribution in biological samples.[98] The main advantage of hyperspectral imaging over photoluminescence spectroscopy and microscopy is that it combines spatial distribution (x-and y-axis) with spectral information. A hyperspectral image (or cube) consists of a 2D spatial map with the photoluminescence or scattering intensity as the z-axis.[97,99] While the hyperspectral microscope does not allow to distinguish between two sub-10 nm NPs spatially due to the Rayleigh constraint, it can monitor their distribution, for instance, within a polymer matrix, a thin film, human cells or fish embryos (Figure 8).[100–102] Examples of

hyperspectral imaging with UCNPs in cells and biological tissues have been reported by the groups of Vetrone and Zvyagin.[67,103]

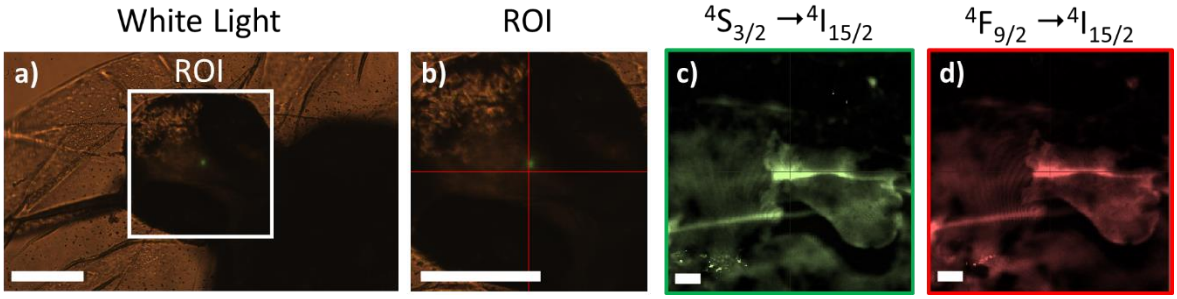

Figure 8. Analysis of β-$NaGdF_4$:Yb^{3+}(20%),Er^{3+}(2%)/$NaGdF_4$ (core/shell) NPs distribution in a zebra fish embryo. a) Micrograph of the fish head. b) Region of interest (ROI) for hyperspectral mapping. Spectral maps over the ROI for the upconverted green (550 nm) and red (650 nm) emission under NIR excitation. Courtesy of Dr. Emille M. Rodrigues. Scale bars are 100 μm for the micrographs and 20 μm for the spectral maps.

2 Objectives

As explained in the chapter 1, there have been reports of microwave-assisted synthesis of $NaLnF_4$-based UCNPs. However, these methods lack phase-selectivity. It is primordial to understand the growth mechanism in order to predict and to control the size and crystalline phase of the NPs correctly. Furthermore, the biomedical applications of UCNPs are derived from the optical properties. As such, it is important to investigate their behavior as an energy donor and as a PL agent in aqueous conditions.

The specific objectives of this thesis were as follow:

- Development of a phase-selective microwave-assisted synthesis route using $[Ln(TFA)_3]$ precursors to obtain cubic- and hexagonal-phase UCNPs. Investigation of the effect of precursor chemistry on size, crystalline phase, and optical properties by using the alternative precursors $[Ln(OA)_3]$ and $[Ln(AC)_3]$. Study of the growth mechanism of Ln-NPs derived from the three different precursors (Chapter 4)
- Development of a microwave-assisted shell growth procedure using $[Ln(TFA)_3]$ precursors, to enhance the PL of the UCNPs (Chapter 4).
- Preparation of a hybrid system containing both UCNPs and Ln-based complexes and investigations of the mechanism behind the energy transfer in the hybrid system (Chapter 5).
- Implementation of surface modifications on the UCNP surface to render them water-dispersible and assessment of their optical properties under aqueous conditions (Chapter 6).

3 Experimental

3.1 Chemicals

Gadolinium oxide (Gd_2O_3, 99.999%), ytterbium oxide (Yb_2O_3, 99.998%), erbium oxide (Er_2O_3, 99.99%), thulium oxide (Tm_2O_3, 99.997%), gadolinium chloride ($GdCl_3 \cdot 6H_2O$, 99.99%), ytterbium chloride ($YbCl_3 \cdot xH_2O$, 99.9%), erbium chloride ($ErCl_3 \cdot xH_2O$, 99.9%), gadolinium acetate ($Gd(CH_3CO_2)_3 \cdot xH_2O$, 99.9%), ytterbium acetate ($Yb(CH_3CO_2)_3 \cdot 4H_2O$, 99.9%), erbium acetate ($Er(CH_3CO_2)_3 \cdot xH_2O$, 99.9%), tetraethyl orthosilicate (TEOS, 98%) and potassium bromide (KBr, 99+%) were purchased from Alfa Aesar. Trifluoroacetic acid (CF_3COOH, TFA, 98%), sodium trifluoroacetate (CF_3COONa, NaTFA, 98%), sodium acetate (CH_3COONa, NaAc, 99%) oleic acid (OA, 90%), oleylamine (OAm, 70%), 1-octadecene (ODE, 90%), IGEPAL CO-520, polyacrylic acid sodium (PAA, Mw = 1800 g/mol), and ammonium fluoride (NH_4F, 98%) were purchased from Sigma Aldrich. Sodium oleate ($CH_3(CH_2)_7CH=CH(CH_2)_7COONa$, NaOA, 97%) was purchased from Tokyo Chemical Industry. α-NH_2-ω-COOH-polyethylene glycol (α-NH_2-ω-COOH-PEG, Mw = 805 g/mol) was obtained from Polymer Source Inc. Cyclohexane was purchased from Ward Natural Science. Toluene (99.8%), hydrochloric acid (HCl, 36.5-38%), ammonium hydroxide (NH_4OH, 28-30% NH_3), and chloroform (99.9%) were purchased from Fisher Scientific. Ethanol (99%) and hexane (analytical grade) were purchased from Commercial Alcohols and Fisher Chemicals, respectively. The lanthanide complexes, $[Ln_2(bpm)(tfaa)_6]$ ($[Ln_2]$, Ln= Tb^{3+} or Eu^{3+}), were synthesized by the Murugesu Group at the University of Ottawa using a published protocol.[104] All chemicals were used as received.

3.2 Microwave-assisted synthesis of lanthanide-based nanoparticles

3.2.1 [Ln(TFA)$_3$] route

For the microwave-assisted decomposition of [Ln(TFA)$_3$] precursors, a modified version of a previously reported protocol was followed.[40,94] In short, 2.5 mmol of [Ln(TFA)$_3$] precursor were prepared by dissolving 1.25 mmol of Ln_2O_3 in 10 mL of a 1:1 trifluoroacetic acid-H_2O mixture in a 50 mL three-neck round-bottom flask.[75] For example, the synthesis of $NaGdF_4$:Yb^{3+}(20%),Er^{3+}(2%) NPs requires 0.975 mmol of Gd_2O_3 (353.4 mg), 0.25 mmol of Yb_2O_3 (98.5 mg), and 0.025 mmol of Er_2O_3 (9.6 mg). The slurry was refluxed under vigorous stirring at 90-95 °C. After it turned completely clear, it was dried overnight at 60 °C and, if needed, stored at 4 °C before usage. Subsequently, for the synthesis of α-$NaLnF_4$-based NPs, 2.5 mmol of NaTFA (346.9 mg, resulting in a 1:1 Na^+-to-Ln^{3+} ion ratio) and 20 mL of a 2:1:1 ODE-OA-OAm mixture were added to the three-neck flask containing the precursor. Thus, the concentration of Ln^{3+} was 0.125 mol·L^{-1}. The solution was degassed at 100 °C for 30 min. A volume of 10 mL of this solution was transferred into a 35-mL microwave vessel using a dry glass syringe. After flushing with N_2 and sealing with a Teflon cap, the reaction vessel was inserted into a CEM Discover SP microwave reactor. The $NaLnF_4$ NPs were grown by subjecting the reaction solution to microwave radiation. Originally, the conditions were i) stirring at room temperature (1 min) followed by ii) rapid heating to T_1, iii) slow cooling (10 min) to a lower temperature T_2 and finally iv) rapid cooling to 50 °C (6 min). For step i), medium speed was used for the stirring, while all subsequent steps used the slow speed setting of the microwave. T_1 was 300 °C while T_2 was set to 230 °C (Figure 9, microwave conditions are shown in Table 1 on page 26).

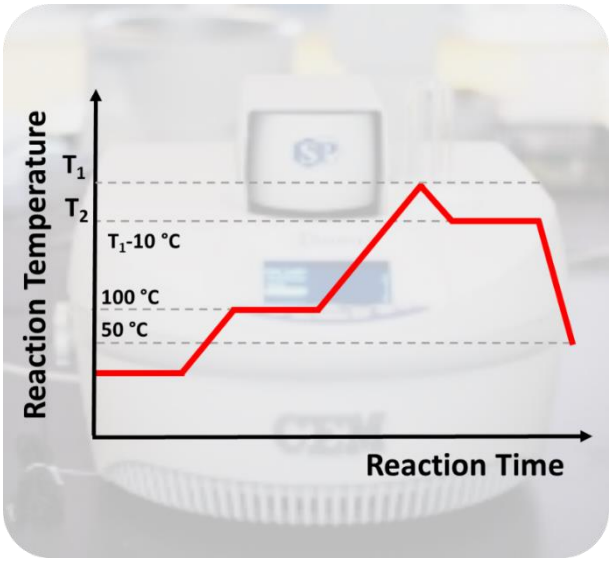

Figure 9. General scheme of the microwave-assisted synthesis of α- and β-$NaLnF_4$ NPs regardless of the precursor employed.

Table 1. Microwave conditions used for the synthesis of core-only Ln-NPs

Precursor	Crystalline Phase	Na^+-to-Ln^{3+} Ion Ratio	Ln^{3+} Concentration ($mol \cdot L^{-1}$)	T_1 (°C)	T_2 (°C)
$[Ln(TFA)_3]$	α	1:1	0.125	300	230
	β	3:1	0.0625	260	250
$[Ln(OA)_3]$	β	4:1	0.0625	260	250
$[Ln(Ac)_3]$	β	3:1	0.0625	260	250

This general procedure was further modified in terms of ion concentration and microwave conditions to obtain the hexagonal analogue. In brief, 1.25 mmol of $[Ln(TFA)_3]$ was prepared as before. For the synthesis of β-$NaGdF_4$:Yb^{3+}(20%),Er^{3+}(2%) NPs, 3.75 mmol of NaTFA (520.4 mg, resulting in a 3:1 Na^+-to-Ln^{3+} ion ratio) were added to the flask, along with 20 mL of a 2:1:1 ODE-OA-OAm mixture. Thus, the concentration of Ln^{3+} was 0.0625 $mol \cdot L^{-1}$. This precursor solution was degassed at 100 °C under stirring for 30 min. A volume of 10 mL of this solution was transferred into a 35-mL microwave vessel using a dry glass syringe, flushed with N_2, and tightly sealed before the insertion into the microwave reactor. The conditions were i) stirring at room temperature (1 min) followed by ii) rapid heating to 100 °C and subsequent static heating (1.5

min), ii) rapid heating to T_1 (5 min), iii) rapid cooling to T_2 (15 s) and static heating at T_2 (10 min), followed by iv) rapid cooling to 50 °C (6 min). For step i), medium speed was used for the stirring, while all subsequent steps used the slow speed setting. For the β-$NaLnF_4$-based NPs, the standard value for T_1 and T_2 were respectively 260 °C and 250 °C (Figure 9, microwave conditions are shown in Table 1 on page 26). Equations for chemical reactions are shown in Figure 10.

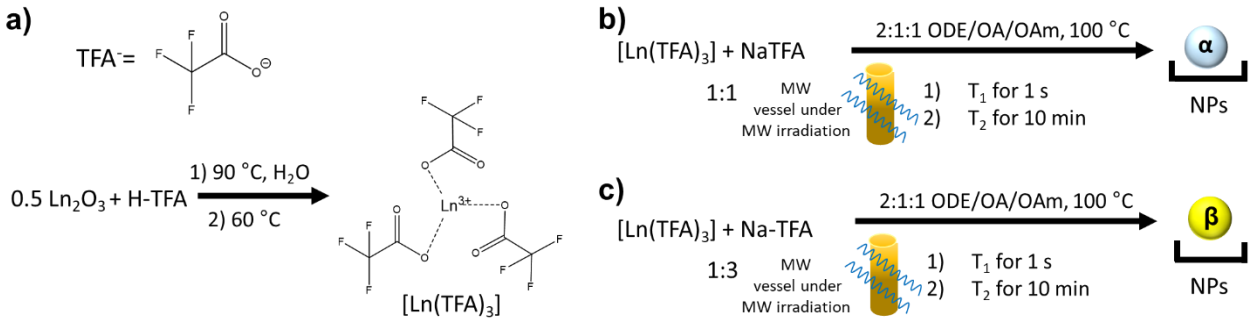

Figure 10. Reaction scheme for a) the preparation of $[Ln(TFA)_3]$ from Ln_2O_3 as well as the microwave-assisted synthesis of b) α-$NaLnF_4$ NPs and c) β-$NaLnF_4$ NPs from $[Ln(TFA)_3]$. MW stands for microwave.

Irrespective of the microwave conditions employed, the resulting NP dispersion was washed using the same protocol: the reaction mixture was transferred to a 50-mL centrifuge tube before the addition of 30 mL of ethanol. The mixture was centrifuged at 8000-10000 RPM for 20 min. After discarding the supernatant, a yellow oil was sometimes obtained along the pellet of NPs. In those cases, it was pipetted out and discarded. The NPs were further washed with a 1:3 toluene-acetone mixture and centrifuged using the same conditions. The NPs were stored in hexane or toluene prior to characterization. NaF – a potential by-product of the reaction with excess Na^+ – can be removed by an additional washing step with water. Therefore, the dry NPs were dispersed in 5 mL of ethanol. After the addition of 5 mL of H_2O, they were subsequently precipitated under the same centrifugation conditions as described above. A second dispersion and precipitation in 10 mL of ethanol was carried before storing the NPs in either hexane or toluene.

3.2.2 [Ln(OA)$_3$] route

The synthesis of lanthanide oleate precursors, [Ln(OA)$_3$], followed an adapted procedure reported in the literature.[80] In brief, 1.25 mmol of [Ln(OA)$_3$] was prepared using 1.25 mmol of [LnCl$_3$]. The chlorides were dissolved in a mixture of 6.6 mL of hexane, 3.8 mL of ethanol, and 2.8 mL of water along with 3.75 mmol (1141.7 mg, giving a 3:1 Na^+-to-Ln^{3+} ion ratio) of NaOA in a 50-mL three-neck round-bottom flask (Figure 11a). The solution was refluxed at 70 °C for 2 h under vigorous stirring. For example, the synthesis of $NaGdF_4$:Yb^{3+}(20%),Er^{3+}(2%) required 0.975 mmol (362.4 mg) of $GdCl_3 \cdot 6H_2O$, 0.25 mmol (96.9 mg) of $YbCl_3 \cdot xH_2O$, and 0.025 mmol (9.5 mg) of $ErCl_3 \cdot xH_2O$.

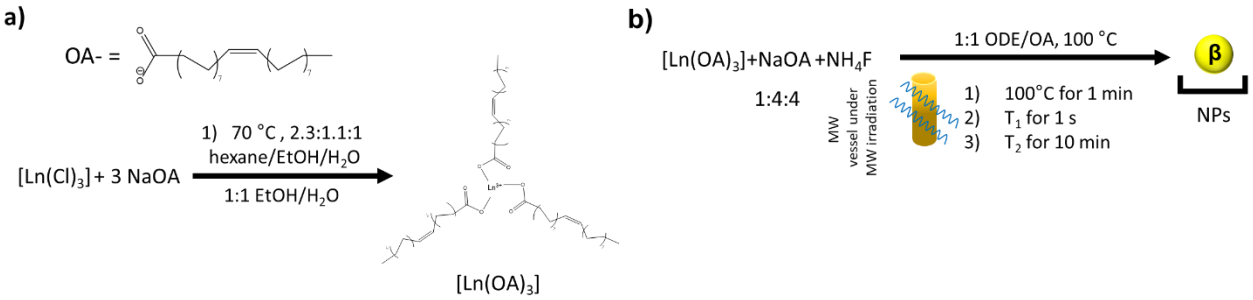

Figure 11. Reaction scheme for a) the preparation of [Ln(OA)$_3$] from [Ln(Cl)$_3$] as well as b) the microwave-assisted synthesis of β-$NaLnF_4$ NPs from [Ln(OA)$_3$]. MW stands for microwave.

Afterward, the organic layer containing the [Ln(OA)$_3$] was washed three times with 4 mL of a 1:1 H_2O-ethanol mixture in a separatory funnel. Afterward, the solution was poured into a 50-mL three-neck round-bottom flask along with 10 mL of ODE. The solution was dried at 70 °C under N_2 flux to remove residual hexane solvent. Subsequently, 10 mL of OA was added. For the synthesis of β-$NaLnF_4$ NPs, 5 mmol (1569.3 mg) of NaOA (resulting in a 4:1 Na^+-to-Ln^{3+} ion ratio) were added. The solution was degassed at 100 °C for 30 min. A 10 mL aliquot of this reaction mixture was transferred into a 35-mL microwave vessel containing 2.5 mmol (94.5 mg) of NH_4F, purged with N_2, tightly sealed, and subjected to the microwave radiation (Figure 11b). Like the

[Ln(TFA)$_3$] pathway, the solution was i) stirred at room temperature (1 min), followed by ii) rapid heating to 100 °C and subsequent static heating (1.5 min), iii) rapid heating to T_1 (10 to 15 min), iv) rapid cooling down to T_2 (15 s), v) static heating at T_2 (10 min), and vi) rapid cooling to 50 °C (6 min). For step i), medium speed was used for the stirring, while all subsequent steps used the slow speed setting. T_1 and T_2 values were the same as described with the [Ln(TFA)$_3$], 260 °C, and 250 °C (microwave conditions are shown in Table 1 on page 26). The washing and storing procedure was as described for the [Ln(TFA)$_3$]-derived NPs.

3.2.3 [Ln(Ac)$_3$] route

The NP synthesis using [Ln(Ac)$_3$] as precursors followed the same protocol as in the case of [Ln(OA)$_3$]. Therefore, 0.975 mmol (326.02 mg) of $Gd(CH_3CO_2)_3 \cdot xH_2O$, 0.25 mmol (105.56 mg) of $Yb(CH_3CO_2)_3 \cdot xH_2O$, and 0.025 mmol (8.61 mg) of $Er(CH_3CO_2)_3 \cdot xH_2O$ were dissolved together with 3.75 mmol (307.52 mg) of sodium acetate (NaAc, resulting in a 3:1 Na^+-to-Ln^{3+} ion ratio) in 20 mL of a 1:1 OA-ODE mixture and degassed under vacuum at 100 °C for 30 min (Figure 12). A 10 mL aliquot of the reaction mixture was transferred to a 35-ml microwave vessel. The microwave heating profile (Figure 9, microwave conditions are shown in Table 1 on page 26), NP precipitation, washing procedure, and storage were as described for the protocol with [Ln(TFA)$_3$] and [Ln(OA)$_3$] (*vide supra*).

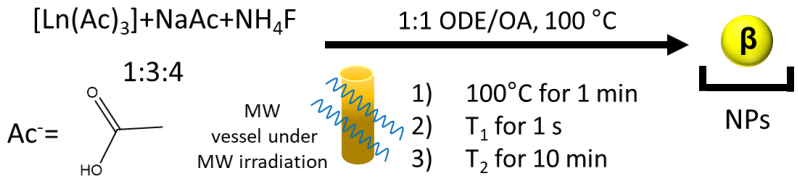

Figure 12. Scheme for the chemical equation for the microwave-synthesis of β-$NaLnF_4$ NPs from [Ln(Ac)$_3$]. MW stands for microwave.

3.2.4 Growth of a $NaGdF_4$ shell on $NaLnF_4$ nanoparticles using $[Ln(TFA)_3]$ as precursors

The core-only NPs were prepared as described above, from either $[Ln(TFA)_3]$, $[Ln(OA)_3]$ or $[Ln(Ac)_3]$ precursors. Following their synthesis, the core-only NPs were washed using a 1:3 hexane-to-ethanol (or toluene nonpolar solvent) mixture and centrifuged at 8000 RPM for 20 min. The pellet was dispersed in 5 mL of hexane, and the resulting suspension was divided into two equal volumes, with one half being set aside for further washing as described above and kept as a core-only NP reference to study the effects of the shell growth. The other half was precipitated and dried before being dispersed in 5 mL of ODE. The NP dispersion was transferred to a 50-mL three-neck flask containing the dry $[Gd(TFA)_3]$ precursor. Subsequently, 1.875 mmol (260.2 mg) of NaTFA (resulting in a 3:1 Na^+-to-Ln^{3+} ion ratio) along with 5 mL of OA were added, and the mixture was degassed at 100°C for 30 min. The whole 10 mL volume was transferred to a 35-mL microwave vessel, purged with N_2, and tightly sealed. The vessel was inserted into a CEM Discover SP Microwave reactor, and the shell was grown by subjecting the reaction mixture under constant stirring to the following temperature profile: (i) stirring at room temperature (1 min) (ii) heating to 230 °C (10 min), (iii) static heating at 230 °C (10 min), and (iv) gradual cooling to 50 °C (6 min), as seen in Table 2. For step i), medium speed was used for the stirring, while all subsequent steps used the slow speed setting. The washing procedure and storage for the obtained core/shell NPs were as described above for the core-only NPs.

Table 2. Microwave conditions used for the synthesis of core/shell Ln-NPs

Precursor of Core-only NPs	Phase of the core-only NPs	Na^+-to-Ln^{3+} Ion Ratio	Ln^{3+} Concentration ($mol \cdot L^{-1}$)	T(°C)	Phase of the Core/shell NPs
$[Ln(TFA)_3]$	β	3:1	0.0625	230	β
	α				α
$[Ln(OA)_3]$	β				β
$[Ln(Ac)_3]$	B				β

3.3 Combining lanthanide-based complexes and upconverting into a hybrid system

3.3.1 Amalgamation of UCNPs and Ln-based complexes into hybrid systems film

In a typical procedure, 40 mg of α-$NaGdF_4$:Yb^{3+}(20%),Tm^{3+}(0.5%) NPs prepared from [$Ln(TFA)_3$] precursors[ii] were precipitated from toluene or hexane upon addition of acetone and centrifugation. The UCNPs were then redispersed in a chloroform solution containing 40 mg of [$Ln_2(bpm)(tfaa)_6$][104] ([Ln_2], Ln=Tb^{3+} or Eu^{3+}) complexes, resulting in a UCNPs-to-complex mass ratio of 1:1. The so-prepared dispersion was sonicated for 10 min and diluted to the desired concentration (40 or 5 $mg \cdot mL^{-1}$). Afterward, 20 μL of the mixed sol was drop-casted on a glass microscope slide preventively washed with ethanol. The solvent was dried off overnight, obtaining the correspondent solid-state hybrid system as a combination of UCNPs and [$Ln_2(bpm)(tfaa)_6$] complexes, in the form of a film.

3.3.2 Preparation of the hybrid system in solution

A dispersion of α-$NaGdF_4$:Yb^{3+}(20%),Tm^{3+}(0.5%) NPs with a concentration of 1 $mg \cdot mL^{-1}$ and a concentrated (16 $mg \cdot mL^{-1}$) solution of [$Tb_2(bpm)(tfaa)_6$] were prepared in chloroform. The quenching of the NIR-trigger UCNP emission was investigated upon titration of the UCNPs dispersion with 100 μL-aliquots of the [$Tb_2(bpm)(tfaa)_6$] solution.

[ii] Note: The NPs were prepared with a T_1 value of 300 °C and a T_2 value of 260 °C. This will be discussed in more details in chapter 4.

3.4 Surface modification

3.4.1 Oleate (OA^-) ligand removal

Ligand-free NPs were prepared by dispersing 150 mg of oleate-capped NPs in a 1:1 hexane-HCl mixture (pH set to 1.5 for the aqueous phase).[93, 94] The two-phase mixture was stirred overnight at room temperature. Subsequently, it was poured into a separatory funnel, and the aqueous phase containing the NPs was isolated. The NP dispersion was transferred to a 50-mL centrifuge vessel with 45 mL of acetone and centrifuged for 20 min (10000 RPM). The NPs were stored in 5 mL of water or ethanol before characterization.

3.4.2 Silanization

The SiO_2 growth protocol was adapted from the literature.[59] In short, 20 mg of α-$NaGdF_4$:Yb^{3+}(20%),Tm^{3+}(0.5%) NPs[iii] were dispersed in 6 mL of cyclohexane with 100 µL of IGEPAL CO-520 and stirred vigorously for 10 min in a 25-mL round-bottom flask. Subsequently, 40 µL of IGEPAL CO-520 and 80 µL of NH_4OH were poured into the flask, and the mixture was sonicated for 30 min. Finally, 40 µL of TEOS was added, and the solution was stirred continuously for 48 h. The SiO_2-coated UCNPs were precipitated by the addition of 30 mL of acetone and centrifugation (10000 RPM, 40 min). Afterward, they were washed two times with a 1:1 water-ethanol mixture and were centrifuged for 20 min at 8000-10000 RPM. The UCNPs were then stored in 3 mL of water before characterization.

3.4.3 Polyacrylic acid (PAA) surface functionalization

The PAA coating was prepared using an adapted approach from the literature.[105] In short, 120 mg of PAA were dispersed in 10 mL of ethanol in a small vial. A 5-mL solution of chloroform

[iii] Prepared from [$Ln(TFA)_3$] precursors

containing 30 mg of 20 mg of α-$NaGdF_4$:Yb^{3+}(20%),Tm^{3+}(0.5%) NPs[iv] were added, and the two-phase mixture was stirred for 24 h at room temperature. PAA-capped UCNPs were precipitated by centrifuging at 8000 RPM for 20 min after the addition of 30 mL of acetone. The UCNPs were further washed using an 8:1 acetone-H_2O mixture. The UCNPs were stored in 3 mL water or ethanol before characterization.

3.4.4 α-NH_2-ω-COOH-Polyethylene glycol (PEG) surface functionalization

A protocol similar to the one described for PAA was employed for grafting PEG on the surface of α-$NaGdF_4$:Yb^{3+}(20%),Tm^{3+}(0.5%) NPs.[105,106] 20 mg of the UCNPs were dispersed in 1.34 mL of chloroform, while 50 mg of α-$NaGdF_4$:Yb^{3+}(20%),Tm^{3+}(0.5%) NPs[vi] was dissolved in 6 mL of ethanol. The two solutions were mixed and stirred at room temperature overnight. They were washed as described for the PAA-capped UCNPs. The PEG-capped UCNPs were stored in 3 mL of water or ethanol at 4 °C before characterization.

3.5 Characterization techniques

3.5.1 Crystalline phase and morphology

To determine the crystalline phase of the NPs, powder X-ray diffraction (XRD) analysis was performed using a Rigaku Ultima IV Diffractometer (Cu Kα, λ = 1.5401 Å), operating at 44 kV and 40 mA (step size: 0.02 °, scan speed between 0.15 and 2.5 ° min^{-1}). NP dispersions were drop-casted and dried on an amorphous glass substrate before XRD measurement. XRD were acquired in 20 ° to 60 ° range. The size and morphology of the NPs were obtained by transmission electron microscopy (TEM) using a FEI Tecnai Spirit microscope operated at 120 kV. NP dispersions were

[iv] Prepared from [$Ln(TFA)_3$] precursors

diluted by a factor of 10 ([$Ln(TFA)_3$]-derived and core/shell NPs) or 100 ([$Ln(Ac)_3$] and [$Ln(OA)_3$]-derived NPs). Samples were then dispersed on a Formvar/carbon film supported on a 300-mesh copper TEM grid. The average particle diameters were extracted with ImageJ using the straight-line option. The morphology of the hybrid system film was investigated using the TEM as well as a scanning electron microscope (SEM, JEOL JSM-7500F FESEM) operated at 120 kV. SEM observations were conducted on the hybrid system prepared on a glass slide (as above described) after gold-sputtering (layer thickness ca. 3 nm) in a vacuum coater (Leica EM ACE200). Energy dispersive X-ray (EDX) measurements were performed on a Zeiss Gemini SEM 500 equipped with a Bruker EDX detector. Profilometry measurements were performed with a Dektak profilometer using a stylus with 2 μm tip and an applied force of 19.62 $mN \cdot m^{-1}$.

3.5.2 Optical properties

Solid-state emission spectra under UV and NIR excitation and hyperspectral images were acquired on dried films of NPs on microscopy slides (1 mm thick, Fischer Scientific) using a custom-built hyperspectral microscope IMA^{TM} (PhotonEtc, Montreal). This optical system contains a Princeton Instruments SP-2360 monochromator/spectrograph, an inverted Nikon Eclipse Ti optical microscope, a set of galvanometer mirrors, visible and NIR emission filters, a Princeton Instruments ProEM EMCCD camera for the visible emission, and a BaySpec Nunavut deep-cooled InGaAs detector for the detection of the NIR emission. Two excitation sources were used: a 980-nm (NIR) laser diode and a Nikon IntensiLight halogen lamp (100 W). For this microscope stage mode, the maximum power density was estimated to be ca. $4 \cdot 10^7$ $mW \cdot cm^{-2}$ with a beam diameter of approximately 1.5 μm.

NP dispersions in toluene (5 $mg \cdot mL^{-1}$) or water (any concentration) were analyzed with the same system, using however a 1-cm optical glass cuvette and a 90° configuration to record visible and

NIR emission. Excitation in the cuvette mode was performed with a 980-nm laser diode focused on a laser spot with an estimated diameter of no larger than 1 mm. The laser power density was estimated to be ca. around 100 $mW \cdot cm^{-2}$ for this recording mode.

Power-dependent studies under NIR excitation were performed either in the cuvette or microscope stage mode, using a set of neutral density (ND) filters to stepwise reduce the incident laser power. Power was either measured on the microscope stage in case of solid-state measurement or in front of the focusing lens in front of the cuvette holder in case of the dispersion measurement.

Optical absorption spectra of the [Ln_2] complexes were recorded on a Cary Varian 5000 in the 300-1200 nm range with a scan step of 0.5 nm and a scan speed of 600 $nm \cdot min^{-1}$. For recording diffuse reflectance spectra (DRS), an accessory for solid-state measurements was used. Excitation spectra of the complexes were acquired on a Varian Cary Eclipse spectrofluorometer.

For luminescence lifetime measurements on the hybrid system film (solid-state, presented in Chapter 5), a 980-nm diode laser in current modulated pulsed mode was used as the radiation source (CNI Optoelectronics Tech). The beam was focused on the sample and the emission was gathered with a 40× objective and a beam splitter (Thorlabs, BSS10) in backscattering mode. Steady-state upconversion spectra were recorded using a halfmeter monochromator (Andor, Shamrock 500i) equipped with a 1200 lines mm^{-1} grating and CCD detector (Andor, iDus420-BVF). The decay curves were also recorded with a half-meter monochromator (Andor, Shamrock 500i) equipped with a 1200 lines mm^{-1} grating and a Hamamatsu R928 photomultiplier tube connected to a 500 MHz digital oscilloscope (LeCroy, WaveRunner LT342). Luminescent lifetime measurements on the UCNPs dispersion (5 $mg \cdot mL^{-1}$ in toluene, presented in Chapter 3) were performed on a FLS980 (Edinburg Instruments, UK) spectrometer equipped with a double emission monochromator, cooled (-20 °C) single-photon counting photomultiplier (Hamamatsu

R2658P, Japan), and a 1000-mW 980-nm pulsed laser diode MDL-III-980 (CNI, China) with 70 μs pulse width and 200-Hz repetition rate. Lifetimes of the $^4S_{3/2}$ and $^4F_{9/2}$ emitting levels were obtained by integration of the area under the normalized emission decay curves.

3.5.3 Other characterization techniques

Thermogravimetric analysis (TGA) of the $[Ln(Ac)_3]$, $[Ln(TFA)_3]$, and $[Ln(OA)_3]$ precursors were carried out using a TGA Q500/Discovery under an N_2 atmosphere and at a heating rate of 10 °C/min. Surface functionalization was confirmed by Fourier transform infrared (FTIR) spectroscopy with a Shimadzu FT-IR8400S. Therefore, samples were dispersed in a KBr pellet before the measurement. Pure KBr was used as a reference.

4 Microwave-assisted synthesis of $NaLnF_4$-based nanoparticles

Note: All figures and tables presented in this chapter are reprinted (adapted) with permission from reference [107] *with permission from The Royal Society of Chemistry.*

4.1 The importance of precursor chemistry

4.1.1 $[Ln(TFA)_3]$ route

While there are microwave-assisted reaction protocols using $[Ln(TFA)_3]$ reported in the literature, to date, these were only suitable for the growth of cubic-phase NPs.[3,4] An exception was published by the Hemmer group (Liu *et al.*), where the phase-selective microwave-assisted synthesis of undoped $NaGdF_4$ NPs was achieved through control of the Na^+-to-Ln^{3+} ion ratio.[52] It was demonstrated that cubic-phase NPs are obtained when using a 1:1 ion ratio, while the synthesis of hexagonal-phase NPs requires a 2:1 ion ratio.

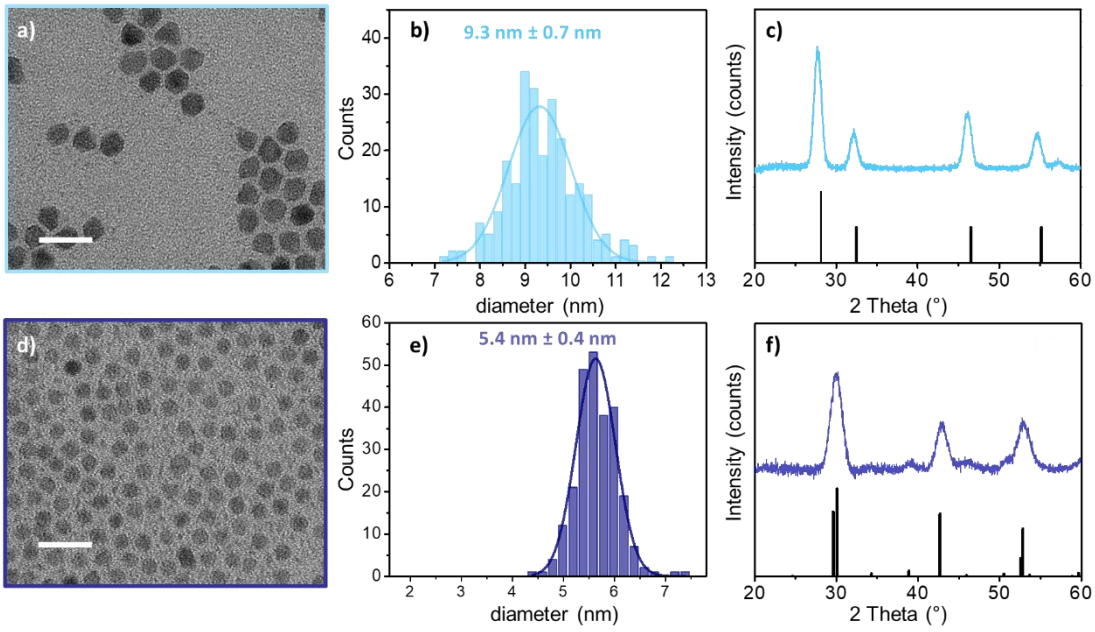

Figure 13. a) TEM image and b) corresponding size distribution of α-$NaGdF_4$:Yb^{3+},Er^{3+} NPs made from $[Ln(TFA)_3]$ precursors. c) Associated XRD pattern of the α-$NaGdF_4$:Yb^{3+},Er^{3+} NPs. d) TEM image and e) corresponding size distribution of β-$NaGdF_4$:Yb^{3+},Er^{3+} NPs made from $[Ln(TFA)_3]$ precursors. f) Associated XRD pattern of the β-$NaGdF_4$:Yb^{3+},Er^{3+} NPs. Scale bars are 20 nm. References: β-$NaGdF_4$ (PDF#: 01-080-8787), α-NaGdF4 (PDF#: 00-027-0697).

In analogy, when using a Ln^{3+} concentration of 0.125 mol·L^{-1} and a 1:1 Na^{+}-to-Ln^{3+} ion ratio, α-$NaGdF_4$:Yb^{3+}(20%),Er^{3+}(2%) NPs of spherical morphology and with a size of 9.3 ± 0.7 nm were obtained (Figure 13a-b). The crystalline phase was confirmed by XRD analysis (Figure 13c). Such NPs size is comparable to NP sizes previously reported for cubic-phase NPs by microwave-assisted methods.[3,4] However, the protocol yielding for undoped β-$NaGdF_4$ NPs was not suitable to synthesize β-$NaGdF_4$ NPs doped with Yb^{3+}(20%), and either Er^{3+}, Tm^{3+} or Ho^{3+}. Instead, it was found that decreasing the Ln^{3+} concentration to 0.0625 mol·L^{-1} – while simultaneously increasing Na^{+}-to-Ln^{3+} ion ratio to 3:1 – was necessary to obtain hexagonal-phase Ln^{3+}-doped NPs (*vide infra*). [$Ln(TFA)_3$]-derived NPs had a spherical morphology with a narrow size distribution and an average diameter of 5.4 ± 0.4 nm (Figure 13d and 13f). XRD analysis confirmed crystallization in the hexagonal phase of $NaGdF_4$, while the observed peak broadening is expected for NPs of such small size (Figure 13e). As mentioned above, the Na^{+}-to-Ln^{3+} ion ratio was a key parameter for phase-control of undoped small $NaGdF_4$ NPs (2:1 for the hexagonal phase, 1:1 for the cubic phase).[52] Here, it is demonstrated that further tuning of the ion ratio and precursor concentration are required to promote the formation of phase-pure and β-$NaGdF_4$ when doped with Er^{3+} and Yb^{3+} at a concentration high enough to endow the NPs with good upconversion capabilities, *i.e.*, 2 and 20 mol%, respectively. As a result, rapid synthesis of sub-10 nm $NaGdF_4$:Yb^{3+}(20%), Er^{3+}(2%) NPs in either the cubic (1:1 ion ratio) or hexagonal (3:1 ion ratio) phase became accessible.

Noteworthy, precursor concentration in the reaction mixture was identified as a phase-influencing parameter. Aiming for the cubic phase, higher Ln^{3+} concentrations – together with a 1:1 Na^{+}-to-Ln^{3+} ion ratio – had to be used, namely 0.125 mol·L^{-1} (*versus* 0.0625 mol·L^{-1} when synthesizing hexagonal-phase NPs). Using such Ln^{3+} concentrations when aiming for hexagonal-phase NPs

resulted in a phase-mixture that exhibited XRD diffraction peaks of both crystalline phase of $NaGdF_4$ (Figure 14a), even at a Na^+-to-Ln^{3+} ion ratio of 3:1. Since the crystalline phase is an enormous factor of the optical behavior of the NPs (demonstrated in section 4.1.5), such NPs mixture is of little interest for the pursue of optical-based applications.

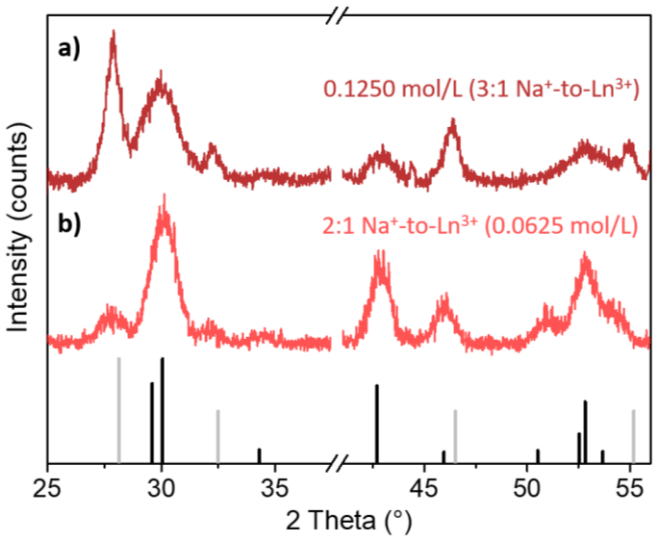

Figure 14. Effect of precursor concentration and Na^+-to-Ln^{3+} ion ratio on phase formation: a) Using a too high Ln^{3+} ion concentration (0.1250 mol/L *versus* 0.0625 mol/L) in combination with a 3:1 Na^+-to-Ln^{3+} ion ratio resulted in the formation of a phase mixture. b) Using a Na^+-to-Ln^{3+} ion ratio of only 2:1 (*versus* 3:1) led to the formation of α-$NaGdF_4$ in addition to β-$NaGdF_4$ (Ln^{3+} ion concentration: 0.0625 mol/L). References: α-$NaGdF_4$ (PDF#: 00-027-0697, light grey lines), β-$NaGdF_4$ (PDF#: 01-080-8787, black lines). Reflections at 39° due to NaF were removed for clarity.

The preferential formation of the hexagonal phase in the presence of excess Na^+ ions – using an appropriate precursor concentration – is in agreement with previous work on the growth mechanism of $NaLnF_4$ NPs.[55] It is well-know that the presence of Gd^{3+} ions in $NaLnF_4$ NPs generally favors the crystallization in their hexagonal phase.[55,56] In line with this, it is possible to obtain undoped $NaGdF_4$ NPs under relatively mild microwave reaction conditions with a 2:1 Na^+-to-Ln^{3+} ion ratio.[52] In contrast, when such ion ratio was used to synthesized β-$NaGdF_4$:Yb^{3+},Er^{3+} NPs, it yielded a phase mixture despite the Ln^{3+} concentration of 0.625 mol·L^{-1} (Figure 14). Yb^{3+} and Er^{3+} ions belong to the group of Ln^{3+} ions (including Lu^{3+}, $Tm^{3+,}$ and Ho^{3+}) that prefer to

crystallize in the cubic phase.[56] Therefore, it appears harsher reaction conditions are required to foster the hexagonal-phase UCNPs. With this in mind, the necessity for an ion ratio of at least 3:1 (Figure 14) to foster the formation of β-$NaGdF_4$:Yb^{3+},Er^{3+} under microwave conditions can be ascribed to two important aspects: (i) the effect of the ion ratio itself on phase formation with Na^+ in excess favouring the hexagonal phase, and (ii) the enhanced capability of the ion-enriched reaction mixture to absorb microwave energy (OA/ODE/OAm alone being rather poor microwave absorbers) providing the system the energy required for crystallization in the hexagonal phase. [31,87]

4.1.2 The [Ln(OA)$_3$] route

To investigate the influence of the Ln^{3+} and Na^+ precursor chemistry on the NPs growth, it was decided to further use [$Ln(OA)_3$] in the developed microwave-assisted protocol. Under reaction conditions almost identical to those described above for the synthesis of hexagonal-phase NPs from [$Ln(TFA)_3$] (T_1 = 260 °C, T_2 = 250 °C, Ln^{3+} concentration = 0.0625 mol·L^{-1}, Na^+-to-Ln^{3+} is 4:1), quasi-spherical [$Ln(OA)_3$]-derived NPs with a diameter of 3.2 ± 0.3 nm were obtained (Figures 15a-b). XRD patterns of on the samples confirmed the formation of the hexagonal phase (Figure 15c).

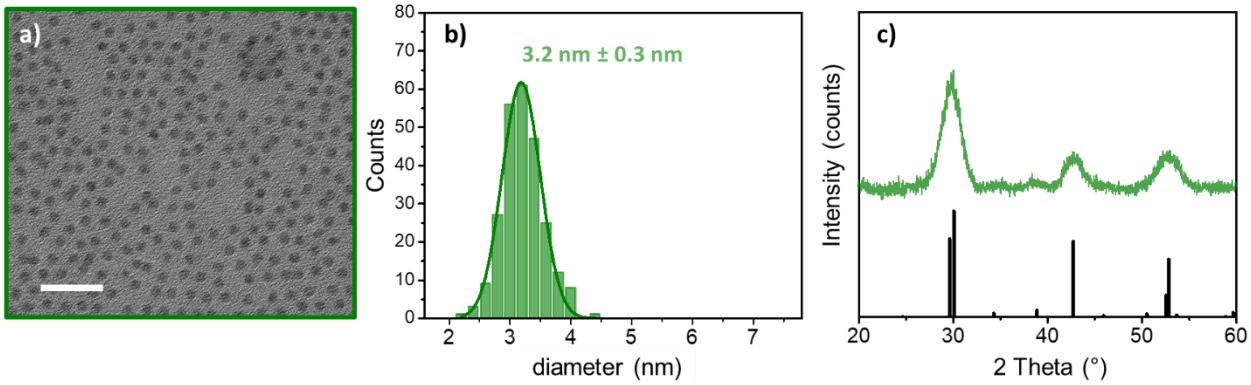

Figure 15. a) TEM image and b) corresponding size distribution of β-$NaGdF_4$:Yb^{3+},Er^{3+} NPs made from [$Ln(OA)_3$] precursors. c) Associated XRD pattern of the β-$NaGdF_4$:Yb^{3+},Er^{3+} NPs. Reference: β-$NaGdF_4$ (PDF#: 01-080-8787). Scale bar is 20 nm.

These findings on ultrasmall $NaGdF_4:Yb^{3+},Er^{3+}$ NPs are in good agreement with those that were recently reported by Amouroux *et al*.[31] The authors demonstrated the suitability of $[Ln(OA)_3]$ as precursors – together with NaOH as sodium source – for the microwave-assisted synthesis of hexagonal UCNPs. They achieved size control at the sub-5 nm realm by increasing the reaction time to up to 30 min. Alternatively, the classical co-precipitation approach using lanthanide chloride as precursors is known to result in β-$NaGdF_4:Yb^{3+},Er^{3+}$ NPs of comparable sizes in the 2.5-to-8 nm range as a function of reaction time.[81,108] Yet, compared to those previously reported synthetic routes, the here presented microwave-assisted strategy comes with the advantage of reduced reaction times (10 min *versus* up to 100 min).

4.1.3 $[Ln(Ac)_3]$ route

To further investigate the influence of the precursor chemistry on NPs growth, we decided to use $[Ln(Ac)_3]$ in the developed microwave-assisted protocol. Under reaction conditions identical to those described above for the synthesis of hexagonal-phase NPs from $[Ln(TFA)_3]$ (T_1 = 260 °C, T_2 = 250 °C, Ln^{3+} concentration = 0.0625 mol·L^{-1}, Na^+-to-Ln^{3+} is 3:1), quasi-spherical $[Ln(Ac)_3]$-derived NPs with a diameter of 3.2 ± 0.3 nm, were obtained (Figures 16a-b). XRD pattern confirmed the formation of the hexagonal phase (Figure 16c). While $[Ln(Ac)_3]$ has previously been reported as precursor applied in a microwave-assisted decomposition using a benzyl alcohol/ water mixture yielding β-$NaYF_4:Ln^{3+}$ nanorods or α-$NaYF_4:Ln^{3+}$ of undefined morphology,[95,109] the herein developed approach grants access to the sub-5 nm size regime for β-$NaGdF_4:Yb^{3+},Er^{3+}$ NPs. Besides, when aiming for ultrasmall NPs, the use of $[Ln(Ac)_3]$ is particularly appealing as time- and resources-consuming precursor synthesis can be omitted by directly employing commercially available $[Ln(Ac)_3]$ in the microwave process.

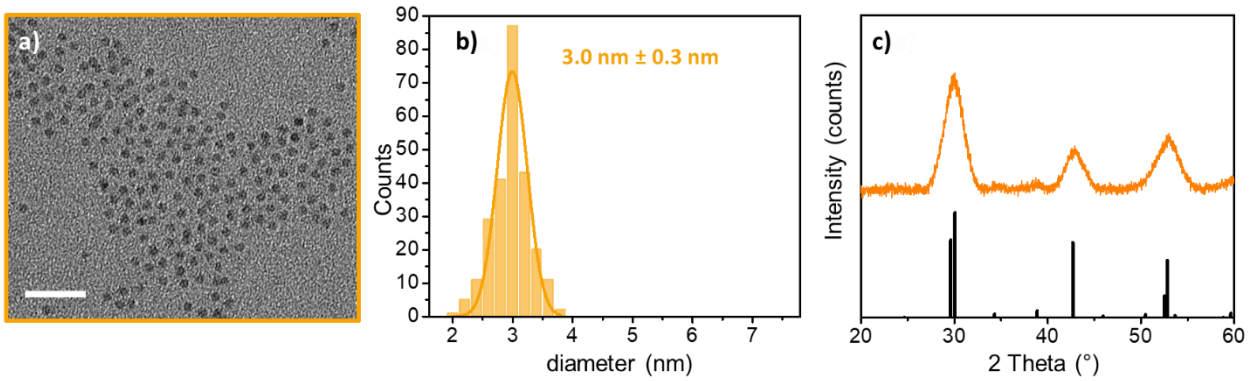

Figure 16. a) TEM image and b) corresponding size distribution of β-$NaGdF_4$:Yb^{3+},Er^{3+} NPs made from [$Ln(Ac)_3$] precursors. c) Associated XRD pattern of the β-$NaGdF_4$:Yb^{3+},Er^{3+} NPs. Reference: β-$NaGdF_4$ (PDF#: 01-080-8787). Scale bar is 20 nm.

4.1.4 Tailoring nanoparticle size and crystal phase through precursor chemistry

The results described above demonstrate that varying of precursor chemistry is an attractive alternative to variation of reaction time and temperature when seeking size control of (ultra)small Ln-based NPs. As such, reaction time as short as possible can be retained, fully profiting from the major advantages of microwave-assisted strategies when compared to classical thermal decomposition and co-precipitation processes. With respect to precursor-induced size control, it is suggested that differences in the thermal stability of the precursors under investigation – [$Ln(TFA)_3$] on one side *versus* [$Ln(OA)_3$] and [$Ln(Ac)_3$] on the other – has a strong impact on the reaction kinetics of NP formation. Indeed, changes in thermal stability can alter nucleation and NP growth processes, ultimately determining NPs size.[47] In support of this, thermogravimetric analysis (TGA) of [$Ln(TFA)_3$], [$Ln(Ac)_3$], and [$Ln(OA)_3$] was performed (Figure 17).

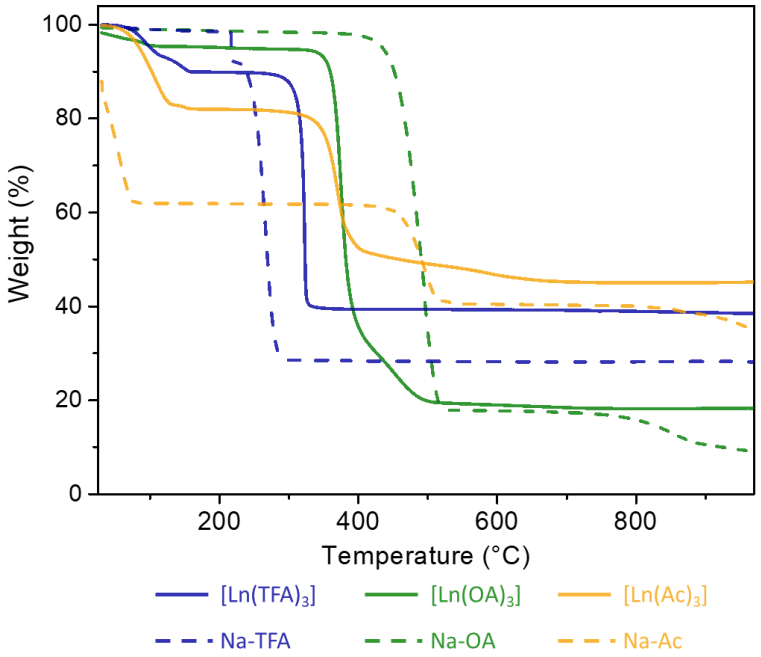

Figure 17. TGA profiles of each of the Ln^{3+} precursors, as well as sodium sources used in the microwave-assisted thermal decomposition.

The thermal decomposition profiles of the three Ln-precursors showed a first weight loss of up to 10% at temperatures below 200 °C. This was attributed to the removal of residual water and trifluoracetic acid, while the actual thermal decomposition took place at higher temperatures. TGA analysis revealed a lower decomposition temperature and sharper decomposition profile for $[Ln(TFA)_3]$ (Figure 17, blue curve), accounting for the larger size of the obtained NPs. The steep decrease in weight obtained for $[Ln(TFA)_3]$ indicated a decomposition temperature of 320 °C, which matches well with data reported in the literature.[110,111] Meanwhile, an almost identical decomposition behavior was observed for $[Ln(Ac)_3]$ and $[Ln(OA)_3]$, and the obtained TGA curves indicate higher thermal stability when compared to $[Ln(TFA)_3]$. Their decomposition temperature was found to be shifted towards higher temperatures, namely 380 °C (Figure 17, green and orange curve).[47,112] Moreover, both latter precursors exhibited a second, less pronounced mass loss at higher temperatures. Based on reported literature, these two weight losses correspond to the decomposition of the anhydrous precursor to the oxycarbonate, $Ln_2O_3 \cdot CO_2$, as well as the

formation of the sesquioxide, Ln_2O_3.[112] The decomposition profiles are in line with (i) the comparable size ranges of NPs derived from [$Ln(Ac)_3$] and [$Ln(OA)_3$], and (ii) their smaller size in comparison to [$Ln(TFA)_3$]-derived NPs. An additional explanation for the NP size dependence on the precursors, one should also take into account the presence of the -CF_3 groups in [$Ln(TFA)_3$], which is absent in the other two precursors. Herein, the stronger electron-withdrawing nature of the -CF_3 moiety can facilitate the release of Ln^{3+} ions and, hence, NP nucleation and growth.[111]

Furthermore, a look at the pressure evolution in the microwave vessel during the NP synthesis (Figure 18) provides further insight into materials formation and growth. As the microwave-assisted synthesis of NPs takes place in a closed system, an increase in temperature, decomposition of precursors, and formation of gaseous by-products result in a pressure increase in the microwave reaction vessel.

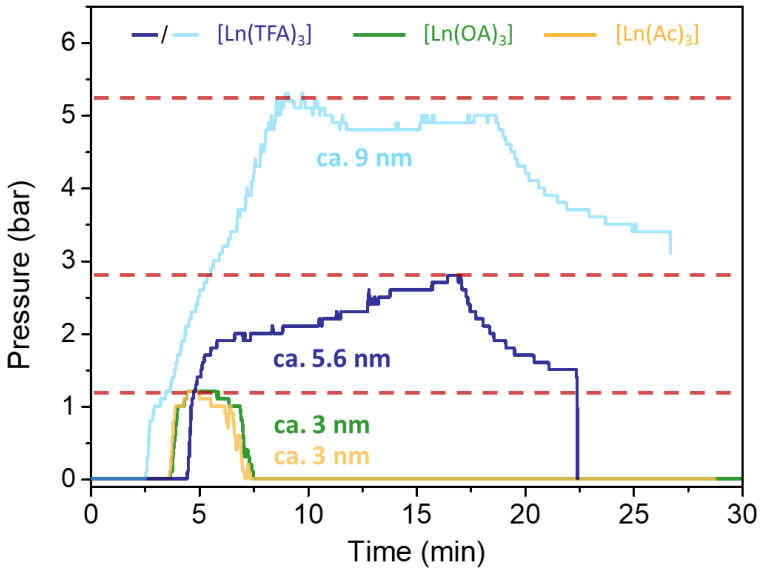

Figure 18. Pressure profiles showing the time-dependent pressure evolution during the microwave-assisted synthesis of cubic (light blue line) and hexagonal (dark blue, green, yellow lines) $NaGdF_4$:Yb^{3+},Er^{3+} NPs using [$Ln(TFA)_3$], [$Ln(OA)_3$], and [$Ln(Ac)_3$] as precursors. Herein, given pressure values constitute the pressure that was sensed on the Teflon cap placed on the microwave reaction vessel. The sizes of the NPs are included for clarity.

For all precursors, pressure steeply increased at the beginning of the reaction with increasing temperature during the first 5 min. This rise in pressure was associated with the beginning of the precursor decomposition, triggering the formation of the first nuclei. Notably, the pressure profiles in the case of [$Ln(OA)_3$] and [$Ln(Ac)_3$] were very similar to each other, and the pressure increase reached its maximum of 1.3 bar within less than 5 min (green and orange line). The pressure remained unchanged till 7 min – the time point at which the set reaction temperature (T_2) was approached –, followed by a drop to atmospheric pressure (pressure applied to the Teflon cap: 0 bar) for the remaining reaction time. It can be noted that such a pressure profile exhibits a LaMer-like character, as it does not continuously increase.[77,113,114] Therefore, it is suggested that the temperature-induced increase in pressure also reflects a growing precursor decomposition rate, along with increasing nucleation that, in turn, reached its maximum at maximum pressure. Meanwhile, for [$Ln(TFA)_3$], the pressure rose continuously during the complete reaction time and increased to maximum values of 2.8 and 5.3 bar, respectively, before decreasing to atmospheric pressure upon initialization of the cooling process. Along with these higher-pressure conditions during the reaction came larger NP sizes of ca. 5.6 and 9.3 nm, respectively (compared to around 3 nm for [$Ln(OA)_3$] and [$Ln(Ac)_3$]). Thus, the pressure profile can be correlated with the resulting NP size: the higher the pressure reached during the synthesis, the larger was the resulting NP size.

4.1.5 Optical properties of $NaGdF_4$:Yb^{3+}(20%),Er^{3+}(2%) nanoparticles obtained from [$Ln(TFA)_3$], [$Ln(OA)_3$], and [$Ln(Ac)_3$]

Despite their small size and irrespective of the crystalline phase, all prepared NPs showed upconversion and NIR emission under 980 nm excitation (Figure 19). Characteristic UC emission peaks in the blue, green and red (visible) spectral regions are ascribed to the $^2H_{9/2} \rightarrow {}^4I_{15/2}$ (408 nm), $^2H_{11/2} \rightarrow {}^4I_{15/2}$ (520 nm) $^4S_{3/2} \rightarrow {}^4I_{15/2}$ (550 nm) and $^4F_{9/2} \rightarrow {}^4I_{15/2}$ (650 nm) Er^{3+} transitions in

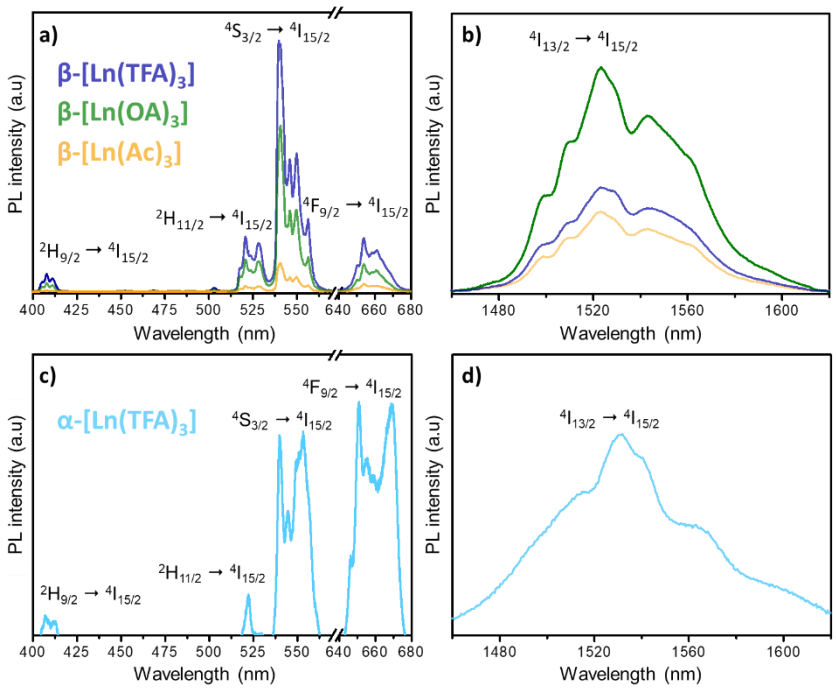

Figure 19. a) UC-based visible and b) DS-based NIR emission spectra of β-$NaGdF_4$:Yb^{3+}(20%),Er^{3+}(2%) NPs synthesized from $[Ln(TFA)_3]$, $[Ln(OA)_3]$, and $[Ln(Ac)_3]$ precursors. c) UC-based visible and d) DS-based NIR emission spectra of the α-$NaGdF_4$:Yb^{3+}(20%),Er^{3+}(2%) NPs synthesized from $[Ln(TFA)_3]$ precursors. All spectra were obtained under 980-nm laser excitation (P = 150 mW). Note that the spectra obtained for the cubic-phase and the hexagonal-phase NPs are not comparable in terms of absolute upconversion as well as NIR PL due to the different exposure times used. Comparisons between PL are shown in Table S1 on page 92.

Figure19a and 19c. The NIR emission centered at 1520 nm stems from the $^4I_{13/2} \rightarrow {}^4I_{15/2}$ transition (Figure 19b and 19d).

The green-to-red (G/R) ratio is significantly larger than 1 for all hexagonal phase samples, which provides further evidence for the hexagonal phase of the host lattice.[115] Based on the determined particle sizes, it is not surprising that $[Ln(TFA)_3]$-derived NPs (sub-10 nm) showed brighter upconversion emission when compared to $[Ln(OA)_3]$- and $[Ln(Ac)_3]$-derived ones (sub-5 nm). The loss in the overall visible emission intensity with decreasing particle size can be ascribed to surface quenching for the smaller UCNPs. For the NIR emission, $[Ln(OA)_3]$-derived NPs showed the brightest emission, followed by those obtained from $[Ln(TFA)_3]$ and $[Ln(Ac)_3]$. α-$NaGdF_4$:Yb^{3+}(20%),Er^{3+}(2%) NPs derived from $[Ln(TFA)_3]$ exhibited a more prominent red

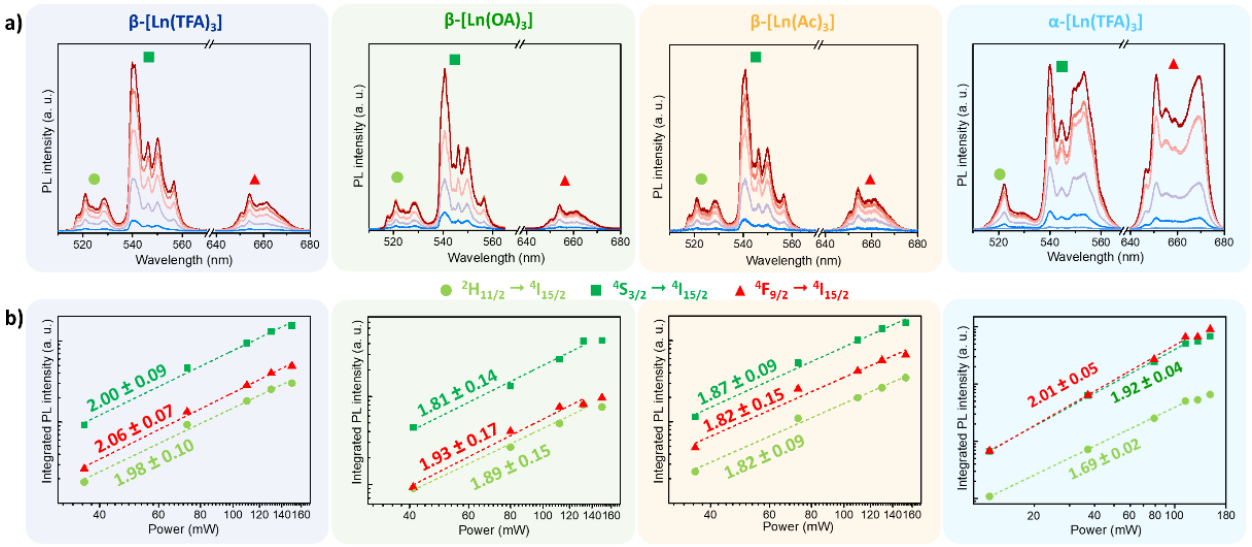

Figure 20. a) Excitation power-dependent upconversion spectra and b) integrated $^2H_{11/2} \rightarrow {}^4I_{15/2}$, $^4S_{3/2} \rightarrow {}^4I_{15/2}$, and $^4F_{9/2} \rightarrow {}^4I_{15/2}$ Er^{3+} intensity *versus* 980-nm excitation power for β-$NaGdF_4$:Yb^{3+},Er^{3+} NPs synthesized using [$Ln(TFA)_3$], [$Ln(OA)_3$], and [$Ln(Ac)_3$] and α-$NaGdF_4$:Yb^{3+}(20%),Er^{3+}(2%) NPs synthesized using [$Ln(TFA)_3$].

emission (Figure 19a). The resulting G/R ratio smaller than 1 is expected for the higher-symmetry cubic phase of $NaLnF_4$.[115]

The photophysical properties of the UCNPs, irrespective of the crystalline phase or the precursors employed, were further analyzed through power-dependent photoluminescence spectroscopy (Figures 20). As mentioned in the introduction, UC is a nonlinear process in which multiple photons are absorbed sequentially in order to excite the Ln^{3+} ions. The transition's photon order (*i.e.*, the number of photons required to populate the emitting Ln^{3+} energy level) can be extracted from the slope of a logarithmic plot displaying emission intensity *versus* excitation power. Regardless of the precursor or the resulting crystalline phase selected, both the green and the red Er^{3+} upconversion emissions were found to be 2-photon processes, as expected for the Yb^{3+}/Er^{3+} upconversion ion pair.

Lifetime values are indicative of the radiative relaxation dynamics present in the photoluminescent (be it a NP or a molecule).[116] Due to the complex nature of the UC relaxation process in Ln-NPs,

the lifetime decay curves shown below (Figure 21) do not have a clear single-exponential character.[117,118] The Yb^{3+}-to-Er^{3+} energy transfer rate, the lifetime of Er^{3+} intermediate levels, and the lifetime of the Yb^{3+} excited state (which also plays a role in the upconversion excitation pathway) may influence the emitting level decay profile.[117]

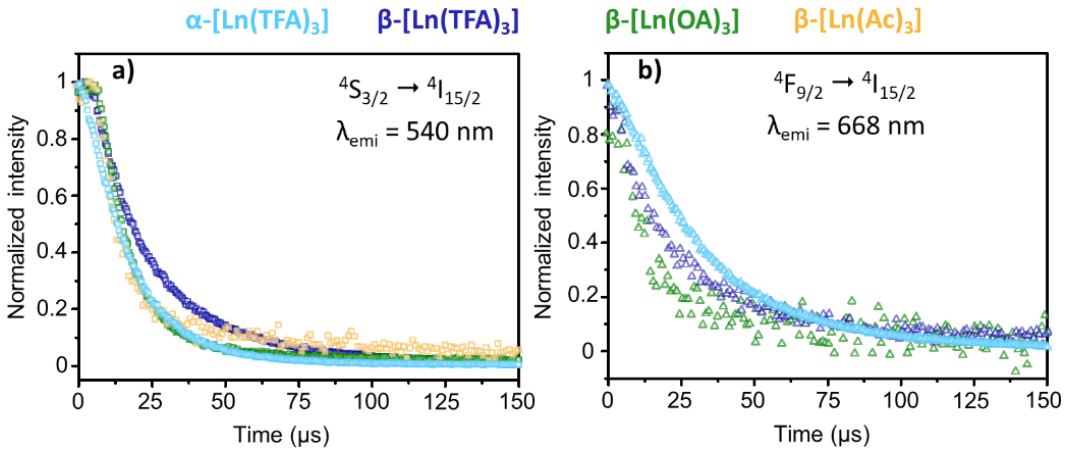

Figure 21. Decay curves of the a) $^4S_{3/2} \rightarrow {}^4I_{15/2}$ (540 nm) and b) $^4F_{9/2} \rightarrow {}^4I_{15/2}$ (668 nm) Er^{3+} transitions for α- and β-$NaGdF_4$:Yb^{3+}(20%),Er^{3+}(2%) NPs synthesized using $[Ln(TFA)_3]$, $[Ln(OA)_3]$, and $[Ln(Ac)_3]$ as precursors. All decay curves were obtained under 980-nm pulsed laser excitation.

Table 3. Lifetime values and corresponding NP sizes of α- and β-$NaGdF_4$:Yb^{3+},Er^{3+} core-only synthesized by the microwave-assisted method

Core Precursor	Crystalline Phase	Lifetime (μs)		Approx. NP Size (nm)
		$^4S_{3/2} \rightarrow {}^4I_{15/2}$ [540 nm]	$^4F_{9/2} \rightarrow {}^4I_{15/2}$ [655 nm]	
$[Ln(TFA)_3]$	B	22	25	5.5
$[Ln(OA)_3]$		16	18	3.2
$[Ln(Ac)_3]$		17	–[a]	3.0
$[Ln(TFA)_3]$	α	15	29	9.3

[a] weak band.

Moreover, these small UCNPs likely have emission centres occupying sites with different chemical surroundings and coordination environments (namely at the NP surface and in the NP

core), resulting in a heterogeneous population of the emitting Ln^{3+} ions.[32] Accounting for this heterogeneity (reflected in the multi-exponential character of the decay curves), the lifetimes of the $^4S_{3/2}$ and $^4F_{9/2}$ emitting levels of Er^{3+} were calculated by integration of the area under the normalized emission decay curves. The lifetime results (Table 3) confirmed a more pronounced surface quenching effect for the smaller NPs. The sub-5 nm hexagonal-phase NPs exhibited shorter lifetimes (16 µs for $[Ln(OA)_3]$ and 17 µs for $[Ln(Ac)_3]$) for the $^4S_{3/2}$ emitting level (540 nm emission) compared to the larger $[Ln(TFA)_3]$-derived NPs (22 µs). For the $^4F_{9/2}$ emitting level (650 nm emission), the same tendency was observed (for values, refer to Table 3). Overall, the lifetime values herein found for both the green and red emissions of Er^{3+} were below 50 µs, in line with lifetimes previously reported by Gargas *et al.* and Würth *et al.* for similar-sized small (sub-10 nm) Yb^{3+}/Er^{3+}-doped UCNPs.[118,119] The cubic-phase NPs had a longer lifetime for the $^4F_{9/2}$ (29 µs) emitting level than for the $^4S_{3/2}$ (15 µs) one (Figure 21). The same trend is observed with the lifetimes of hexagonal-phase NPs for the $^4F_{9/2}$ and $^4S_{3/2}$ energy levels, albeit with smaller differences between the two values (Table 3) that can be attributed to the different crystalline phase and size. Noteworthy, the relatively low emission intensities both in the visible and NIR regions for $[Ln(Ac)_3]$-derived NPs when compared to $[Ln(OA)_3]$-derived ones speak for the higher quality of the nanocrystals in the latter case.

4.2 Phase formation and nanoparticle growth in microwave-assisted synthesis

4.2.1 Effect of the reaction time

The initial formation of a sacrificial cubic phase, which is subsequently transformed into the hexagonal phase, is a widely accepted mechanism in the conventional co-precipitation and thermal decomposition process toward $NaLnF_4$ NPs.[108,120] With respect to microwave-assisted routes, Niu

et al. observed an α → β transformation with prolonged reaction time in an open-vessel microwave process, ultimately yielding pure β-$NaLnF_4$ microdisks.[121] To assess whether a similar phase transformation would occur in the closed-vessel microwave-assisted approach toward (ultra)small β-$NaGdF_4$:Yb^{3+},Er^{3+} NPs, we stopped the reaction after a predefined time interval once the reaction mixture reached its set temperature T_1 of 260 °C (T_2 was set to 250 °C). These time intervals were 1 s and 1 min (note that 1 s was not long enough to reach T_2; after 1 s, the reaction mixture was still at T_1). After 1 min, T_2 was reached. [$Ln(TFA)_3$] and [$Ln(OA)_3$] were chosen as precursors representing those that give access to sub-10 nm and sub-5 nm NPs, respectively. TEM images shown in Figure 22 confirmed that NPs of poorly defined morphology were obtained at the shortest reaction time (rise time to T_1 + 1 s) when [$Ln(TFA)_3$] was used as precursor (estimated NP size: 3.1 ± 0.6 nm, Figure 23a). After 1 min at 250 °C, the NPs reached a diameter of 4.5 ± 0.6 nm. Further size increase to 5.6 ± 0.6 nm was observed after 10 min of microwave irradiation at 250 °C (Note that the size of this batch of NPs was in line with the size of those NPs shown in Figure 13c (ca. 5.7 nm) as well as the cores (ca. 7 nm) of the core/shell samples discussed further below), which demonstrates good reproducibility of the established protocol. According to XRD patterns recorded on these samples (Figure 22c and Figure S1 on page 93), the hexagonal phase is present from 1 s onwards. Yet, the peak broadening due to the small crystal size made it difficult to exclude the presence of any minor α-$NaGdF_4$ content. β-$NaGdF_4$ was observed as the only crystalline phase after 1 min, and this crystalline phase was retained at longer reaction times. Similar observations about morphology and crystalline phase were made when employing [$Ln(OA)_3$] as the precursor (Figure 22b-c, Figure 23b, and Figure S1). By increasing the reaction time to 1 min, the very small NPs obtained after 1 s (estimated size: 2.6 ± 0.3 nm) grew in diameter to 3.0 ± 0.4 nm.

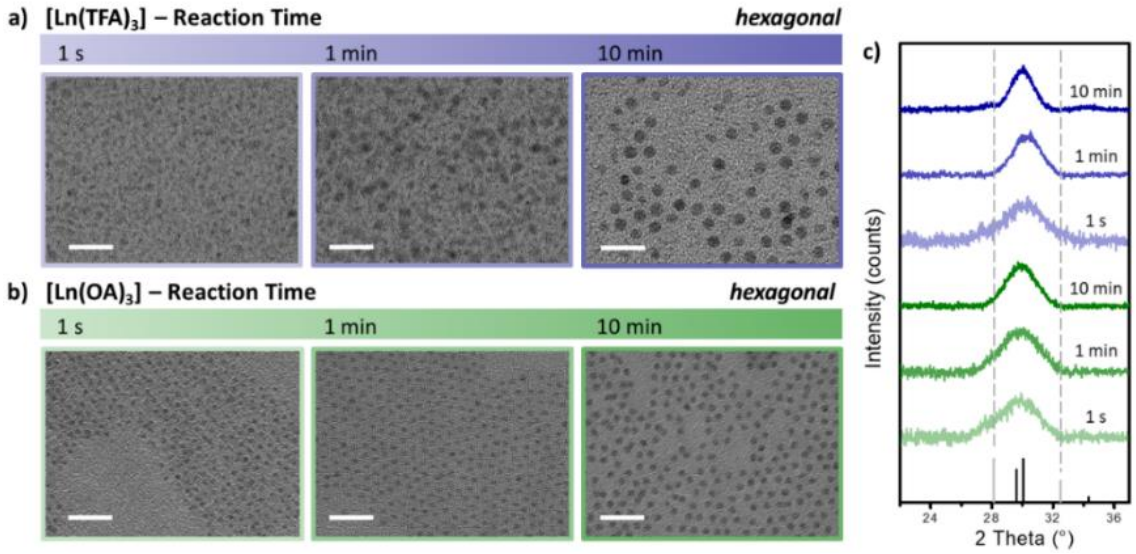

Figure 22. Influence of the reaction time on NP formation. TEM images of NPs obtained from a) $[Ln(TFA)_3]$ and b) $[Ln(OA)_3]$ precursors, whereas the microwave-assisted heating was terminated 1 s, 1 min, and 10 min after reaching T_1 = 260 °C (T_2 = 250 °C). Na^+-to-Ln^{3+} ion ratios were set to promote the formation of the hexagonal phase. c) Associated XRD patterns of the NPs showing the range where the main reflections for the hexagonal and cubic phases of $NaGdF_4$ are expected. Dashed lines are guides for the eye marking the position of the main reflections of the cubic phase. References: β-$NaGdF_4$ (PDF#: 01-080-8787, black lines), α-$NaGdF_4$ (PDF#: 00-027-0697, light grey lines). Full XRD patters are given in the annexe (Figure S1). Scale bars in TEM images are 20 nm.

Further prolonging the reaction time induced only minor additional increase in size to 3.2 ± 0.3 nm. At the earliest stage of the microwave-assisted decomposition of $[Ln(OA)_3]$, the potential presence of minor amounts of crystalline cubic phase could not be ruled out due to peak broadening, As seen with $[Ln(TFA)_3]$. According to the results of this time-dependent study, there was no stage of phase-pure α-$NaGdF_4$:Yb^{3+},Er^{3+} even at the earliest time after reaching T_1. Instead, any possible α → β transformation must have taken place predominantly during the initial heating stage of the temperature profile prior to reaching T_1.

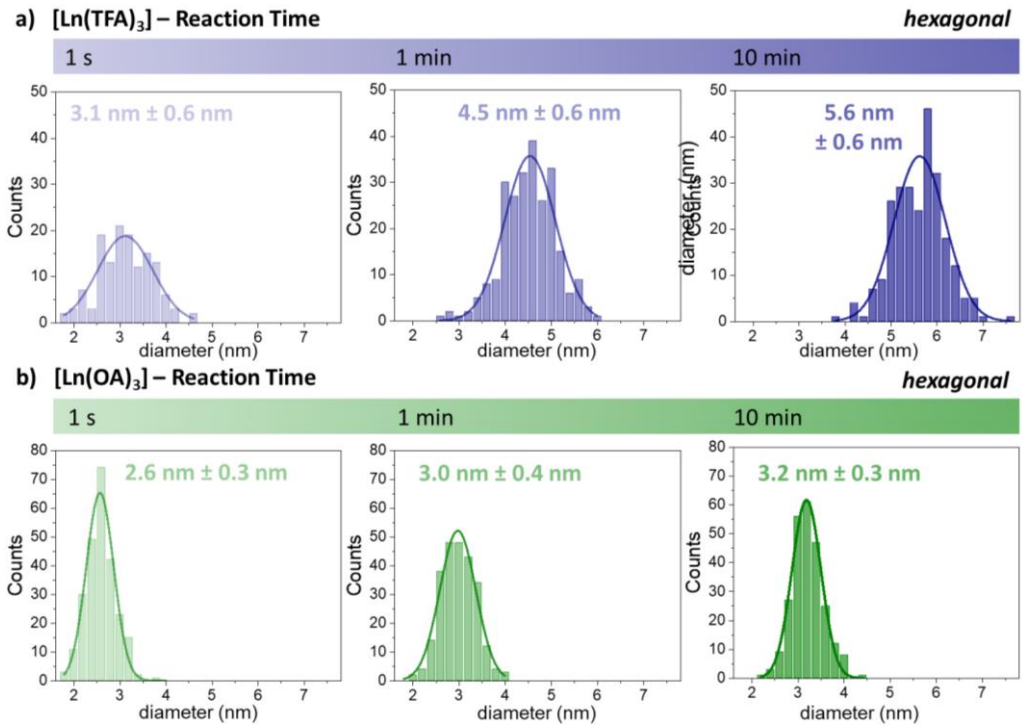

Figure 23. Influence of the reaction time on mean size and size distribution of β-$NaGdF_4$:Yb^{3+},Er^{3+} NPs synthesized using a) $[Ln(TFA)_3]$ and b) $[Ln(OA)_3]$ as precursors. Reaction times varied between 1 s and 10 min, as indicated in the figure. Reaction temperature T_2: 250 °C. The Na^+-to-Ln^{3+} ion ratio was set aiming for the hexagonal crystalline phase.

Similar observations were reported for the growth mechanism of larger β-$NaGdF_4$:Ln^{3+} nanorods obtained in a microwave-assisted hydrothermal synthesis using lanthanide nitrate as precursor.[121]

Previous studies using $[Ln(Ac)_3]$ as precursor in thermal decomposition processes suggested an *in situ* conversion of the $[Ln(Ac)_3]$ into $[Ln(OA)_3]$ during the degassing step in presence of OA.[122,123] However, the difference in optical quality observed in (Figure 19a-b) of the obtained NPs derived from $[Ln(Ac)_3]$ and $[Ln(OA)_3]$ points towards differences in the chemical conditions during NP synthesis. This was further supported by the slight differences in the crystalline phase of nuclei formed at the earliest stage of materials formation when $[Ln(OA)_3]$ or $[Ln(Ac)_3]$ was used as precursor. Respective XRD patterns shown in Figure 24a reveal that, at 200 °C, a phase mixture was obtained from $[Ln(OA)_3]$ and $[Ln(Ac)_3]$. The contribution of the hexagonal phase can be

estimated to be more pronounced for [Ln(Ac)$_3$]-derived NPs (broad peak more shifted towards the hexagonal reference) than for [Ln(OA)$_3$]-based NPs (broad peak more shifted towards the cubic reference). This indicates that both precursors, [Ln(OA)$_3$] and [Ln(Ac)$_3$], enable the formation of the hexagonal crystal phase already at an early stage of the reaction – [Ln(Ac)$_3$] promoting more the hexagonal phase formation.

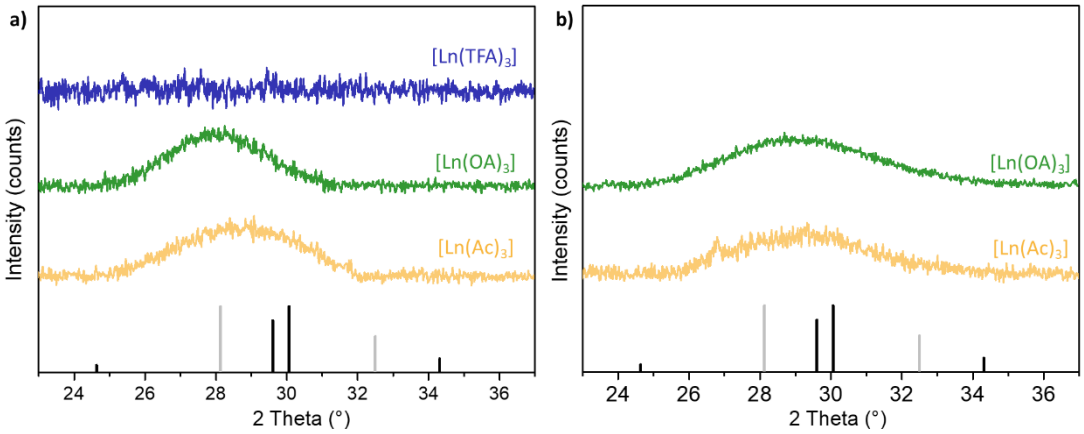

Figure 24. Assessment of the crystalline phase formation during the synthesis of β-NaGdF$_4$:Yb^{3+},Er^{3+} NPs. XRD patterns are shown for samples obtained using [Ln(TFA)$_3$], [Ln(OA)$_3$] and [Ln(Ac)$_3$] as precursors. a) The reactions were stopped when reaching a temperature of 200 °C and a pressure of ca. 1 bar. b) Using [Ln(OA)$_3$] and [Ln(Ac)$_3$] as precursors, the reactions were kept at 200 °C for 10 min. References: α-NaGdF$_4$ (PDF#: 00-027-0697, light grey lines), β-NaGdF$_4$ (PDF#: 01-080-8787, black lines).

In the case of [Ln(TFA)$_3$], no crystalline product was obtained at all even if the reaction was stopped at 230 °C, suggesting that the NPs likely crystallized in their hexagonal phase from the beginning and did not undergo any noticeable α → β phase transformation. To assess the influence of the reaction time on the α → β transformation at low temperature, the reaction time was prolonged to 10 min using [Ln(Ac)$_3$] and [Ln(OA)$_3$] as precursors. XRD patterns of the obtained products were like those of NPs obtained immediately after reaching 200 °C, indicating a cubic-hexagonal phase mixture (Figure 24b). These results provide evidence that the reaction temperature plays a key role in the α → β transformation, suggesting a thermodynamically controlled process. The observed differences in NP growth mechanism and phase formation at an

early reaction stage for [Ln(TFA)$_3$] *versus* [Ln(OA)$_3$] and [Ln(Ac)$_3$] can also be seen in light of the pressure profiles obtained during the microwave-assisted decomposition of the three precursors (Figure 18): as indicated by the continuously increasing pressure, the nucleation process was not completed yet at the early stage of heating in case of [Ln(TFA)$_3$]. Oppositely, a plateau – indicative of an already started NP growth – was reached in the case of [Ln(OA)$_3$] and [Ln(Ac)$_3$].

Overall, these findings provide evidence that the microwave-assisted synthesis conditions strongly favour the α → β transformation of ultrasmall $NaGdF_4$ NPs in comparison to conventional routes, when specific precursor concentration and ratios are selected. Herein, the short reaction time in which β-$NaGdF_4$:Yb^{3+},Er^{3+} was formed indicates that nucleation and material formation kinetics are accelerated under solvothermal microwave-assisted conditions.

4.2.2 Optical properties of nanoparticles obtained at different reaction times.

For NPs derived from [Ln(TFA)$_3$], the photoluminescence intensities increased with increasing reaction time (Figure 25a), whereas the gain in intensity was particularly significant when the reaction time increased from 1 to 10 min. A similar increase was observed for [Ln(OA)$_3$]-derived NPs when the reaction time was extended from 1 to 10 min, while no increase was observed between 1 s and 1 min (Figure 25b). Given the minimal size increase upon prolonging the reaction time (particularly for [Ln(OA)]$_3$-derived NPs), this enhanced optical performance speaks for the fact that the NPs were more crystalline and/or contained fewer defects in their crystal structure – acting as possible photoluminescence quenching centres – after longer reaction times.

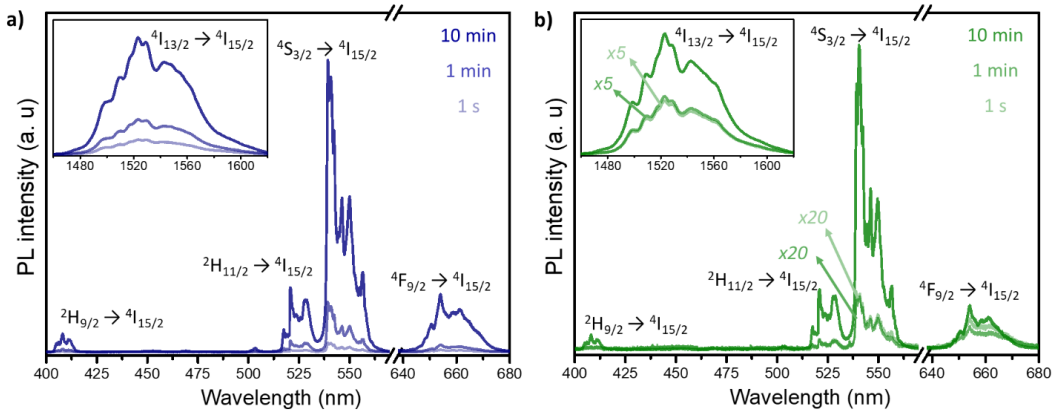

Figure 25. Influence of the reaction time on the visible and NIR (inset) photoluminescence upon 980-nm excitation of NPs synthesized using a) [Ln(TFA)$_3$] and b) [Ln(OA)$_3$] as precursors. Reaction temperature T_2: 250 °C. The Na^+-to-Ln^{3+} ion ratio was set to obtain the hexagonal phase.

4.2.3 Effect of reaction temperature

To investigate the potential effects of the reaction temperature on crystalline phase and size, the reaction temperature T_2 was reduced or increased by 10 °C to 240 °C and 260 °C, respectively (T_1 always being 10 °C higher than T_2 as described in Chapter 3. The reaction time was kept constant at 10 min and the Na^+-to-Ln^{3+} ratio was set to foster the formation of β-$NaGdF_4$:Yb^{3+},Er^{3+}. TEM images and XRD patterns of the NPs obtained from [Ln(TFA)$_3$] and [Ln(OA)$_3$] at 240 °C, 250 °C, and 260 °C, respectively, are shown in Figure 26. NPs were obtained regardless of the set temperature, without any apparent change in morphology. Using [Ln(TFA)$_3$] as the precursor, no clear trend correlating reaction temperature and NP size was found, with NP sizes within the 5.0-to-5.6 nm realm (Figure 26a and Figure 27a). Similarly, using [Ln(OA)$_3$] as the precursor, size distributions based on TEM showed little variation between the different thermal reaction conditions, resulting in sizes ranging from 3.2 ± 0.4 nm to 4.0 ± 0.4 nm with increasing reaction temperature (Figure 27b and Figure 28b). Noteworthy, even at lower temperature, phase-pure β-

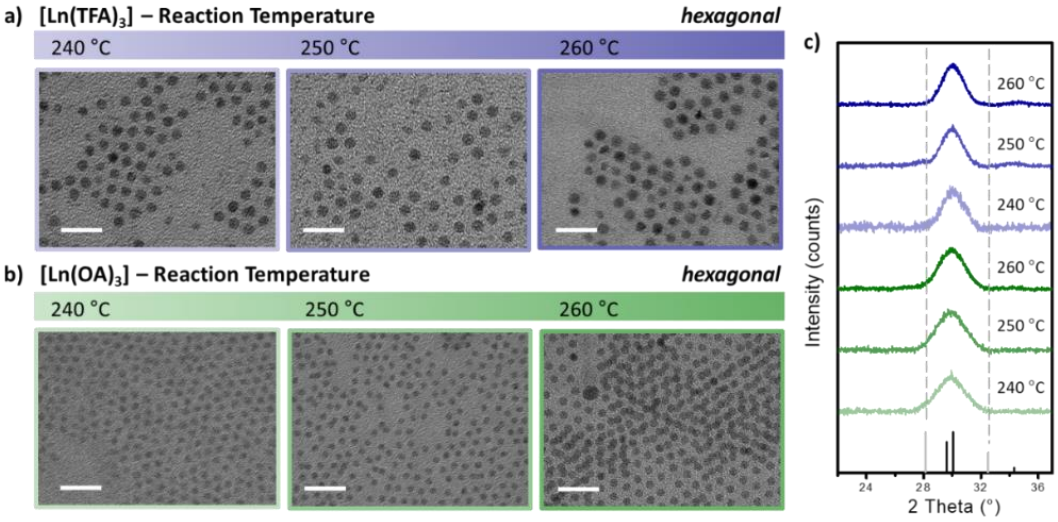

Figure 26. a) to c): Influence of the reaction temperature on NP formation. TEM images of NPs obtained at different reaction temperatures (T_2) using a) [Ln(TFA)$_3$] and b) [Ln(OA)$_3$] precursors. c) Associated XRD patterns of the NPs presented. References: β-$NaGdF_4$ (PDF#: 01-080-8787, black lines), α-$NaGdF_4$ (PDF#: 00-027-0697, light grey lines). Dashed lines are guides for the eye marking the position of the main reflections of the cubic phase. Full XRD patters are given at the ESI (Figure S1). Scale bars are 20 nm.

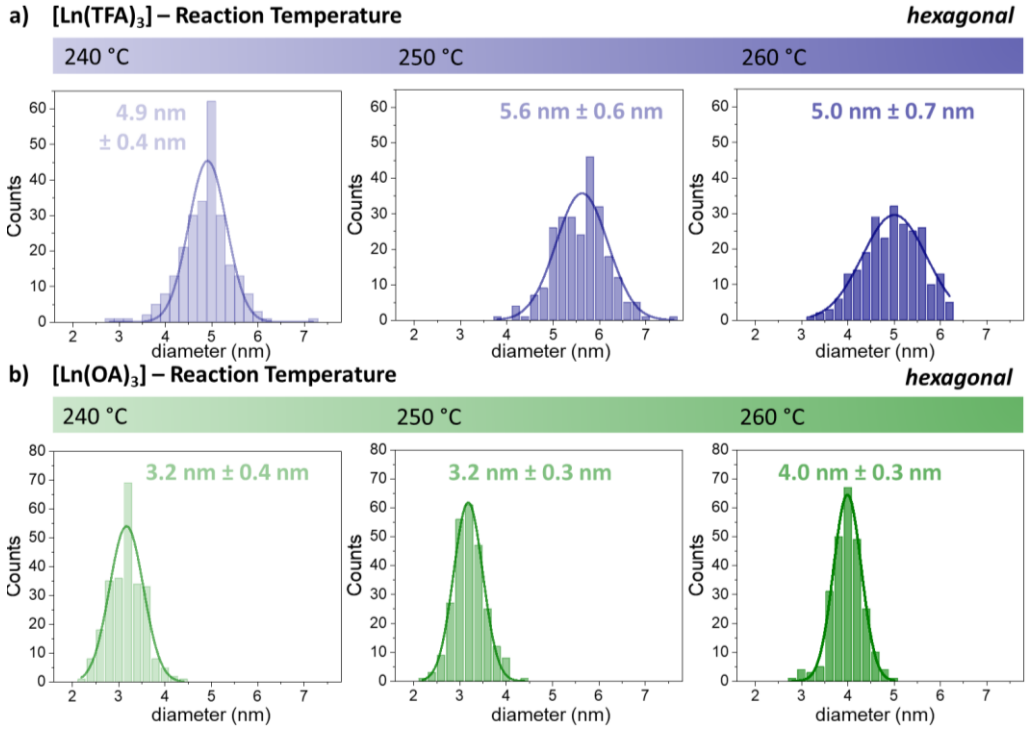

Figure 27. Influence of the reaction temperature (T_2) on mean size and size distribution of $NaGdF_4$:Yb^{3+},Er^{3+} NPs synthesized using a) [Ln(TFA)$_3$] and b) [Ln(OA)$_3$] as precursors. Reaction time: 10 min. The Na^+-to-Ln^{3+} ion ratio was set aiming for the hexagonal crystalline phase.

NPs were derived from both precursors (Figure 26c). Consequently, the here developed reaction protocol does not only kinetically but also thermodynamically favors the formation of the hexagonal phase resulting in a complete α → β transformation at temperatures lower and reaction times shorter than in conventional decomposition processes.

4.2.4 Optical properties of nanoparticles obtained at different reaction temperatures

G/R ratios larger than 1 (Figure 28) for all samples analyzed under the temperature study are in line with findings by XRD analysis (Figure S1), showing the presence of the hexagonal phase for all temperature conditions. The photoluminescence spectra further reveal that, for both $[Ln(TFA)_3]$- and $[Ln(OA)_3]$-derived NPs, an increase in reaction temperature from 240 °C to 250 °C or 260 °C enhanced the overall upconversion PL intensity. Generally speaking, such trend can be associated with two main aspects: NP size increase and/or the fact that higher temperatures favor the healing of defects in the NP volume as well as at the NP surface. Given the limited variation in NP size as a function of temperature (Figure 28), the observed increase in the visible upconversion emission intensity upon increase of the reaction temperature can likely be ascribed to improved crystal quality, *i.e.*, healing of defects and better crystallinity (Figures 27c and Figure

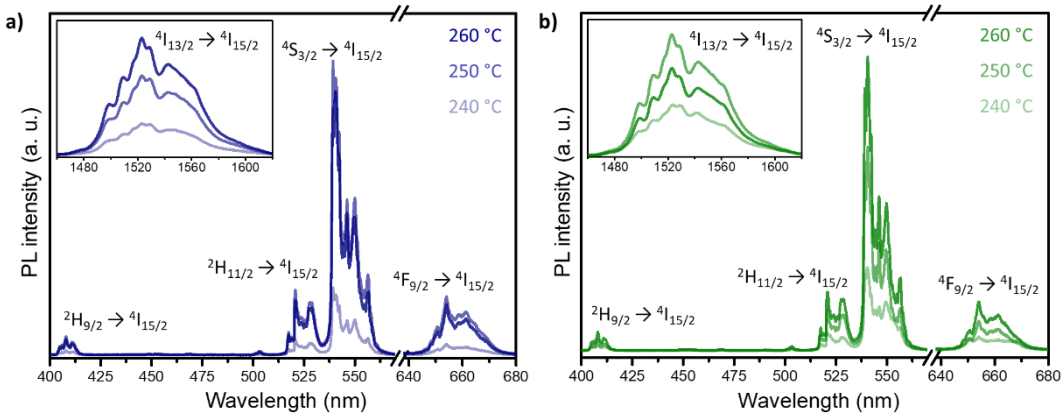

Figure 28. Influence of the reaction temperature on the visible and NIR (inset) photoluminescence upon 980-nm excitation of NPs synthesized using a) $[Ln(TFA)_3]$ and b) $[Ln(OA)_3]$ as precursors. Reaction time was t_2: 10 min. The Na^+-to-Ln^{3+} ion ratio was set to obtain the hexagonal phase.

S1). Similarly, for the emission in the NIR spectral region, higher intensities were obtained for samples prepared at either 250 °C or 260 °C. Yet, overall, the photoluminescence enhancement upon temperature increase was less dramatic as in case of prolongation of the reaction time.

4.3 Photoluminescence enhancement by $NaGdF_4$ shell growth

A major challenge with respect to very small NPs is the reduced photoluminescence intensity due to their large surface area and therewith related interaction with the environment, *e.g.*, solvent molecules, as well as surface defects that can act as photoluminescence quenchers. The most common strategy to circumvent this issue is to grow a protecting shell around the luminescent core, resulting in core/shell architectures.[118,119,124] The successful shell growth through the developed microwave-assisted synthesis route is demonstrated in Figure 29. Undoped $NaGdF_4$ shells were grown on hexagonal and cubic core-only NPs obtained from each of the studied precursors. Due to the enhanced efficiency of the $[Ln(TFA)_3]$ precursor in terms of thermal decomposition and NP formation, $[Gd(TFA)_3]$ was used as shell precursor, irrespectively of the chemical history of the core-NPs. Shells were successfully grown within 10 min of microwave irradiation at 230 °C, whereas the shell thickness varied as a function of the initial core size. Size distributions of NPs pre- and post-shell growth are shown in Figure 29a-d revealing shell thicknesses of approximately 2.5, 2.2, and 1.4 nm around hexagonal-phase core-only NPs derived from $[Ln(TFA)_3]$, $[Ln(OA)_3]$, and $[Ln(Ac)_3]$, respectively. A shell of 1 nm was grown above the

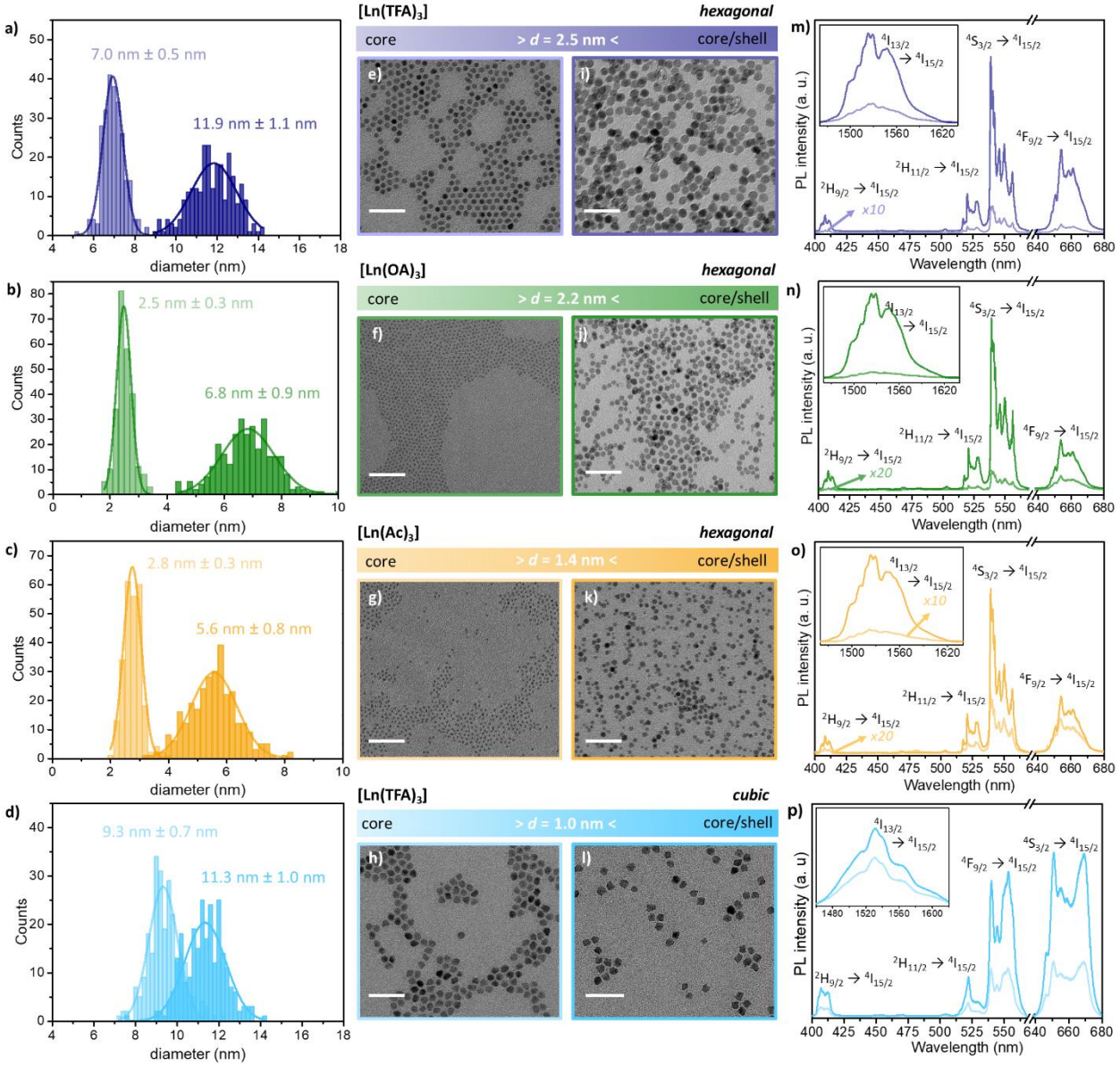

Figure 29. a-d) Size distribution of core-only and core/shell NPs: hexagonal-phase cores were grown using $[Ln(TFA)_3]$, $[Ln(OA)_3]$ or $[Ln(Ac)_3]$ as precursors, cubic-phase NPs were grown using $[Ln(TFA)_3]$ precursors; shells were synthesized using $[Ln(TFA)_3]$ as precursor. e-l) Corresponding TEM images of core-only as well as core/shell NPs. m-p) Associated photoluminescence in the visible and NIR (insets) spectral regions. Reaction temperatures: 250 °C for core NPs and 230 °C for shell growth. Reaction time: 10 min for core and shell growth each. Scale bars are 50 nm. Comparison between core and core/shell NPs are shown in Table S1 on page 92.

cubic-phase core-only NPs. Following shell growth, the NPs retained their cubic or hexagonal crystalline phase (Figure 30) and homogeneous size distribution (Figure 29a-d). As expected, shell

growth greatly enhanced the photoluminescence intensity in the visible and NIR spectral regions (Figure 29m-p) of all NPs, irrespective of the precursor or crystalline phase.

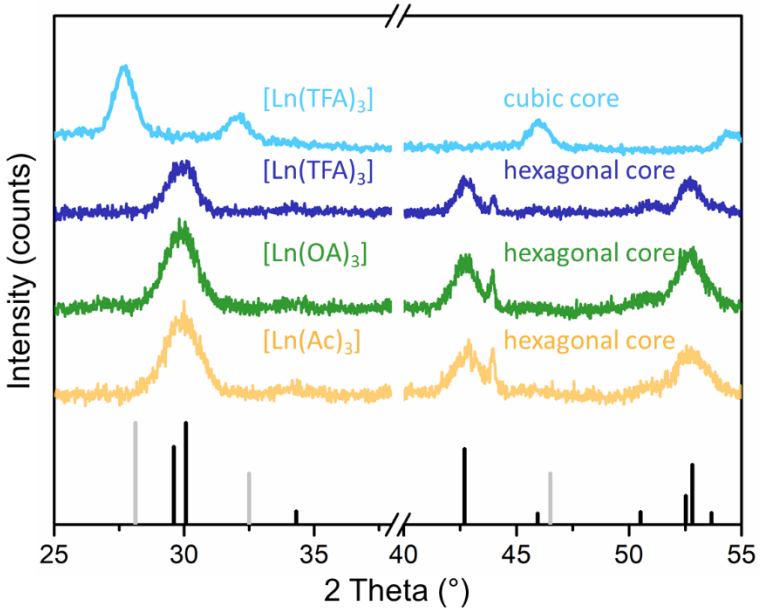

Figure 30. XRD patterns of core/shell NPs. The shells were grown using $[Ln(TFA)_3]$ as precursor within 10 min on $[Ln(TFA)_3]$-, $[Ln(OA)_3]$-, and $[Ln(Ac)_3]$-derived NPs. Reference: α-$NaGdF_4$ (PDF#: 00-027-0697, light grey lines), β-$NaGdF_4$ (PDF#: 01-080-8787, black lines). Reflections at 39° due to NaF were removed for clarity. The reflection at 44° is due to the sample holder.

Indeed, the upconversion emission capability of the NPs was improved to the point that it became visible to the naked eye under excitation with a simple, hand-hold NIR laser pointer (power: 50 mW, Figure 31). When seeking real-life, optical-based applications, the brightness of the upconverted emission is one important aspect. In addition, the possibility to trigger emission by simple means of excitation – *i.e.,* without the need for a sophisticated set-up – can constitute a further asset. Remarkably, despite their small size – sub-10 nm in case of $[Ln(OA)_3]$- and $[Ln(Ac)_3]$-derived core/shell NPs, sub-15 nm in case of $[Ln(TFA)_3]$-derived core/shell NPs (Figure 31) – the α-phase sample exhibited orange and all β-phase samples showed green upconversion emission, visible by naked eye.

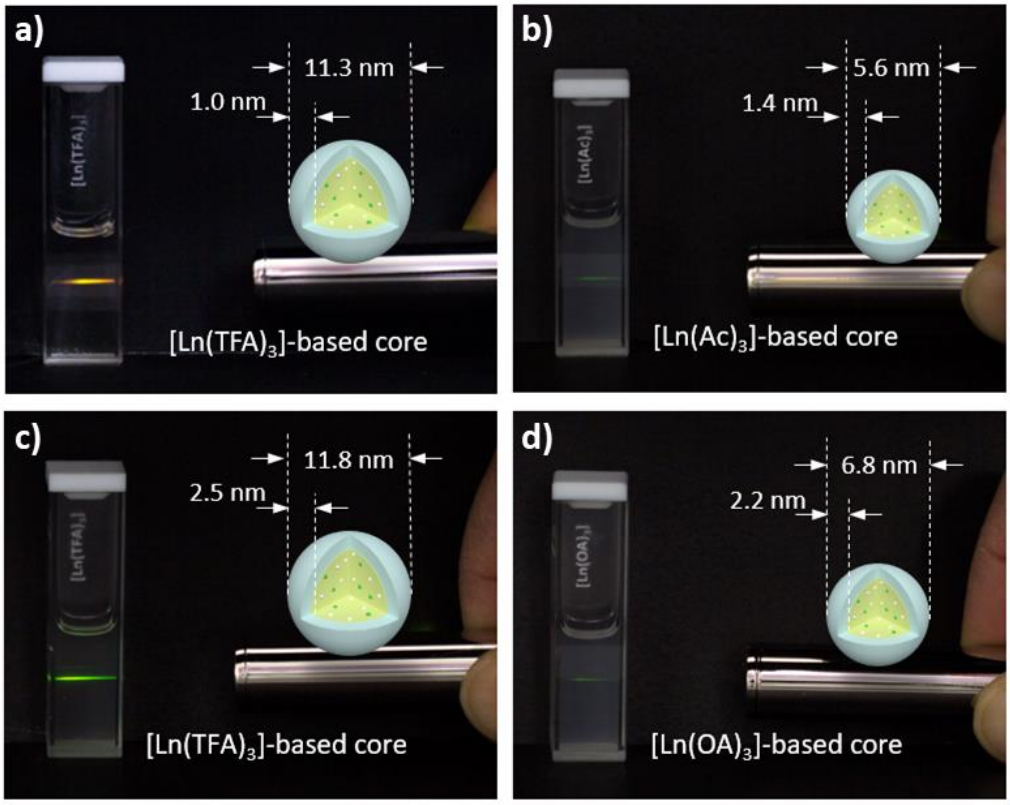

Figure 31. Photographs of a) α-$NaGdF_4$:Yb^{3+},Er^{3+}/$NaGdF_4$ and β-$NaGdF_4$:Yb^{3+},Er^{3+}/$NaGdF_4$ core/shell NPs made from b) $[Ln(Ac)_3]$, c) $[Ln(TFA)_3]$ and $[Ln(OA)_3]$-based core NPs. All NPs were dispersed in toluene under excitation with a 980 nm (P = 50 mW) laser pointer. NP concentration was 16 $g \cdot L^{-1}$ for cubic-phase core/shell NPs. For the hexagonal-phase core/shell NPs, the NP concentrations were 25.5 $g \cdot L^{-1}$, 38.0 $g \cdot L^{-1}$ and 16 $g \cdot L^{-1}$ for $[Ln(OA)_3]$, $[Ln(Ac)_3]$ and $[Ln(TFA)_3]$-derived NPs, respectively.

Table 4. Lifetime values, corresponding NP sizes and shell thicknesses of α-and β-$NaGdF_4$:Yb^{3+},Er^{3+} core/shell NPs

Core Precursor [a]	**Crystal Phase**	**Lifetime (μs)**		**Approx. NP Size (nm)**	**Shell Thickness (nm)**
		$^4S_{3/2} \rightarrow {}^4I_{15/2}$ **[540 nm]**	$^4F_{9/2} \rightarrow {}^4I_{15/2}$ **[655 nm]**		
$[Ln(TFA)_3]$	β	156	156	11.8	2.5
$[Ln(OA)_3]$		103	127	6.8	2.2
$[Ln(Ac)_3]$		73	87	5.6	1.4
$[Ln(TFA)_3]$	α	25	43	11.3	1.0

[a] For shell growth, $[Ln(TFA)_3]$ were used as precursors.

As expected, dispersions of higher NP concentration were required in the case of the sub-10 nm UCNPs, while bright emission was obtained from the larger, ca. 11 nm and 12 nm-sized sample, even at lower concentrations.

As expected, the presence of the shell resulted in the increase of the lifetime for all type of NPs and both green ($^4S_{3/2}$) and red ($^4F_{9/2}$) emission (Table 4 and Figure 32), which correlate with the enhancement of the PL (Figure 29m-p and Figure 31). The improvement can be attributed to the removal of quenching by surface defects and solvents, which are major nonradiative relaxation pathways.[125] The corresponding lifetimes of the green emitting level obtained for the largest [Ln(TFA)$_3$]-based core/shell NPs (156 µs, 11.8 nm with a 2.5-nm shell) were below 200 µs (Table 4 and Figure 32). This is in line with findings by Würth *et al.* for similar-sized core/shell NPs (10.5 nm, with a 3.7 nm $NaGdF_4$:Yb^{3+},Er^{3+} core, and 3.4-nm $NaYF_4$ shell).[118] Yet, remarkably, these values were higher than the lifetime reported in the literature for 17-nm core-only $NaGdF_4$:Yb^{3+},Er^{3+} NPs (74 µs).[32] Thus, despite being small, the developed core/shell NPs have lifetimes similar to or longer than those of larger core-only NPs of similar elemental composition.

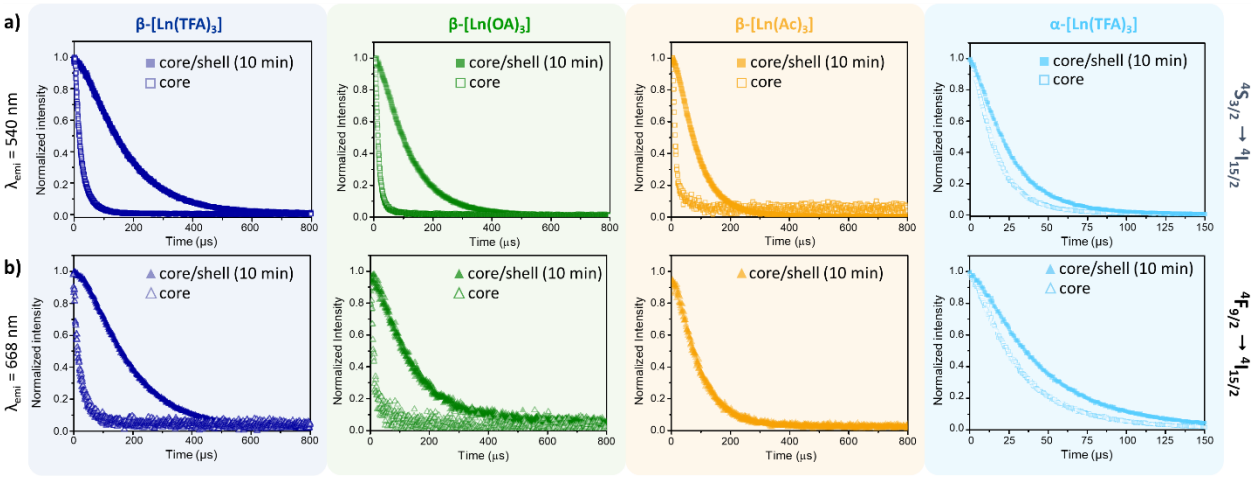

Figure 32. Decay curves of the a) 4S3/2 → 4I15/2 (540 nm) and b) 4F9/2 → 4I15/2 (650 nm) transitions for core-only and core/shell α- and β-NaGdF4:Yb3+,Er3+ NPs synthesized using [Ln(TFA)3], [Ln(OA)3], and [Ln(Ac)3] as precursors. All decay curves were obtained under 980-nm pulsed laser excitation.

This speaks for the efficiency of the employed shelling procedure in passivating the NPs' surface.[32,119,126] Consequently, the developed microwave-assisted protocol constitutes a rapid pathway toward small-yet-bright UCNPs.

4.4 Chapter conclusion

A microwave-assisted synthesis method was developed, providing rapid access to small (sub-10 nm) and ultrasmall (sub-5 nm) upconverting and NIR-emitting $NaGdF_4$ NPs doped with 2% of Er^{3+} and 20% of Yb^{3+}. Remarkably, using lanthanide trifluoroacetates as precursors, *i.e.* $[Ln(TFA)_3]$, control over the crystalline phase of the resulting NPs was achieved upon rigorous adjustment of the reaction conditions, namely temperature, precursor concentration, and Na^+-to-Ln^{3+} ion ratio. This was – to the best of my knowledge – the first example of selective access to $NaGdF_4$:Yb^{3+},Er^{3+} NPs in either their cubic (α) or hexagonal (β) crystalline phase by microwave-assisted decomposition of $[Ln(TFA)_3]$, while retaining NPs sizes below 10 nm. β-$NaGdF_4$:Yb^{3+},Er^{3+} NPs in the 3-nm realm were obtained by choosing lanthanide oleates or acetates – $[Ln(OA)_3]$ or $[Ln(Ac)_3]$ – as precursors. Application of the latter commercially available precursor was found particularly intriguing as making time-consuming precursor synthesis steps obsolete. The chemical nature of the three precursors used for the NP synthesis was shown to have strong influence on their thermal decomposition behaviour. This was reflected in altered resulting pressure in the reaction vessel, which ultimately impacted the NPs size of the final product. XRD analysis of NPs obtained from $[Ln(OA)_3]$ and $[Ln(Ac)_3]$ precursors after different reaction times and at various reaction temperatures provided evidence for a rapid and complete thermodynamic controlled α → β phase transformation within initial heating stage of the reaction. No direct evidence for such phase transformation was found when $[Ln(TFA)_3]$ was used as precursors, indicating a growth mechanism that is strongly in favour of the hexagonal phase. The results of

the study suggest that nucleation and α → β phase transformation is temperature-dependent and as such, thermodynamically-control processes. Overall, this allowed for short reaction times (10 min) and relatively low reaction temperatures (250 °C in case of hexagonal, 230°C in case of cubic NPs, respectively). Despite their small size, all NPs exhibited upconversion and NIR emission, which was brighter for the larger [$Ln(TFA)_3$]-derived NPs. Importantly, the developed microwave-based protocol also provides a strategy towards small, yet brightly emitting core/shell NPs, which are highly sought-after for, *e.g.* biomedical applications.

5 Combining upconverting nanoparticles with lanthanide-based complexes into a hybrid system film

Note: All figures presented in this chapter are reprinted (adapted) with permission from R. Marin, I. Halimi, D. Errulat, Y. Mazouzi, G. Lucchini, A. Speghini, M. Murugesu and E. Hemmer, ACS Photonics, 2019, 6, 436–445. Copyright (2019) American Chemical Society.

5.1 Background and aim of the study on the hybrid system

As explained in chapter 1, Ln-based upconverting nanoparticles (UCNPs) have been investigated as energy donor in combination with various energy acceptors, including Ln^{3+}-based complexes.[9–11,41–43] The route usually adopted to combine UCNPs and Ln-based complexes requires anchoring the molecules of the latter to the surface of the former through covalent bonding, using electrostatically-attached ligand on the surface of UCNPs. As such, it results in material applicable for sensing purposes.[11] In this study, the preparation of an UCNPs+Ln-based complexes hybrid system detaches from this type of approach. Specifically, a straightforward drop-cast method was used to prepare an hybrid system starting from a mixed solution of α-$NaGdF_4$:Yb^{3+}(20%),Tm^{3+}(0.5%) NPs and Ln-based complexes, thus eliminating the need for surface modification and covalent conjugation with the energy acceptor. The complexes chosen for this study were the UV-excitable $[(Tb)_2(bpm)(tfaa^-)_6]$ or $[(Eu)_2(bpm)(tfaa^-)_6]$, abbreviated on the following as $[Tb_2]$ or $[Eu_2]$. This system assembles in $[Tb_2]$ or $[Eu_2]$ needle-like crystal decorated with UCNPs. The optical properties of the so-prepared hybrid system were studied, with emphases on its light-harvesting capabilities in both the UV and NIR wavelength range. As part of this study, an investigation on the energy transfer process (ET) between the UCNPs and the $[Ln_2]$ was performed.

5.2 Optical and crystalline properties of upconverting nanoparticles and lanthanide-based complexes

5.2.1 Characterization of the upconverting nanoparticles and [Tb_2] and [Eu_2]

The α-$NaGdF_4$:Yb^{3+},Tm^{3+} NPs were selected as the energy donor in the hybrid system due to the good upconverting performance of this host-lattice/dopant combination under NIR excitation.[83,127] (*Note: the protocol for the synthesis of hexagonal UCNPs was not yet established when this study was carried out.*) The choice of Yb^{3+} and Tm^{3+} as the sensitizer and activator pair for the preparation of UCNPs was dictated by the superior capability of this combination of dopants to provide high-energy (*i.e.*, blue and UV) upconverted emission compared to other Yb^{3+}/Ln^{3+} ion combinations, such as Yb^{3+}/Er^{3+} ion pair described in chapter 4.[59,124,127] Moreover, it displays a spectral distribution of the emission lines, particularly favorable for the developed hybrid system (*vide infra*). An alternative form of the before described [$Ln(TFA)_3$] route was used in this study for the microwave-assisted synthesis of the NPs. In short, 1.25 mmol of [$Ln(TFA)_3$] was prepared from 0.497 mmol of Gd_2O_3 (180.1 mg), 0.125 mmol of Yb_2O_3 (49.3 mg, 20% doping) and 3.13 µmol of Tm_2O_3 (1.2 mg, 0.5% doping). The Ln^{3+} concentration was 0.125 mol·L^{-1}, the Na^+-to-Ln^{3+} ion ratio was set to 1:1, and T_1 and T_2 were 300 °C (1 s) and 260 °C (10 min), respectively. This allowed for the straightforward preparation of monodisperse, quasi-spherical UCNPs crystallized in the cubic phase with an average diameter of 7.3 ± 0.9 nm (Figure 33a-c). The prepared sub-10 nm UCNPs displayed upconverting emission under 980-nm laser irradiation, characterized by the presence of a Tm^{3+} emission at 450 nm, 480 nm and 650 nm (Figure 33d). [Tb_2] and [Eu_2] complexes were used in this study (Figure 33e), due to their chemical and optical stability, which allows for the preparation of robust hybrid systems.[104] Their thorough structural characterization was previously reported in the literature.[128] Both [Tb_2] and [Eu_2] show optical

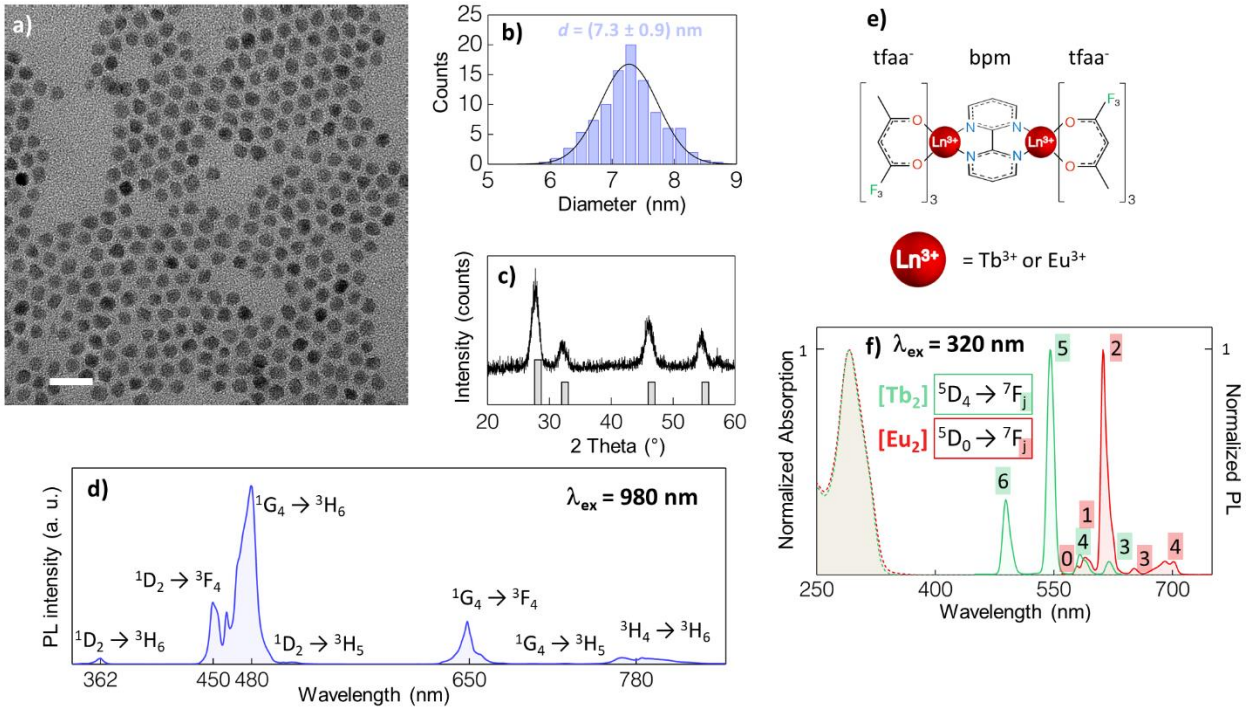

Figure 33. a) TEM image of α-$NaGdF_4$:Yb^{3+}(20%) Tm^{3+}(0.5%) NPs. b) Corresponding size distribution, c) XRD pattern (reference: α-$NaGdF_4$ (PDF #00-27-0697)), and d) upconversion spectra under 980-nm excitation of the UCNPs (due to UC). e) Molecular structure of the [Ln_2] complexes along with f) normalized diffuse reflectance (DRS) and emission spectra of [Tb_2] (green solid, f-f transitions $^5D_4$ to ^7F_j, j= 1 to 6) and [Eu_2] (red solid, f-f transitions $^5D_0$ to ^7F_j, j=1 to 5). Emission spectra were obtained under UV excitation.

absorption capabilities in the UV-blue wavelength range, enabled by the 2,2-bipyrimidine (bpm) and 1,1,1-trifluoroacetyl acetonate ($tfaa^-$) ligands. Hence, they feature a visible emission under UV (390 nm) excitation, which was centered at ca. 540 nm and 612 nm for [Tb_2] and [Eu_2] (Figure 33f).

5.2.2 Formation of the hybrid systems

The hybrid system (solid-state) was formed using a highly concentrated starting mixture containing a [Ln_2] and the UCNPs. The UCNPs-to-[Ln_2] mass ratio was set to 1:1 (40 mg·mL^{-1} each). The [Tb_2] or [Eu_2] were arranged in a continuous, dense film as demonstrated by optical microscopy and scanning electron microscopy (SEM) observations (Figure 34). SEM images show that in both cases, the morphology of this film was characterized by the presence of needle-like

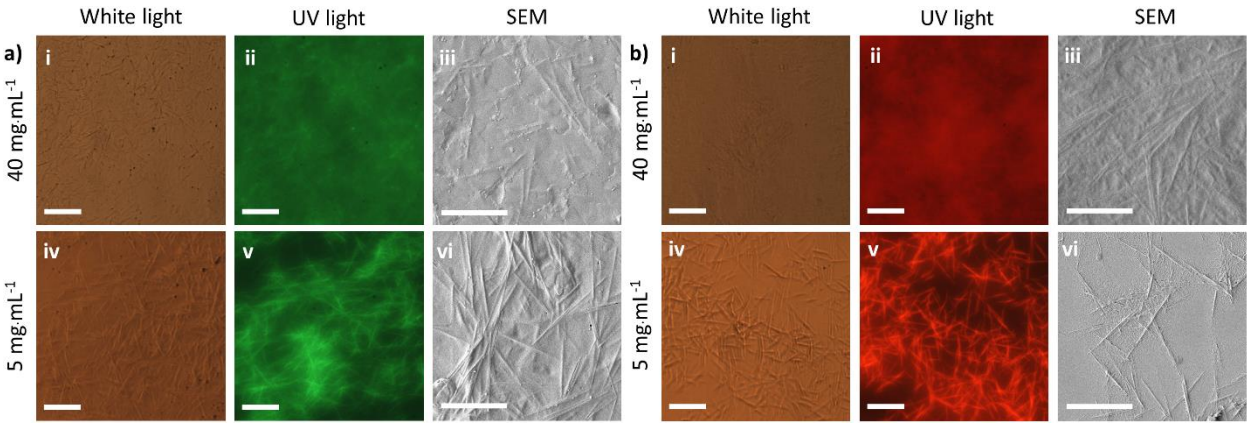

Figure 34. Micrographs of hybrid systems containing UCNPs and a) [Tb_2] or b) [Eu_2] acquired on an optical microscope (i, ii, iv, v) and corresponding SEM images (iii, vi) highlight a similar morphology of the two systems. A continuous distribution of complex molecules across the film (i, ii) or scattered needle-like crystals (iv, v) are observed at the starting solution's high and low concentration of UCNPs and complex, respectively. Scale bars are 20 μm for the micrograph acquired through the optical camera and 10 μm for the image acquired through SEM. Micrographs are presented in real colors.

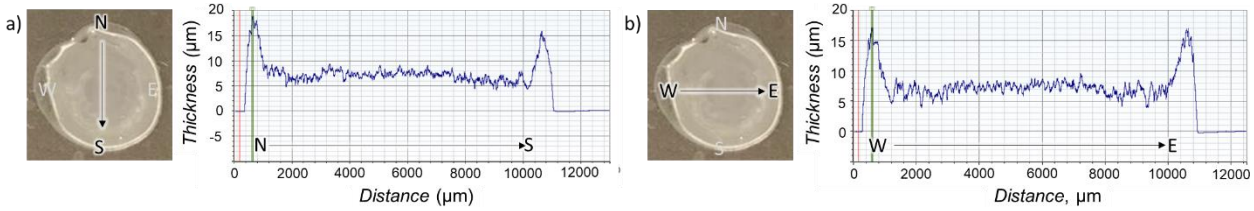

Figure 35. Profilometry scans of the film obtained from a mixture of UCNPs and [Tb_2] in a 1:1 mass ratio and a concentration of 40 mg·mL^{-1}. They had a thickness of approximately 7 ± 2 μm as determined from the scans executed along two orthogonal profiles (*i.e.*, a) – North-to-South, b) – West-to-East).

crystals embedded in a compact matrix overall featuring a relatively homogeneous emission Figure 34a-iii, Figure 34b-iii). At a concentration of 40 mg·mL^{-1}, the thickness of this film was determined to be approximately 7 ± 2 μm utilizing profilometry (Figure 35). Decreasing the concentration of both complex and UCNPs to 5 mg·mL^{-1}, the film became less dense, with the appearance of more isolated needle-like crystals (Figure 34a-vi, Figure 34b-vi).

These well- defined structures were covered by a much thinner layer of [Tb_2] or [Eu_2] molecules that did not organize in a distinct morphology. Direct observations of UCNPs in these hybrid systems via SEM was challenging since the solid-state systems were coated with a gold layer to

prevent charging phenomena. Although expected to be thin (approximately 3 nm), this layer was of the same order of magnitude of the UCNPs. Thus, it rendered impossible to discern the location of the UCNPs. However, direct evidence of the concomitant presence of the moieties was obtained via EDX analysis performed on a film prepared from a 40 $mg \cdot mL^{-1}$ concentrated dispersion of UCNPs and [Tb_2] (Figure 36a). The results confirmed the presence of all the expected elements of which the UCNPs and [Tb_2] are composed, with the notable exception of the Tm (due to low doping level). The EDX profiles obtained along Figure 36b-c of the film showed a homogeneous distribution of the elements of interest, confirming the continuous and concomitant presence of the two moieties used to prepare the film.

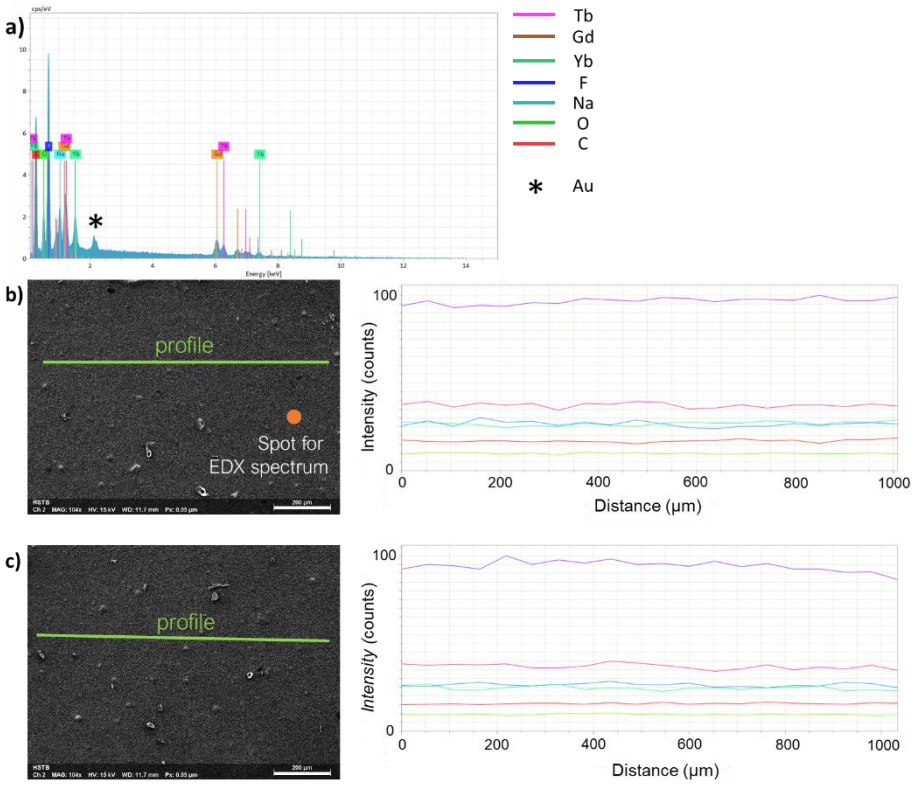

Figure 36. a) EDX spectrum recorded from the single spot in b) the UCNPs+[Tb_2] hybrid system. The signal from Tm was not detected due to the low doping concentration (0.5%). The signal from gold coating (required for SEM imaging) is highlighted with an asterisk. b) and c) EDX profile of the film. Scale bars in the SEM images in b) and c) are 200 µm.

The surface of the UCNPs is capped by OA^- ligands, which renders them highly hydrophobic and dispersible in organic solvent.[129] This OA^- hydrophobic layer is expected to prompt the interaction with the $tfaa^-$ moieties (Figure 33e) of the [Ln_2] complexes. TEM analysis of the hybrid system confirms the presence of [Ln_2] needle-like structures wrapped with a UCNPs "blanket" on their surface (Figure 37a). The validity of this assumption was confirmed by alternatively using UCNPs without OA^- ligands on their surface, *i.e.*, ligand-free UCNPs (Figure 37b, procedure described in section 3.4.1). Indeed, the absence of hydrophobic ligands on the UCNPs' surface hindered the formation of a film. Instead, ligand-free UCNPs tend to form separate clusters that do not cover the surface of the substrate evenly, also hindering the growth of [Tb_2] crystals. In the presence of the oleate-capped UCNPs, the complex crystals grow over a large scale, and the UCNPs cover them, assembling continuously.

To further probe this hydrophobic interaction between the moieties, a sample was prepared by casting a mixture of UCNPs and [Tb_2] directly on a carbon-coated copper grid. SEM observations

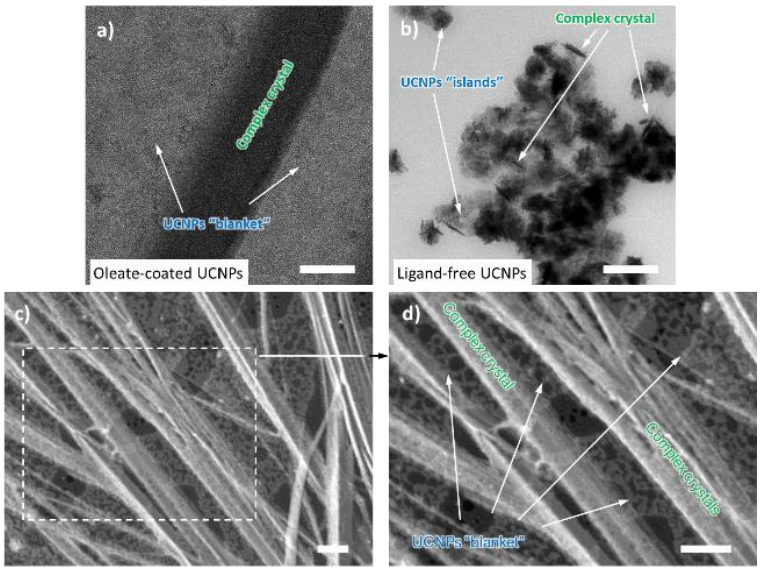

Figure 37. TEM images of hybrid systems prepared on TEM grids using the same concentration of UCNPs and [Tb_2] (approximately 10 mg mL^{-1} in a UCNPs-to-[Ln_2] mass ratio of 1:1) with a) OA^--coated or b) ligand-free UCNPs. c) and d) SEM images of the hybrid system presented in a) show the presence of large crystals covered by a "blanket" of UCNPs. Scale bars are 200 nm in a) and b) and 1 µm in c) and d).

on this specimen showed an arrangement of the UCNPs decorating the surface of the crystals of the complex (Figure 37c,d). The UCNPs' deposition is expected to be analogous to the one in the hybrid system prepared on glass slides, where the preferential accumulation of the UCNPs in correspondence of the surface of [Ln_2] crystals is also supported by hyperspectral imaging observations (*vide infra*). The effect that the UCNPs-to-[Tb_2] mass ratio ([Eu_2] is expected to behave similarly) has on the film morphology and the optical properties was also investigated. This systematic study showed that the best trade off in terms of film homogeneity, upconverted PL , and UV- and NIR-triggered [Tb_2] PL was realized with a 1:1 UCNPs-to-[Tb_2] mass ratio, despite the scattering in this film, as inferred by the recorded absorption spectrum (Figure S2-S5, page 94-97). Decreasing the concentration from 40 $mg \cdot mL^{-1}$ to 5 $mg \cdot mL^{-1}$ led to the formation of isolated [Tb_2] crystalline structure found at the edge of the film (Figure S6, page 98). Thus, when lowering the UCNP amount by mass ratio or the concentration, the complex aggregated and formed preferentially large crystals instead of distributing evenly throughout the film. As such, these results are further pieces of evidence that nonpolar interactions between the UCNPs (through the oleate ligands) and the [Tb_2] are fundamental to obtain a continuous film, whereas a decreased amount of UCNPs in the starting solution led to the formation of isolated islands of material on the glass substrate.

5.3 Optical behavior of the hybrid systems

5.3.1 Optical characterization

As explained in section 5.2.1, the [Ln_2] and UCNPs would emit under respectively UV and NIR irradiation (Figure 33e-f, Figure 38). The investigated complexes did not show emission under

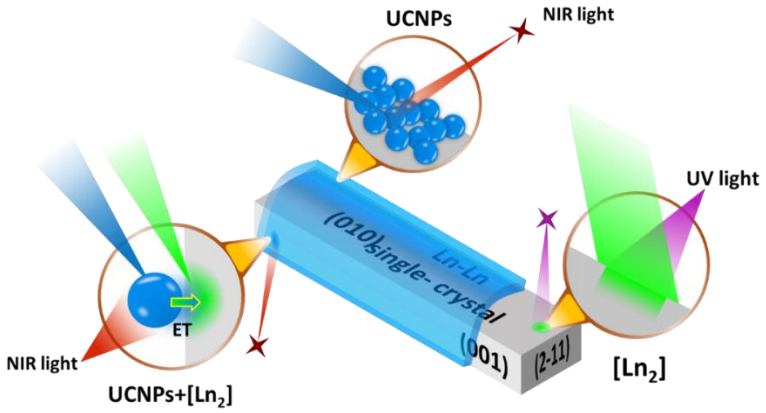

Figure 38. Scheme explaining the principle behind the hybrid system: Under UV excitation, the [Ln_2] complexes emit. Under NIR irradiation, UC emission from the NPs is triggered. In the hybrid system, bringing UCNPs and [Ln_2] close together, NIR excitation results in the simultaneous observation of emissions characteristic for UCNPs and [Ln_2].

continuous NIR excitation. In turn, the UNCPs were not emitting under UV excitation. In the hybrid systems, the [Ln_2] and UCNPs retain their sensitivity, or lack of, toward UV excitation. However, when the hybrid systems (obtained from 40 mg·mL^{-1} concentrated starting solution with a UCNPs-to-[Ln_2] mass ratio of 1:1) were irradiated with light of 980 nm, UC emission from the UCNPs and emission from the [Ln_2] complexes were observed (Figure 38).

The PL of both hybrid systems featured Tm^{3+} characteristic lines alongside the contributions of Tb^{3+} (547 nm), or Eu^{3+} (612 nm) sensitized emission (Figure 39). These results were accompanied by the marked quenching of Tm^{3+} emission bands that overlap with the absorption spectrum of the complexes (centered at 450 and 480 nm). The extent to which each band experienced quenching followed the superimposition between the specific Tm^{3+} emission and the excitation spectrum of the complex (Figure 39b). Altogether, these observations suggest that an energy transfer (ET) occurred between the UCNPs and the [Ln_2], which resulted from interactions between them. As such, the choice of sub-10 nm UCNPs for the preparation of the hybrid system derives from the need to maximize the surface effects that promote this type of interaction between the complexes and the UCNPs, favoring their proximity.

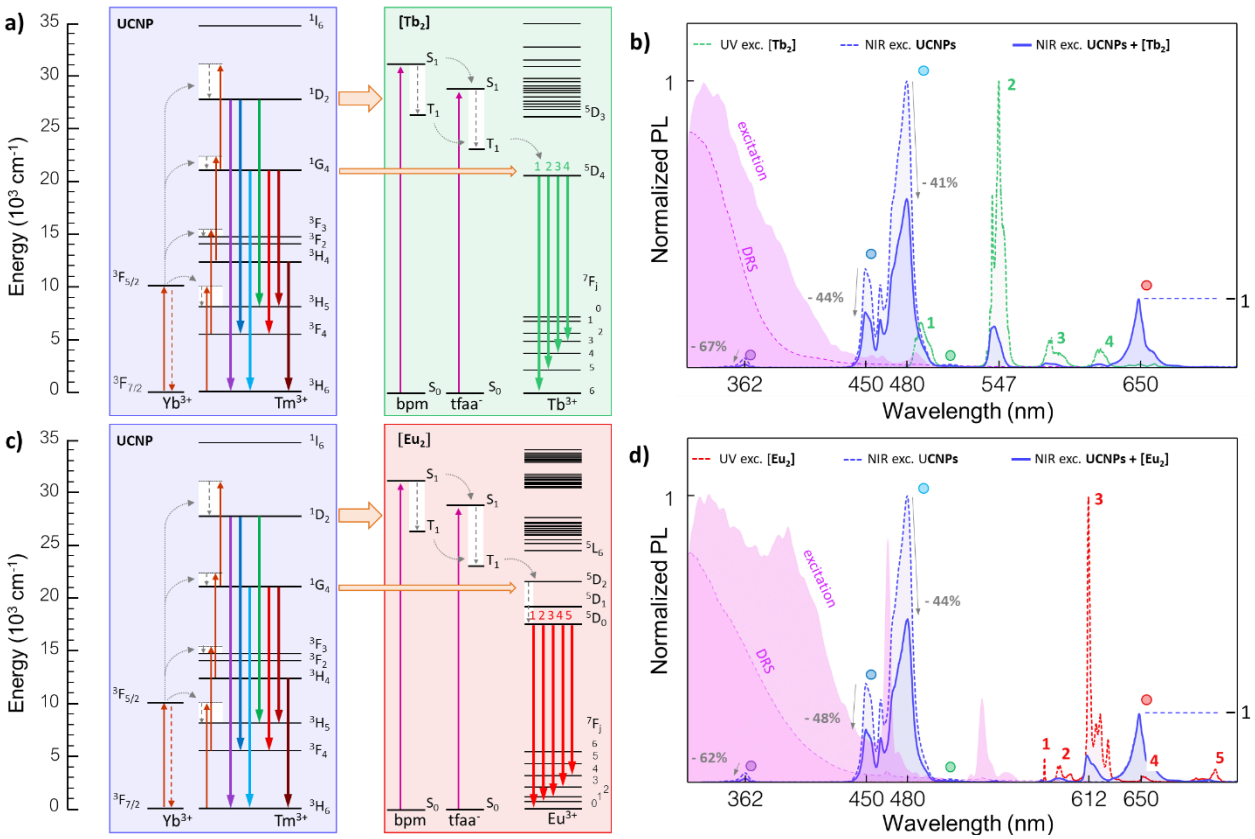

Figure 39. Energy level schemes of UCNPs amalgamated with a) [Tb_2] or c) [Eu_2] yielding the corresponding hybrid systems. Absorption and emission processes (solid upward and downward arrows), non-radiative processes (grey dashed arrows), ET mechanisms within each moiety (grey dotted arrows), and between UCNPs and the complex (centered yellowish arrows) are depicted. DRS and solid-state excitation spectra, UV-triggered [Ln_2] (green and red dashed lines), and NIR-triggered upconversion spectra (blue lines) emission spectra of b) [Tb_2] and d) [Eu_2] are reported.

5.3.2 Energy transfer mechanism

To better understand the interplay between UCNPs and the complexes, it is convenient to briefly lay out the mechanisms governing the optical properties of the complexes. [Tb_2] and [Eu_2] emission follows from the absorption of UV or blue photons that fosters the promotion of an electron to the S_1 level of the bpm and $tfaa^-$ ligands (Figure 39a). Through intersystem crossing and ET processes, the triplet state (T_1) of $tfaa^-$ gets populated. From there, the energy is transferred to the Ln^{3+} ions, where electron radiative de-excitation events take place, ultimately leading to the characteristic Tb^{3+} or Eu^{3+} emission (Figure 33f, Figure 39b).[130] The UC process with the

Yb^{3+}/Tm^{3+} ion pair is very similar to the one described for the Yb^{3+}/Er^{3+} ion pair (Figure 38a). The excitation energy is resonantly transferred from the Yb^{3+} $^3F_{7/2}$ level to the Tm^{3+} $^3H_5$ level. Additional ETs result in the Tm^{3+} excitation to the $^3F_3$, $^1G_4$ and $^1D_2$ levels, and the subsequent radiative relaxation. The bright ligand-sensitized emission of the investigated complexes proceeds from the favorable energy difference between the β-diketonate T_1 and the emitting level of Tb^{3+} ($^5D_4$) and Eu^{3+} ($^5D_0$) of 2680 and 5850 cm^{-1}, respectively, which limits back-energy transfer from Ln^{3+} to the ligands (Figure 39a). The Tm^{3+} quenched bands arise from the $^1D_2 \rightarrow {}^3H_6$ (362 nm), $^1D_2 \rightarrow {}^3F_4$ (450 nm), and $^1G_4 \rightarrow {}^3H_6$ (480 nm) f-f transitions, the latter being a three-photon order transition, while the other two are four-photon order processes.[131] As explained in section 4.1.5, the transition's photon order is the number of photons needed to populate the emitting level, and it is given by the slope of the emission intensity *versus* excitation power double logarithmic plot (Figure 40). For UCNPs alone, the obtained values for the $^1D_2 \rightarrow {}^3F_4$, $^1G_4 \rightarrow {}^3H_6$, and $^1G_4 \rightarrow {}^3F_4$ (650 nm) transitions were 2.56, 2.19, and 2.17, respectively (Figure 40a). These values were lower than the theoretically expected values of 4, 3, and 3, but are in line with reported values for similar fluoride-based Yb^{3+}/Tm^{3+}-doped UCNPs.[131] Discrepancies between theoretical and experimental values are common for nano-sized systems.[126,132] The observed slope values remained unchanged for UCNPs in both hybrid systems, and the indirectly triggered [Tb_2] or [Eu_2] emissions showcased a photon-order (2.89 and 2.77) in line with the highest photon-order transition of Tm^{3+} investigated ($^1D_2 \rightarrow {}^3F_4$ – 2.66 and 2.44 for the two systems) (Figure 40b-c). The slightly higher values observed from Tb^{3+} and Eu^{3+} implicate the involvement of $^1I_6$ level of the Tm^{3+} in the ET mechanism and provides evidence that the ET takes place preferentially from the higher energy level of Tm^{3+} to the ligand scaffold of the complex (Figure 38a). Indeed, if a direct ET from the Ln^{3+} ions inside (or on the surface of) the UCNPs to the Ln^{3+} ions in the complex would occur, it

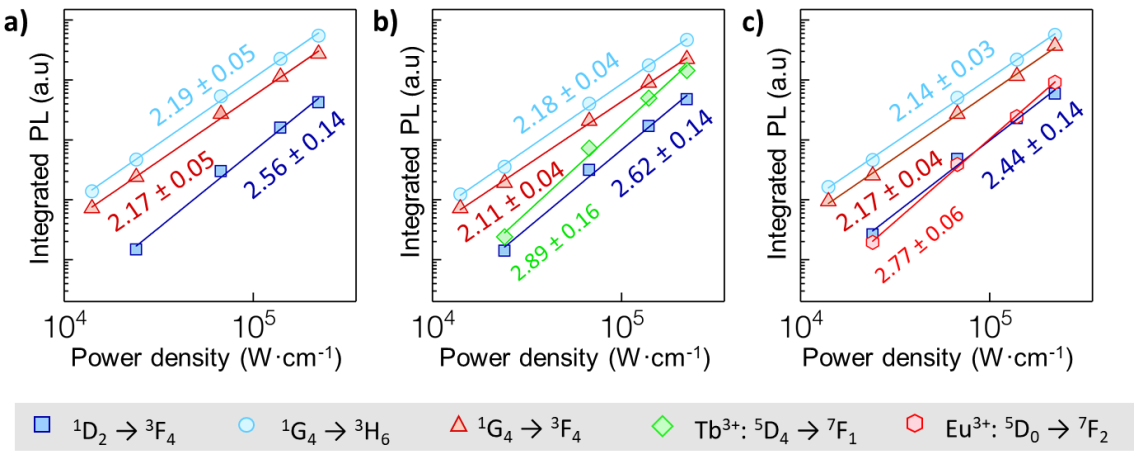

Figure 40. Integrated $^1D_2 \rightarrow {}^3F_4$, $^1G_4 \rightarrow {}^3H_6$, and $^1G_4 \rightarrow {}^3F_4$ Tm^{3+} emissions *vs* 980 nm excitation power density for a) UCNPs alone and amalgamated with b) [Tb_2] and c) [Eu_2], as well as NIR triggered Tb^{3+} and Eu^{3+} emissions.

would take place prominently from the more easily populated Tm^{3+}: $^1G_4$ level to Tb^{3+}: $^5D_4$ or Eu^{3+}: $^5D_{1,0}$ levels. This would result in an observed slope for [Tb_2] or [Eu_2] emission closer to the one of the Tm^{3+}: $^1G_4 \rightarrow {}^3H_6$ transition.

The predominant role played by the ligands in the ET mechanism was also confirmed by studying the behavior of a mixture of UCNPs and [Tb_2] in a chloroform dispersion (Figure 41). There, the quenching of the UCNPs emission and the energy transferred to the complex (hence the intensity of its sensitized emission) was limited as a consequence of the blue-shifted absorption of the complex in solution (Figure 42). This shift led to a reduced overlap between the emission and the absorption of the moieties involved in the ET mechanism, ultimately yielding a less efficient energy transfer. The Tm^{3+}:$^1D_2 \rightarrow {}^3F_4$ emission (450 nm) was quenched to an extent that depends on the amount of [Tb_2] complex added (Figure 41). Tm^{3+} transition $^1D_2 \rightarrow {}^3H_6$ (362 nm) was not detectable with the experimental setup employed for the study. Nonetheless, this transition is expected to play a major role in the transfer mechanism like in the solid-state hybrid system, due to its overlap with the excitation spectrum of the complex.

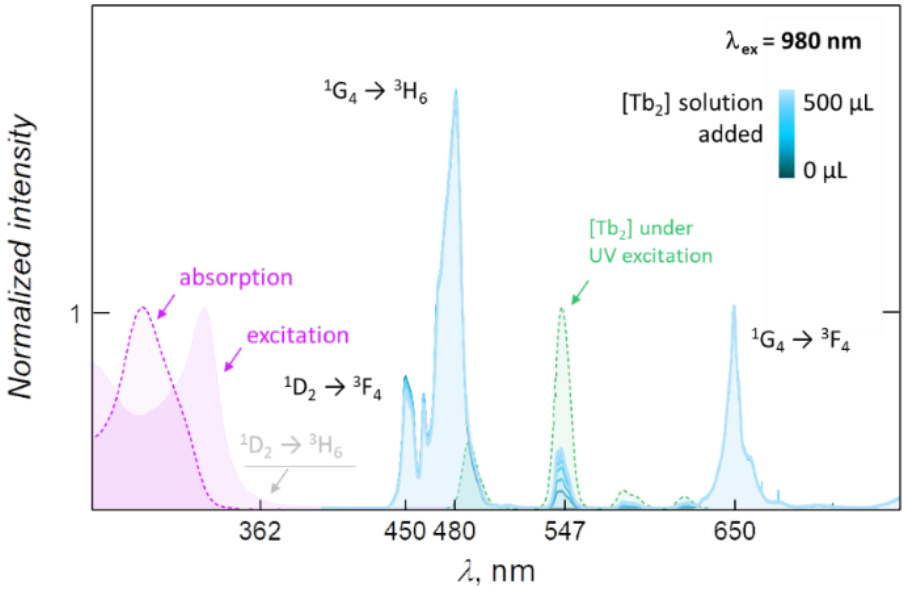

Figure 41. Study of the energy transfer from UCNPs to [Tb_2] in a chloroform mixture of the moieties through analysis of absorption spectra, excitation spectra (centred around 547 nm), and NIR-triggered upconversion emission spectra. The concentrations of UCNPs and the added [Tb_2] were 1 mg·mL^{-1} [Tb_2] and 16 mg·L^{-1}, respectively.

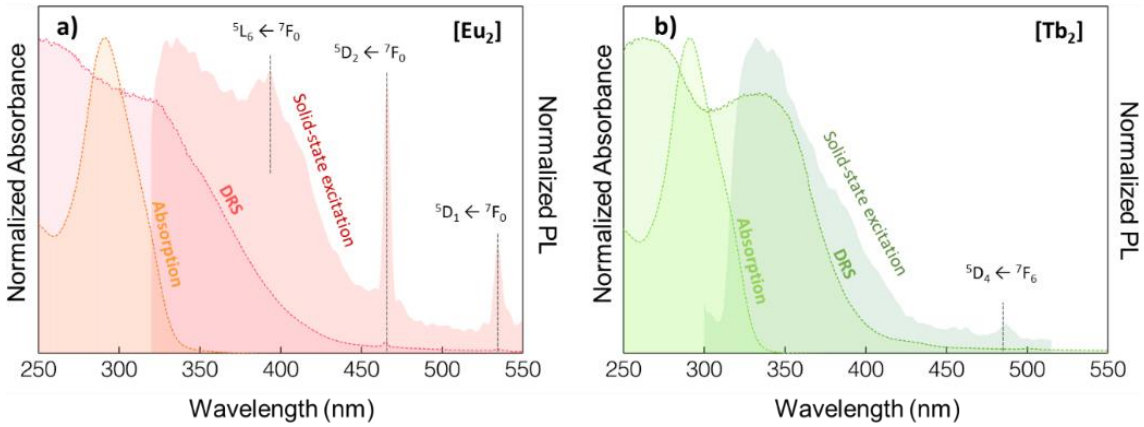

Figure 42. Comparison between absorption (solution), diffuse reflectance (DRS), and excitation spectra (solid-state) of a) [Eu_2] and b) [Tb_2]. The different profile featured by DRS and excitation spectra (recorded monitoring the emission at 612 nm and 547 nm for [Eu_2] and [Tb_2], respectively) arises from the different efficiency of the ET mechanisms that lead to the population of the ligands and the emitting level of the respective Ln^{3+} ion.

In the context of ET, non-radiative processes are more strongly influenced by the distance between the energy donor and energy acceptor than radiative ones, due to their dipole-dipole interaction nature.[133] Generally speaking, non-radiative energy transfer is unambiguously distinguished from

radiative processes since it induces a shortening of the lifetime of the donor energy level involved in the ET.[11,134] Nonetheless, it has to be mentioned that in the case of the investigated UCNPs, the steady-state emission spectrum quenching is considerably more pronounced than the observed lifetime shortening, which differs from other reports in the literature.[32,135] Also, the rich energy level scheme of Ln^{3+} ions results in innumerable activation and de-activation processes. Moreover, there is a difference between Ln^{3+} ions in the core and on the surface of the NPs in terms of accessibility for ET and relaxation pathways. As such, it is difficult to predict the effect of the ET on the kinetics of the relaxation processes in UCNPs.[32,135] For the case under study, a non-radiative ET could only occur from the Tm^{3+}: $^1D_2$ energy level since, as opposed to $^1G_4$, this is the only one that simultaneously shows (i) energy resonance with the ligands' energy levels and (ii) spectral overlap of the emission stemming from it and the optical absorption of [Ln_2] complexes, measured with diffuse reflectance spectroscopy (DRS). To elucidate the nature of the ET in the hybrid systems, lifetime measurements were performed exciting the film with 980-nm irradiation and monitoring the $^1D_2 \rightarrow {}^3F_4$ and $^1G_4 \rightarrow {}^3H_6$ emission lines of Tm^{3+} (Figure 43).

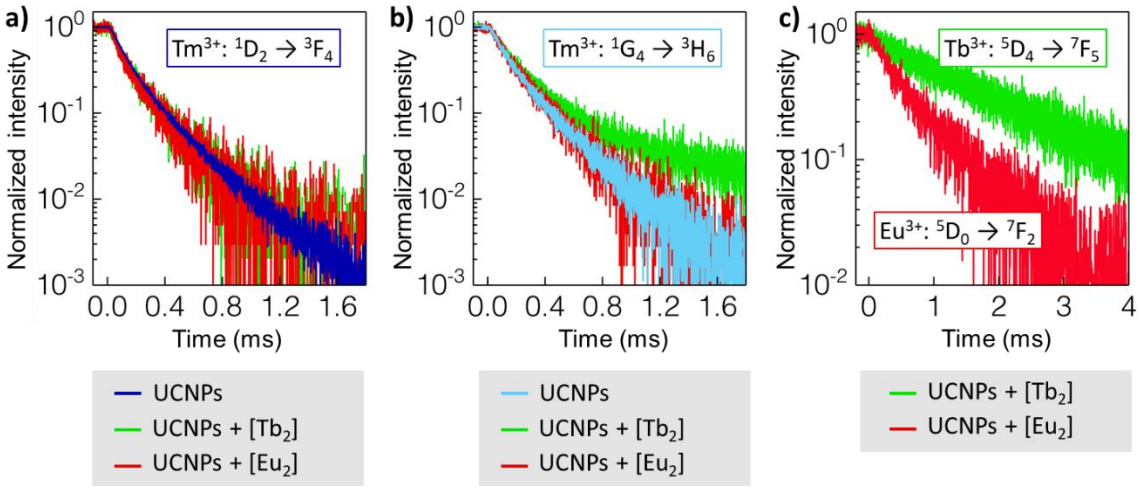

Figure 43. Decay curves obtained under 980 nm excitation of the UCNPs alone and the two hybrid systems monitoring a) Tm^{3+} $^1D_2 \rightarrow {}^3F_4$ (450 nm) and b) $^1G_4 \rightarrow {}^3H_6$ (650 nm) transitions and c) the emission of the indirectly excited complexes (547 nm for Tb^{3+}, 612 nm for Eu^{3+}).

Table 5. Effective lifetime values extracted from the decay curves recorded exciting at 980 nm the UCNPs + [Ln_2] hybrid system films

	Tm^{3+}: $^1D_2 \rightarrow {}^3F_4$	Tm^{3+}: $^1G_4 \rightarrow {}^3H_6$	Tb^{3+}: $^5D_4 \rightarrow {}^7F_5$	Eu^{3+}: $^5D_0 \rightarrow {}^7F_2$
	τ, ms	τ, ms	τ, ms	τ, ms
UCNPs	0.165 ± 0.020	0.226 ± 0.020	-	-
UCNPs + [Tb_2]	0.160 ± 0.018	-[a]	1.730 ± 0.010	-
UCNPs + [Eu_2]	0.161 ± 0.010	0.217 ± 0.021	-	0.560 ± 0.040

[a] The appearance of a second, long-lived decay component for the $^1G_4 \rightarrow {}^3H_6$ transition in the presence of [Tb_2] was a consequence of the partial overlap between Tb^{3+}: $^5D_4 \rightarrow {}^7F_5$ and Tm^{3+}: $^1G_4 \rightarrow {}^3H_6$ emission bands and is congruent with the longer lifetime observed for Tb^{3+}: $^5D_4$ level (Figure 43c and Table 5). Therefore, no lifetime is reported for this decay curve since it does not provide meaningful information to interpret the ET mechanism.

The lifetime of both $^1D_2$ and $^1G_4$ levels did not show any appreciable shortening upon amalgamation with the complexes, indicating that the quenching of the emission occurs mainly due to radiative ET processes (Table 5). Overall, these results from steady-state (solid-state and in solution), power-depend and time-resolved spectroscopy suggest three main characteristics of the investigated ET occurring under 980 nm light excitation from UCNPs to [Tb_2] or [Eu_2]. First, the ET from UCNPs to the complexes leads to the NIR-sensitized emission of the [Ln_2], which is otherwise not achievable by directly exciting them with 980-nm irradiation. Second, the appearance of this NIR-sensitized emission of [Tb_2] and [Eu_2] in the hybrid system is accompanied by quenching of Tm^{3+} emission bands that depend on their overlap with the excitation spectra of the complexes. Last, the ET proceeds most likely through re-absorption of the upconverted light from [Ln_2] predominantly via the organic ligand scaffold. Although the proximity of the moieties (favored by the small UCNP size) theoretically supports a non-radiative energy transfer process via dipole-dipole interaction, the lack of significant lifetime shortening suggests that this type of contribution – albeit not being unquestionably excluded – is largely outweighed by radiative processes.

5.3 Spatial distribution of the spectral features-hyperspectral imaging

Given its foreseeable applications as light-harvesting devices, it is pivotal that the developed hybrid system responds equally throughout the whole film. This homogeneous optical response is achieved in case of a simultaneous and continuous presence of the two moieties composing the hybrid system. In order to probe this, films obtained from UCNPs amalgamated with [Tb_2] and [Eu_2] were spectrally investigated employing hyperspectral imaging technique described in chapter 1 (Figure 44). The micrographs under white and UV light recorded on the films obtained from a 40 $mg \cdot mL^{-1}$ mixture of UCNPs and [Ln_2] display films of complexes over an extended surface (here approximately 100 x 100 μm^2). Hyperspectral mapping was performed over a selected region of interest (ROI) considering three distinct spectral ranges, where two transitions of Tm^{3+} ($^1G_4 \rightarrow {}^3F_4$ and $^1G_4 \rightarrow {}^3H_6$) and the emission from the complex (either Tb^{3+}: $^5D_4 \rightarrow {}^7F_5$ or Eu^{3+}: $^5D_0 \rightarrow {}^7F_2$) are centered. Notably, the features of the film that can be observed under UV illumination in the ROI (Figure 44a) are also distinguished under NIR excitation (Figure 44b) with an excellent overlap between the spatial distribution of the UCNP emission and the indirectly NIR-triggered emission of the complexes. To quantitatively confirm this visual evidence, PL obtained under NIR excitation were extracted from the hyperspectral maps at four different spots (Figure 44c).

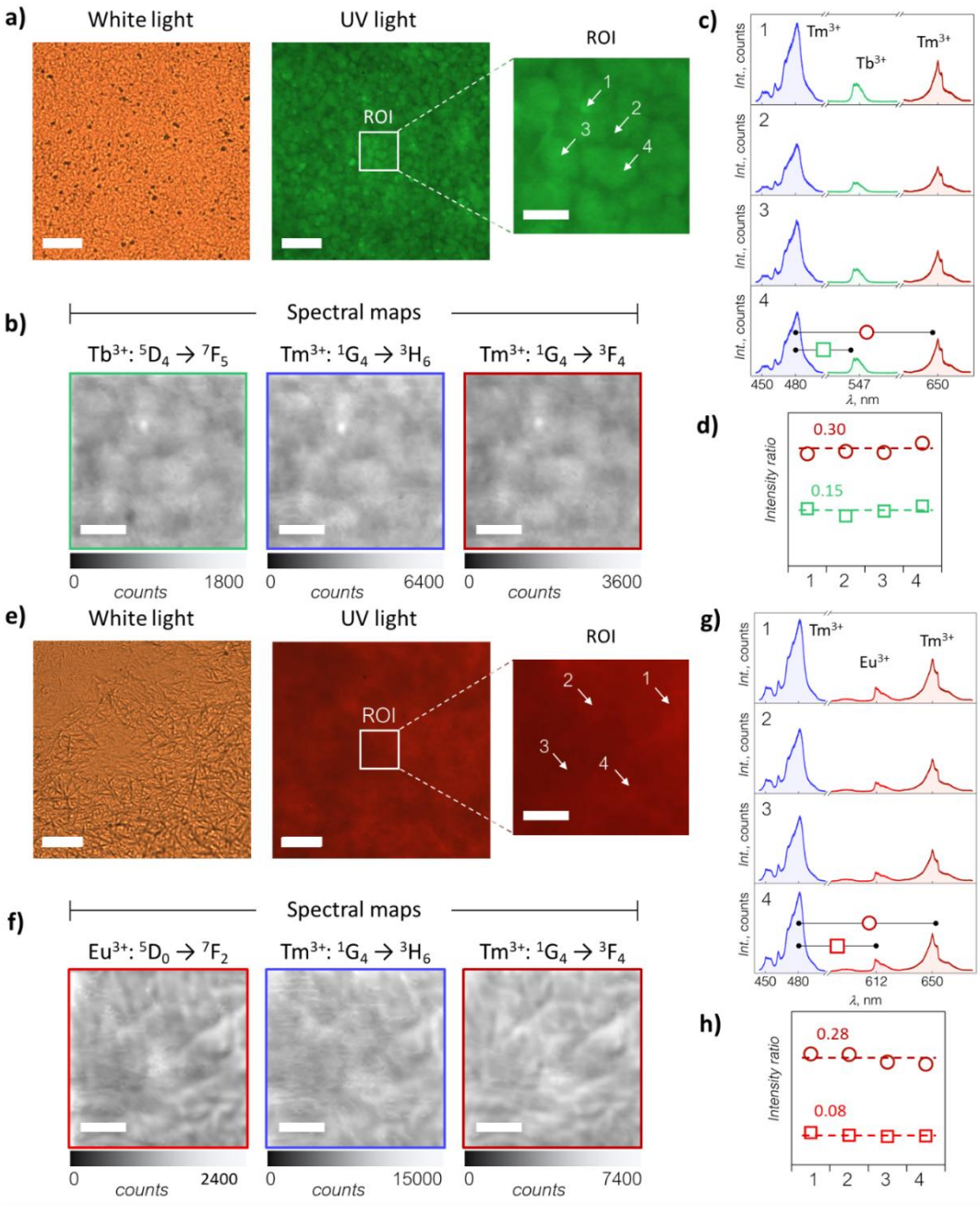

Figure 44. Micrographs for the hybrid systems obtained from a 40 mg·mL^{-1} [Ln_2] solution under white and UV light illumination along with the region of interest (ROI) (a) – [Tb_2], e) – [Eu_2]) over which spectral maps under NIR irradiation in b) and f) were obtained. The Tm^{3+} and NIR-triggered Tb^{3+} or Eu^{3+} visible emissions were monitored over an area of approximately 20 x 20 μm^2. Absolute intensities of the PL from UCNPs+[Tb_2]- and UCNPs+[Eu_2]-based hybrid system are given in c) and g). d) and h) Ratio between the integrated PL of the [Tb_2] and [Eu_2] complex *versus* Tm^{3+}: $^1G_4 \rightarrow {}^3H_6$ transition (squares) and Tm^{3+}:$^1G_4 \rightarrow {}^3F_4$ *vs* Tm^{3+}:$^1G_4 \rightarrow {}^3H_6$ (circles). Scale bars are 20 μm in the micrographs and 5 μm in ROIs and spectral maps. Micrographs are presented in real colors.

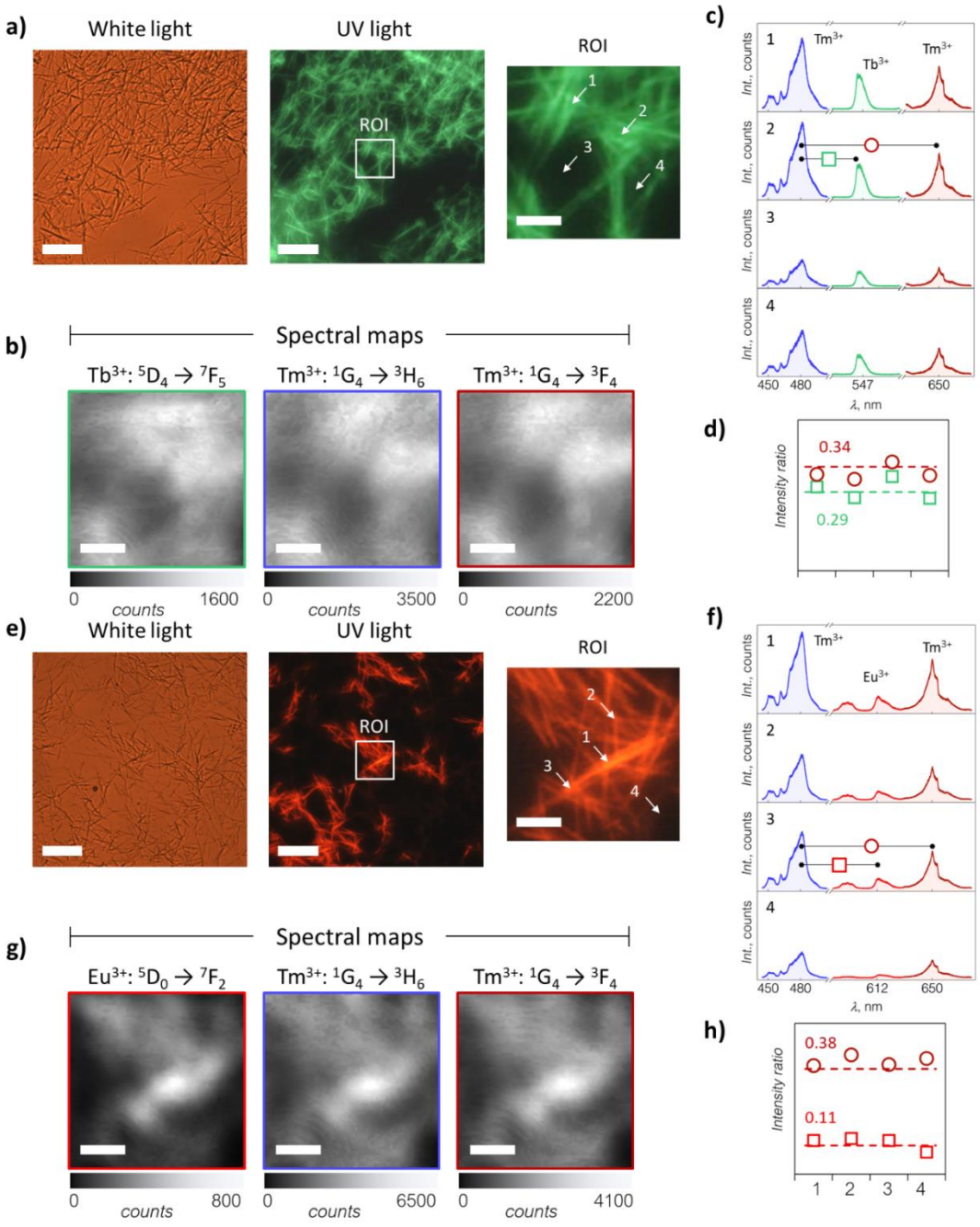

Figure 45. Micrographs for the hybrid systems obtained from a 5 mg·mL^{-1} [Ln_2] solution under white and UV light illumination along with the region of interest (ROI) (a) – [Tb_2], e) – [Eu_2]) over which spectral maps under 980 nm light irradiation in b) and f) were obtained. The Tm^{3+} and NIR-triggered Tb^{3+} or Eu^{3+} visible emissions were monitored over an area of approximately 20 x 20 μm^2. Absolute intensities of the PL from UCNPs+[Tb_2]- and UCNPs+[Eu_2]-based hybrid system are given in c) and g). d) and h) Ratio between the integrated PL of the [Tb_2] and [Eu_2] complex *versus* Tm^{3+}: $^1G_4 \rightarrow {}^3H_6$ transition (squares) and Tm^{3+}:$^1G_4 \rightarrow {}^3F_4$ *vs* Tm^{3+}:$^1G_4 \rightarrow {}^3H_6$ (circles). Scale bars are 20 μm in the micrographs and 5 μm in ROIs and spectral maps. Micrographs are presented in real colors.

Although some fluctuations in the absolute intensity of the signals were noticeable, the ratio between the integrated intensity of the three signals did not exhibit significant fluctuations throughout the film surface (Figure 44d). Hyperspectral imaging performed over three distinct ROIs on a second hybrid film – prepared under identical conditions – evidences the reliability of the optical properties over larger sample areas and from film-to-film (Figure S7). Similar behavior is also shown by the hybrid system obtained at a concentration of 5 $mg \cdot mL^{-1}$ (Figure 45). This experimental evidence – in hand with SEM and TEM observations (Figure 37) – suggests that, upon [Tb_2] and [Eu_2] crystallization, the UCNPs organize close to the complexes, hence fostering the ET process upon NIR excitation.

5.4 Chapter conclusion

In this chapter, hybrid systems composed of a film amalgamating lanthanide complexes [Tb_2] or [Eu_2] with α-$NaGdF_4$:Yb^{3+}(20%),Tm^{3+}(0.5%) NPs were presented. The hybrid system was prepared via a straightforward drop-cast approach, exploiting the interaction between the complex and nanoparticular moieties. The choice of $NaGdF_4$:Yb^{3+},Tm^{3+} as the UCNP material ensured a good spectral overlap of the NIR-triggered upconverted visible emission with the excitation spectra of the lanthanide complexes. The proximity of the two species, along with the mentioned spectral overlap, promoted effective energy transfer from the UCNPs to the lanthanide complexes, while retaining their strong emission under UV illumination, due to the energy transfer. Thus, the complexes were indirectly excitable using NIR light, resulting in augmented light-harvesting capability. The combination of power-dependent and time-resolved spectroscopic studies revealed the predominantly radiative, ligand-mediated nature of the energy transfer, setting the ground for further understanding of these amalgamated systems. Finally, the use of hyperspectral imaging

enabled to assess the concomitant presence of UCNPs and lanthanide complexes and the occurrence of the energy transfer mechanism between them throughout the hybrid system.

Therefore, albeit only preliminary optimization with respect to concentration, ratio, and nature of the moieties was carried out, the results demonstrate that the preparation of multiwavelength-responsive hybrid systems composed of UCNPs and [Ln_2] can be promptly achieved. It is accomplished by taking advantage of the hydrophobic interaction between both moieties, which prompts their assembly in structures with augmented optical properties. These results open opportunities for the preparation of similar systems based on UCNPs and lanthanide complexes yet leaving space for a case-by-case optimization in terms of amalgamated moieties and film morphology.

6 Surface modification of $NaLnF_4$-based upconverting nanoparticles

6.1 A requirement for biomedical applications

The NPs presented in this thesis, irrespective of their crystalline phase or the microwave conditions used for their synthesis, are dispersible in organic solvents. This is due to their surface capping with oleate groups (OA^- represent $CH_3(CH_2)_7C=C(CH_2)_7COO^-$), a hydrophobic molecule. Such hydrophobic character is not suitable for biomedical applications, as they mostly occur under aqueous conditions.[136] The surface of the ligand-free $NaLnF_4$ NPs is positively charged, and such NPs can disperse in aqueous solution. However, these ligand-free NPs can easily agglomerate and form larger clusters. This can be problematic for the formation of the hybrid system seen in chapter 5, but also if the NPs are inserted in a biological setting (like during cell uptakes studies). As such, seeking biomedical applications, simply removing the oleate ligand is not a viable strategy for surface modification. Moreover, surface ligands can be used for bioconjugation with a gamut of substance relevant to biomedical applications, such as aptamer, proteins and even antibodies.[137–139] In regard to the small NPs synthesized and analyzed in chapter 4 and 5, they were subjected to surface modifications so that they could be dispersed in aqueous solvents. These types of modifications selected were: a hard inorganic silica-based shell, a soft molecular shell with polyacrylic acid (PAA) or α-NH_2-ω-COOH-PEG (Figure 47). This work should hopefully provide a basis for future bioconjugation studies and biomedical applications of UCNPs.

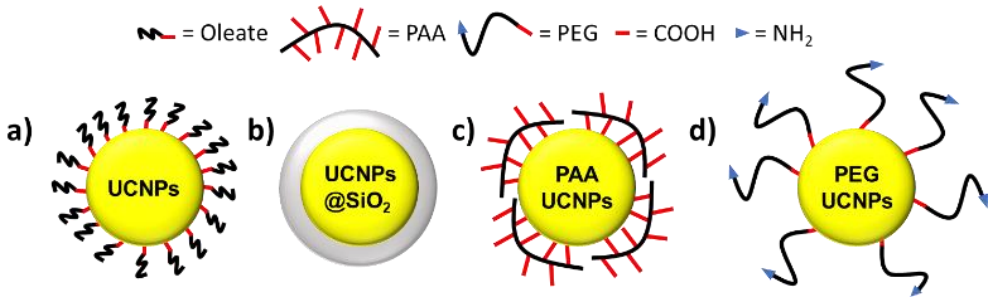

Figure 46. Scheme of different NP surface modifications. a) OA^--capped UCNPs, b) silica-coated UCNPs c) PAA-capped UCNPs, and d) PEG-capped UCNPs.

6.2 Surface modification

6.2.1 Silanization

Silica NPs have been recognized for their potential application in nanomedicine due to their biocompatibility and their drug-carrier capacity.[140] In turn, the addition of a silica shell has become a strategy to safely disperse other types of NPs, *e.g.*, quantum dots, in aqueous media.[141] Silica-coated UCNPs ($NaGdF_4$-based or not) have been widely investigated for imaging and cancer treatment, since the surface functional groups (-COOH, $-NH_2$,-OH and-SH) can conjugate with biomolecules, like aptamers.[142,143] Here, the silanization procedure was carried out with α-$NaGdF_4$:Yb^{3+}(20%),Tm^{3+}(0.5%) NPs made from [$Ln(TFA)_3$] precursors. The core NPs were synthesized using the same procedure as described in chapter 5. They had an average size of 10 ± 1 nm (Figure 47a and Figure 47c). The silanization was obtained using TEOS, a commonly used source of silicon. TEM images confirmed the presence of the inorganic SiO_2 shell, with a thickness of roughly 3.6 nm (Figure 47b-c). Photoluminescence measurements showed that the NPs were weakly emitting when being dispersed in water (Figure 47d). This low PL can be attributed to a certain extent to the presence of water molecules. They can partially absorb the NIR excitation light, which in turn reduces the incident excitation energy that reaches the UCNPs.[65] Furthermore, the molecular vibration of O-H groups can interact with the excited Ln^{3+} ions, leading to a non-

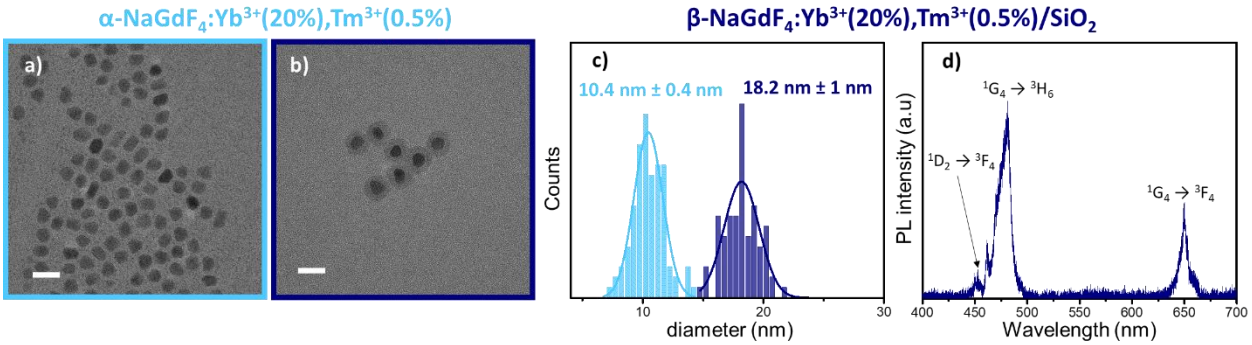

Figure 47. TEM images of a) α-$NaGdF_4$:Yb^{3+},Tm^{3+} and b) α-$NaGdF_4$:Yb^{3+}, Tm^{3+}/SiO_2 NPs. c) Size distribution of the core and core/shell NPs. The SiO_2 layer has a thickness of ca. 3.6 nm. D) Upconversion spectrum of the silica-coated UCNPs dispersed in water with a concentration of 43 mg·mL^{-1} under 980-nm excitation (P = 160 mW). Scale bars are 20 nm.

radiative deactivation and quenching of the photoluminescence.[144] The O-H functional groups are also present in this inorganic silica shell itself, *i.e.* under the form of Si-O-H groups. The quenching of the upconverted PL is more pronounced if the shell is porous.[144] The porosity of inorganic silica shell is usually removed by annealing the NPs at high temperature (600°C), but in turn, the NP's dispersion capability are lost.[145]

6.2.2 Ligand exchange with PAA

The OA^- groups are anchored at the surface of the $NaGdF_4$-based NPs thanks to its carboxy (the COO^-) head through electrostatic interaction. As such, it is possible to replace it with another hydrophilic ligand, as long as it has a negatively charged moiety. PAA is a long carbon-based polymer that contains many COOH groups, which allows it to form a soft molecular shell around the UCNPs. Exchanging the oleate ligand for PAA is a rather simple procedure, as it just requires to mix the UCNPs and the PAA in a chloroform/ethanol solution overnight.[105] The ligand exchange was performed on α-$NaGdF_4$:Yb^{3+}, Tm^{3+} NPs made from [$Ln(TFA)_3$], similar to those used for the silanization. FTIR results did not confirm the presence of PAA on the UCNPs surface (Figure 48a). The UCNPs' FTIR spectrum lacks the characteristic 1730 cm^{-1} band from the COO^- group of the PAA.[146] However, the FTIR spectrum neither displayed the 1440 cm^{-1} nor the 1560 cm^{-1} bands of

the OA^- ligands, indicating removal of the initially on the NP surface present oleate groups.[106,146] PL measurements in aqueous solution confirmed that the NPs were still emissive (Figure 49b). This suggests that the NPs became water-dispersible, providing indirect evidence of a successful ligand exchange. Nonetheless, the PL was rather weak, which implied that these NPs suffer from the same problems as the silica-coated UCNPs, *i.e.* quenching induced by the O-H vibrations. A TEM image of PAA-NPs is shown in Figure 48c, which offers more evidence of the successful ligand exchange. The UCNPs remains well separated. The partial agglomeration observed in Figure 48c could be due to the sample preparation of the hydrophilic UCNPs on a hydrophobic carbon-coated TEM grid.

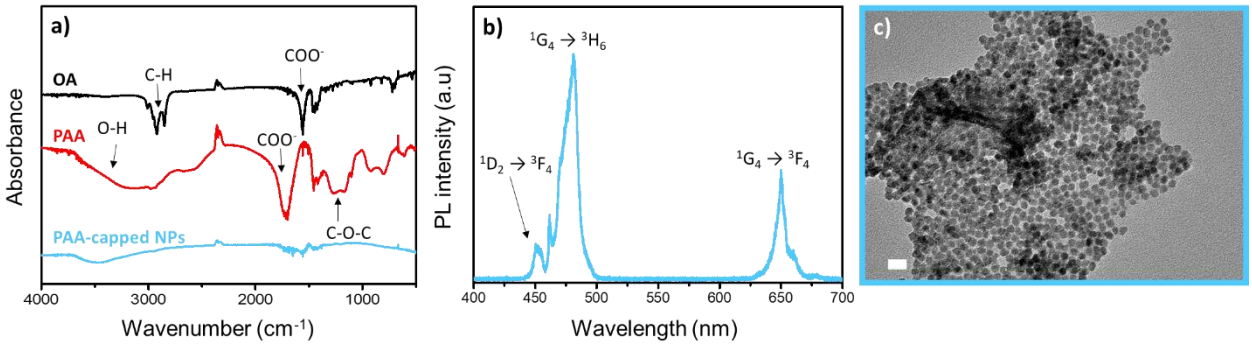

Figure 48. a) FTIR spectrum of the PAA-capped α-$NaGdF_4$:Yb^{3+},Tm^{3+} NPs in comparison with PAA and NaOA alone. b) Associated upconverted PL spectrum of the UCNPs dispersed in water under 980-nm excitation (P = 160 mW, NP concentration = 27 mg·mL^{-1}). c) TEM images of the PAA-capped UCNPs. Scale bar is 50 nm.

6.2.3 Ligand exchange with α-NH_2- ω-COOH-PEG

Polyethylene glycol (PEG) is a versatile ligand that is used often conjugated with therapeutic compounds to prevent agglomeration and to improve the solubility (or in our case, the NP dispersion capability).[147] The terminal COOH moiety of the PEG ligand is used as an electrostatic anchor to bind to the NP surface and displace the oleate ligand, a mechanism similar to what has been tried with the PAA. The PEG exchange was carried out on the α-$NaGdF_4$:Yb^{3+},Tm^{3+} NPs derived from [$Ln(TFA)_3$], similar to those used for the silanization. Here, FTIR analysis confirmed

the successful surface modification on the PEG-capped UCNPs with the presence of the absorbance band ca. 1080 cm^{-1} (C-N group), from the PEG, and the absence of the 1440 and 1560 cm^{-1} bands, characteristic of the OA^- ligand (Figure 50a).[106,146] PL measurements performed on the NPs' aqueous dispersion also confirmed that the NPs became water-dispersible (Figure 50b). Importantly, the terminal amine moiety can further be used for bioconjugation as a binding site.[148] Nonetheless, the PL behavior of PEG-capped UCNPs suffered from the same issue as the other water-dispersible NPs, *i.e.*, quenching by the O-H stretches.

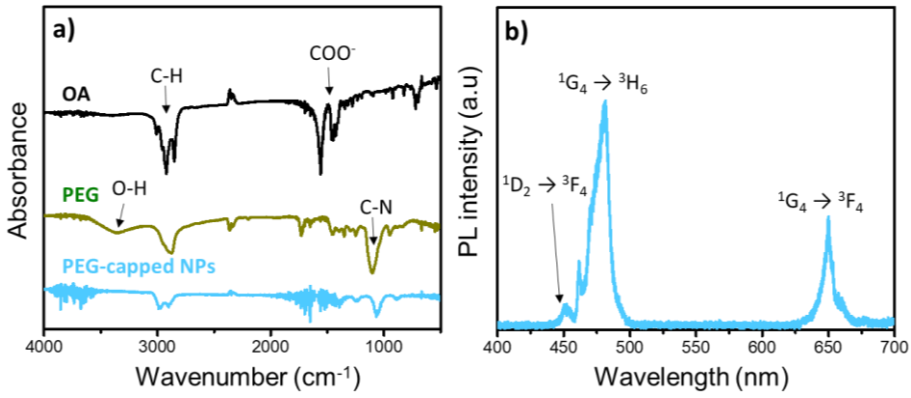

Figure 49. a) FTIR spectra of the PEG-capped α-$NaGdF_4$:Yb^{3+},Tm^{3+} NPs in comparison with PEG and NaOA. b) Associated upconversion spectrum of the PEG-capped UCNPs dispersed in water under 980 nm excitation (P = 160 mW, NP concentration = 33 $mg \cdot mL^{-1}$).

6.3 Chapter conclusion

Hard and soft surface modifications were successfully performed on the UCNPs as demonstrated by TEM, FTIR and PL analysis. However, the PL in aqueous solution remained weak. The low PL was attributed to quenching by O-H stretches. In the case of silica-coated UCNPs, the Si-O-H groups, in combination with a porosity that allows water molecules to reach the NPs caused a decrease of the PL. Likewise, PAA- and PEG-capped UCNPs were also affected by the O-H stretches-induced quenching. The PL issue can be addressed by applying such surface

modifications on the bright core/shell UCNPs described in chapter 4, since the luminescent ions are more protected from solvent and SiO_2 shell-assisted quenching than in the core-only NPs.

7 Conclusion

The phase-selective microwave-assisted synthesis of $NaLnF_4$ NPs was achieved using $[Ln(TFA)_3]$ as precursors and a set of two temperatures, T_1 (1 s) and T_2 (10 min). By decreasing the Ln^{3+} concentration to 0.0625 $mol \cdot L^{-1}$ and increasing the Na^+-to-Ln^{3+} ion ratio to 3:1, sub-10 nm β-$NaGdF_4$:Yb^{3+}(20%),Er^{3+}(2%) NPs were obtained. This constitutes, to the best of my knowledge, the first example of hexagonal-phase UCNPs synthesized *via* the microwave-assisted decomposition of $[Ln(TFA)_3]$. Changing the precursor for $[Ln(OA)_3]$ and $[Ln(Ac)_3]$ resulted in ultrasmall (sub-5 nm) β-$NaGdF_4$:Yb^{3+},Er^{3+} NPs. $[Ln(TFA)_3]$-derived NPs (of both phases) exhibited high pressure profile, which correlates with their larger dimensions and lower decomposition temperature. Despite being smaller, $[Ln(OA)_3]$-derived NPs emitted better in the NIR range than the $[Ln(TFA)_3]$-derived NPs, which had brighter PL in the visible range. Time and temperature studies show that the $[Ln(OA)_3]$- and $[Ln(Ac)_3]$-derived NPs undergo an α → β phase transformation, which was found to be a thermodynamically controlled process. This phase transformation was not observed with the $[Ln(TFA)_3]$-derived NPs, which directly crystallized in the aimed phase. Furthermore, the phase transformation was found to be accelerated under microwave conditions, since no pure cubic-phase NPs could be isolate during the ramping stage. Shell growth using $[Ln(TFA)_3]$ as a precursor was successful on all the sub-10 and sub-5nm NPs, which retained the core crystalline phase. The addition of the shell resulted in higher PL and longer lifetime, while keeping the NP size close to or below 10 nm.

Seeking the development of optical devices, $NaGdF_4$:Yb^{3+}(20%),Tm^{3+}(0.5%) NPs were combined with UV-excitable Ln-based complexes. Under NIR excitation, the resulting hybrid system showed energy transfer from the UCNPs to the Ln-based complexes. The ET process was demonstrated to occur from the re-absorption of the $^1D_2 \rightarrow {}^3F_4$ emission from the Tm^{3+} via the $tfaa^-$

and bmp ligands rather than being directly absorbed by the Tb^{3+} or Eu^{3+}. As a consequence, quenching of the Tm^{3+} emission along with sensitization of the [Ln_2] emission was observed. Time-resolved spectroscopy provided further evidence that the ET was not FRET-based but due to re-absorption. Hyperspectral imaging was used for additional analysis of the optical properties of the hybrid films, demonstrating good optical homogeneity across the samples.

Last but not least, surface modifications were performed on $NaGdF_4$:Yb^{3+}(20%),Tm^{3+}(0.5%) NPs to replace the hydrophobic OA^- ligands by a hydrophilic surface. A hard, silica-based shell was successfully grown, while ligand exchange allowed for the formation of a soft molecular shell with either PAA and α-NH_2-ω-COOH-PEG. No matter the strategy employed, the NPs became water-dispersible, albeit their PL was affected by O-H induced quenching.

Overall, with microwave-assisted synthesis protocols for UCNPs (especially core/shell) now being established and having demonstrated the capacity of hyperspectral imaging to observe and partially analyze ET process, many research possibilities are appearing. In the strictly material field, the next steps would be to implement UCNPs in light-harvesting and optoelectronic devices, like solar cells and luminescent screens. Furthermore, with the access to water-dispersible UCNPs, it is now possible to attempt bioconjugation with various nanomaterials and molecules relevant to the biomedical field, and to endeavour bioimaging.

8 Annex

8.1 Effect of the microwave conditions on crystalline phase, size and PL behavior of UCNPs

Table S1. Relation between the microwave conditions and the crystalline phase, size and PL behavior of the $NaGdF_4$:Yb^{3+}(20%),Er^{3+}(2%) NPs

Precursors (core)	Size (nm) {core size (nm)}	Crystalline phase	Na^+-to-Ln^{3+} ion ratio	Ln^{3+} ions concentration ($mol \cdot L^{-1}$)	T_1(°C); T_2(°C)	PL intensity enhancement[a] for $^4S_{3/2} \rightarrow {}^4I_{15/2}$	PL intensity enhancement[a] for $^4F_{9/2} \rightarrow {}^4I_{15/2}$	PL intensity enhancement[a] for $^4I_{13/2} \rightarrow {}^4I_{15/2}$	PL lifetime for $^4S_{3/2} \rightarrow {}^4I_{15/2}$	PL lifetime for $^4F_{9/2} \rightarrow {}^4I_{15/2}$
$[Ln(TFA)_3]$	9.3	α	1:1	0.125	300; 230	–[b]	–[b]	–[b]	15	29
	5.5	β	3:1	0.0625	260; 250	7.5[c]	3.9[c]	1.4[c]	22	25
$[Ln(OA)_3]$	3.2	β	4:1	0.0625	260; 250	4.5[c]	2.2[c]	2.8[c]	16	18
$[Ln(Ac)_3]$	3.0	β	3:1	0.0625	260; 250	1[c]	1[c]	1[c]	17	–[d]
$[Ln(TFA)_3]$[e]	11.3 {9.3}	α	3:1	0.0625	230;230	3[f]	3[f]	1.7[f]	25	49
	11.9 {7.0}	β	3:1	0.0625	230;230	6[f]	10.4[f]	4.6[f]	156	156
$[Ln(OA)_3]$[e]	6.8 {2.5}	β	3:1	0.0625	230;230	9[f]	3.6[f]	142.7[f]	103	127
$[Ln(Ac)_3]$[e]	5.6 {2.8}	β	3:1	0.0625	230;230	3[f]	1.7[f]	72.8[f]	73	87

[a] Obtained by the dividing the integrated PL intensity by a reference sample integrated PL intensity.

[b] Not comparable with the hexagonal sample emission, as it was done on a different day and different measurement parameters.

[c] Normalized by the integrated PL intensity of $[Ln(Ac)_3]$-derived NPs.

[d] Weak band.

[e] Core/shell NPs, shells are grown using $Gd(TFA)_3$ precursor.

[f] Normalized by the integrated PL intensity of core-only NPs.

8.2 Effect of reaction time and temperature on crystalline phase, size, and photoluminescence

This figure presented here is reprinted (adapted) with permission from Ref[107] *with permission from The Royal Society of Chemistry.*

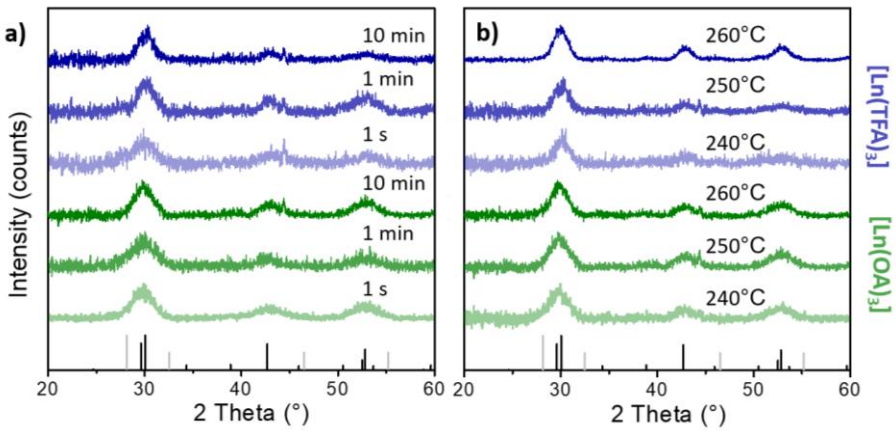

Figure S1. Effect of reaction time and temperature on the crystalline phase of NPs obtained from $[Ln(TFA)_3]$ and $[Ln(OA)_3]$. a) XRD patterns of NPs obtained after 1 s, 1 min, and 10 min, respectively (Reaction temperature: T_1 = 260 °C, T_2 = 250 °C). b) XRD patterns of NPs obtained at different reaction temperatures T_2 (Reaction time: 10 min). References: β-$NaGdF_4$ (PDF#: 01-080-8787, black lines), α-$NaGdF_4$ (PDF#: 00-027-0697, light grey lines).

Note: All the following presented in the annex are reprinted (adapted) with permission from R. Marin, I. Halimi, D. Errulat, Y. Mazouzi, G. Lucchini, A. Speghini, M. Murugesu and E. Hemmer, ACS Photonics, 2019, 6, 436–445. Copyright (2019) American Chemical Society.

8.3 Effect of the mass ratio between UCNPs and [Tb_2] on film morphology

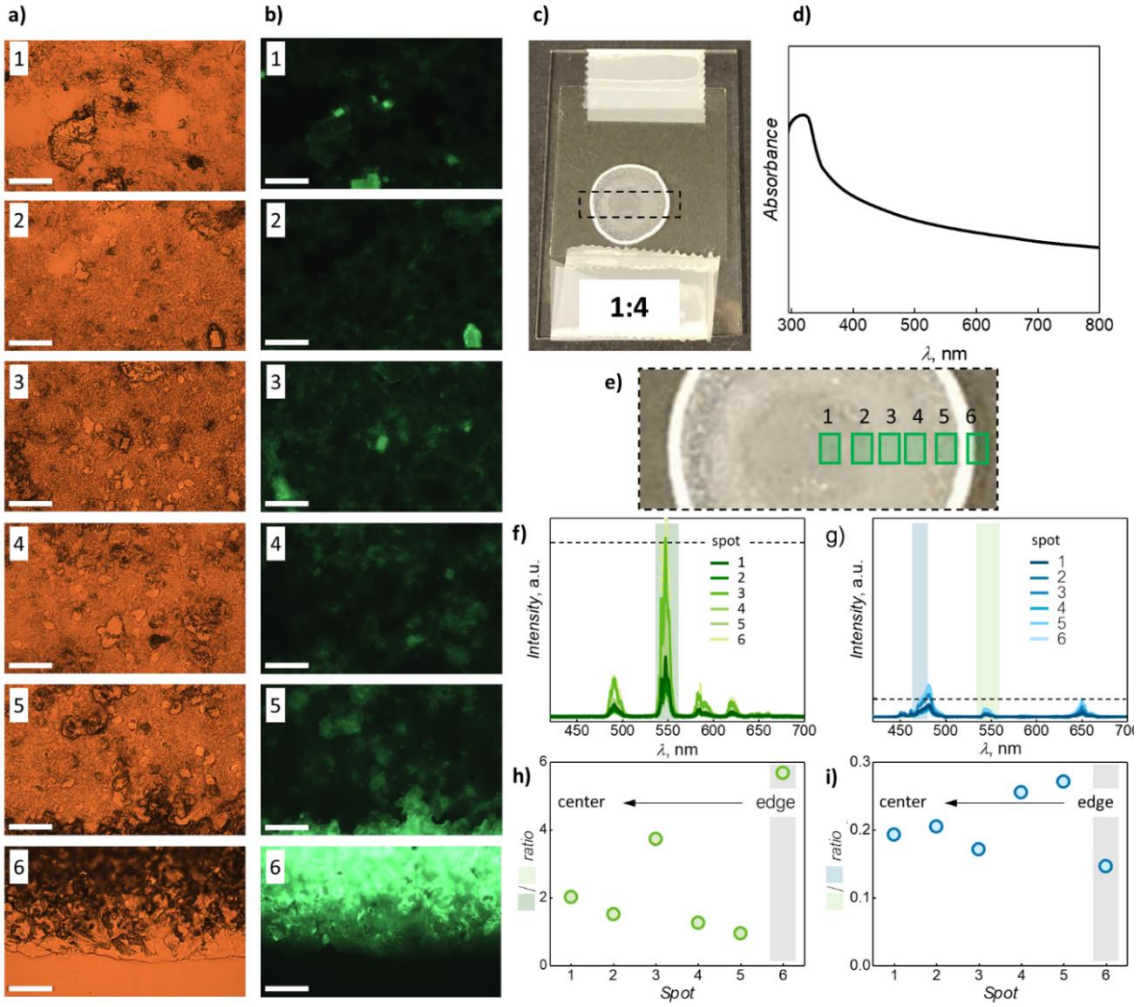

Figure S2. Hybrid system film obtained using a solution with a UCNPs-to-[Tb_2] mass ratio of 1:4 (concentration = 40 mg·mL^{-1}). a) Bright-field and b) UV-excited micrographs taken on six different spots of the film. c) Photograph of the film. d) Absorption spectrum of the film. e) Magnification of the film along with the marked spots from where the images were acquired. At each spot, spectra under f) UV and g) 980 nm excitation were recorded. The optical performance of the film was evaluated considering: h) the ratio between the emission of [Tb_2] under UV (direct) and NIR (indirect) excitation, and i) the ratio between the indirectly excited [Tb_2] emission and thulium upconverted blue emission. The spectral ranges used for the integration of the emissions are shown in f) and g) as shaded areas in dark green ([Tb_2] direct excitation), light green ([Tb_2] indirect excitation), and blue (Tm). Scale bars in a) and b) are 100 μm. Dashed lines in f) and g) are drawn in correspondence of the same absolute intensity value (7000 a.u.).

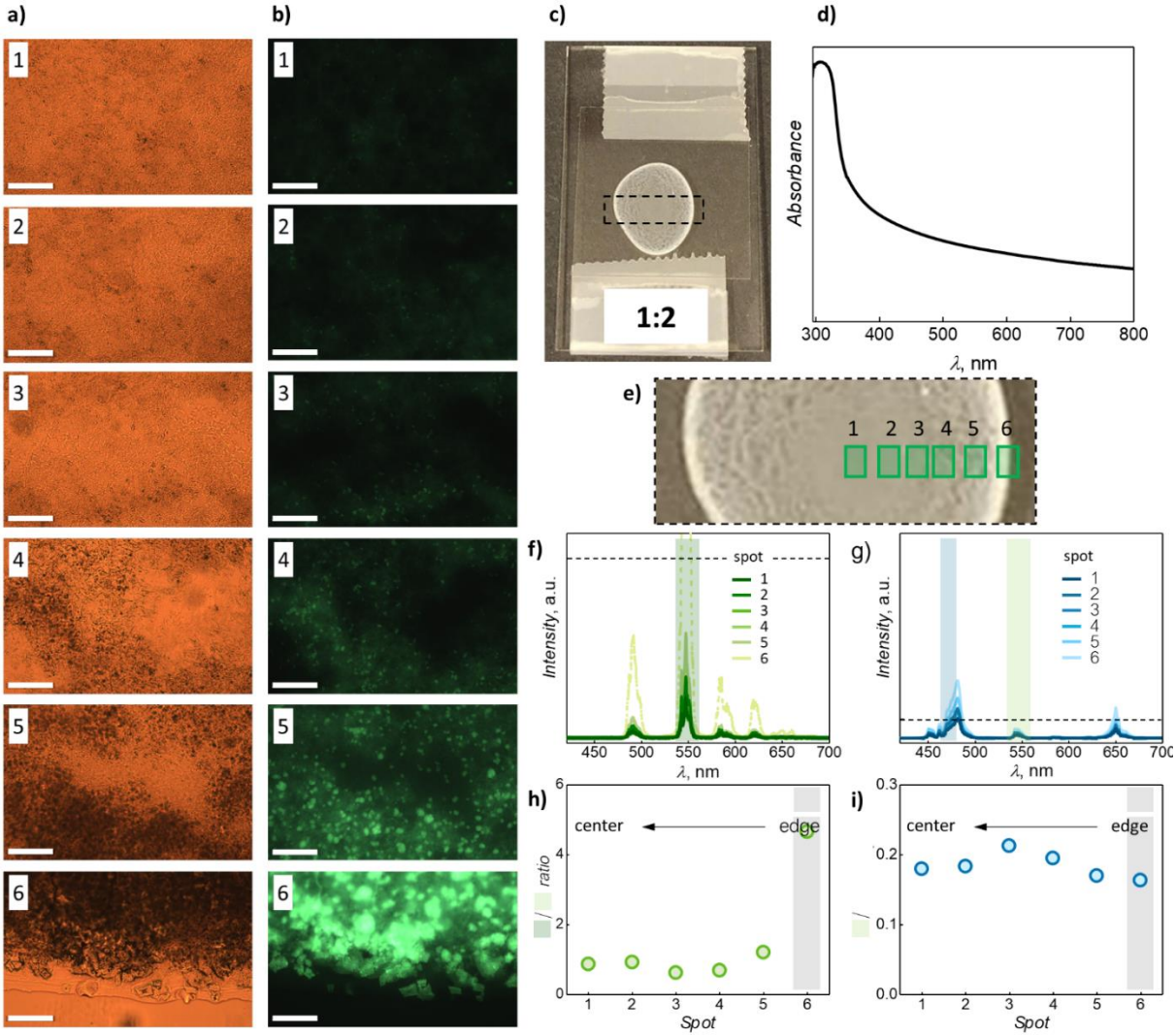

Figure S3. Hybrid system film obtained using a solution with a UCNPs-to-[Tb_2] ratio of 1:2 ([Tb_2] concentration: 40 mg·mL^{-1}). a) Bright-field and b) UV-excited micrographs taken on six different spots of the film. c) Photograph of the film. d) Absorption spectrum of the film. e) Magnification of the film along with the marked spots from where the images were acquired. At each spot, spectra under f) UV and g) 980 nm excitation were recorded. The optical performance of the film was evaluated considering: h) the ratio between the emission of [Tb_2] under UV (direct) and NIR (indirect) excitation, and i) the ratio between the indirectly excited [Tb_2] emission and thulium upconverted blue emission. The spectral ranges used for the integration of the emissions are shown in f) and g) as shaded areas in dark green ([Tb_2] direct excitation), light green ([Tb_2] indirect excitation), and blue (Tm). Scale bars in a) and b) are 100 μm. Dashed lines in f) and g) are drawn in correspondence of the same absolute intensity value (7000 a.u.).

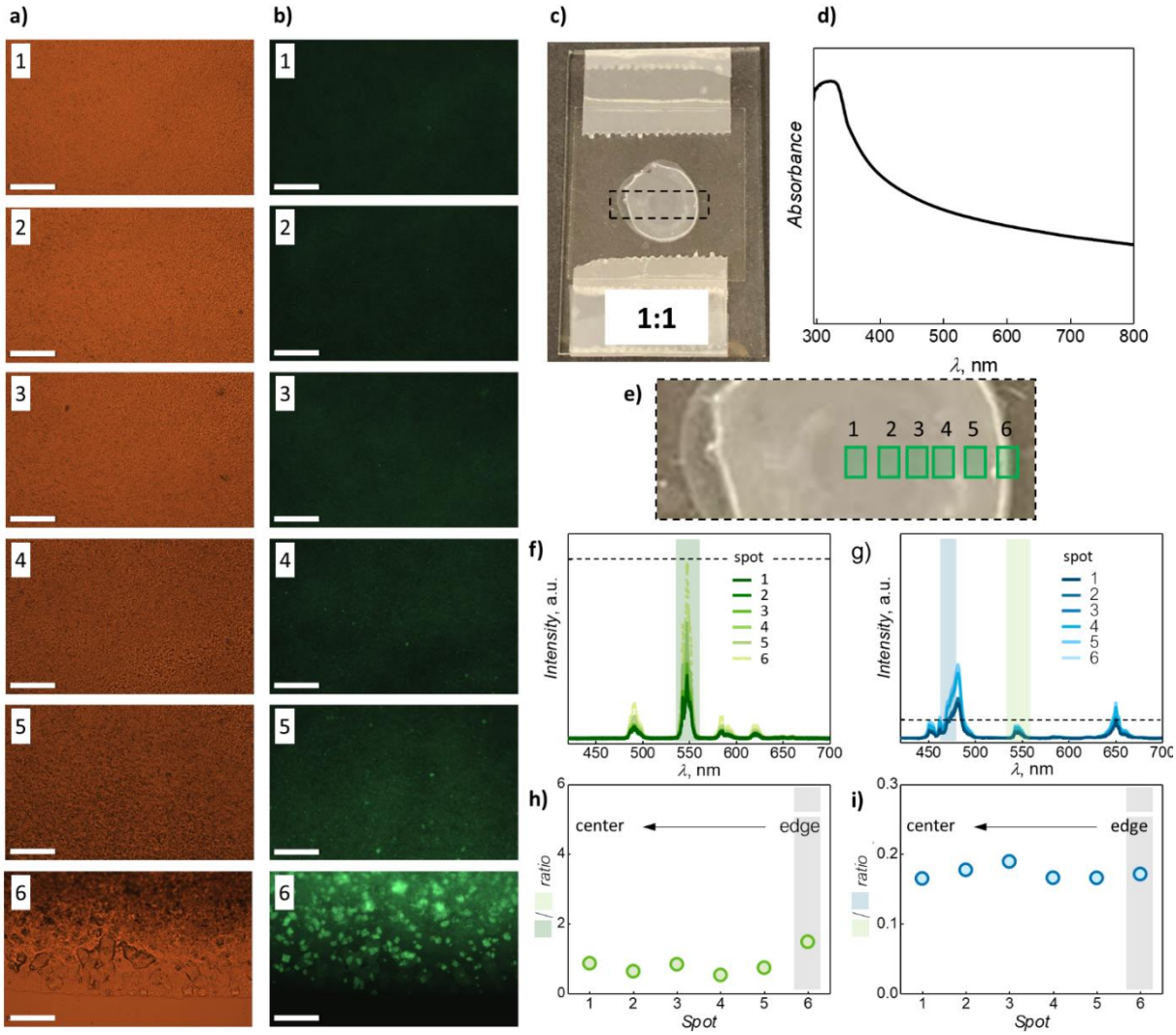

Figure S4. Hybrid system film obtained using a solution with a UCNPs-to-[Tb_2] ratio of 1:1 ([Tb_2] concentration: 40 mg·mL^{-1}). a) Bright-field and b) UV-excited micrographs taken on six different spots of the film. c) Photograph of the film. d) Absorption spectrum of the film. e) Magnification of the film along with the marked spots from where the images were acquired. At each spot, spectra under f) UV and g) NIR excitation were recorded. The optical performance of the film was evaluated considering: h) the ratio between the emission of [Tb_2] under UV (direct) and NIR (indirect) excitation, and i) the ratio between the indirectly excited [Tb_2] emission and thulium upconverted blue emission. The spectral ranges used for the integration of the emissions are shown in f) and g) as shaded areas in dark green ([Tb_2] direct excitation), light green ([Tb_2] indirect excitation), and blue (Tm). Scale bars in a) and b) are 100 μm. Dashed lines in f) and g) are drawn in correspondence of the same absolute intensity value (7000 a.u.).

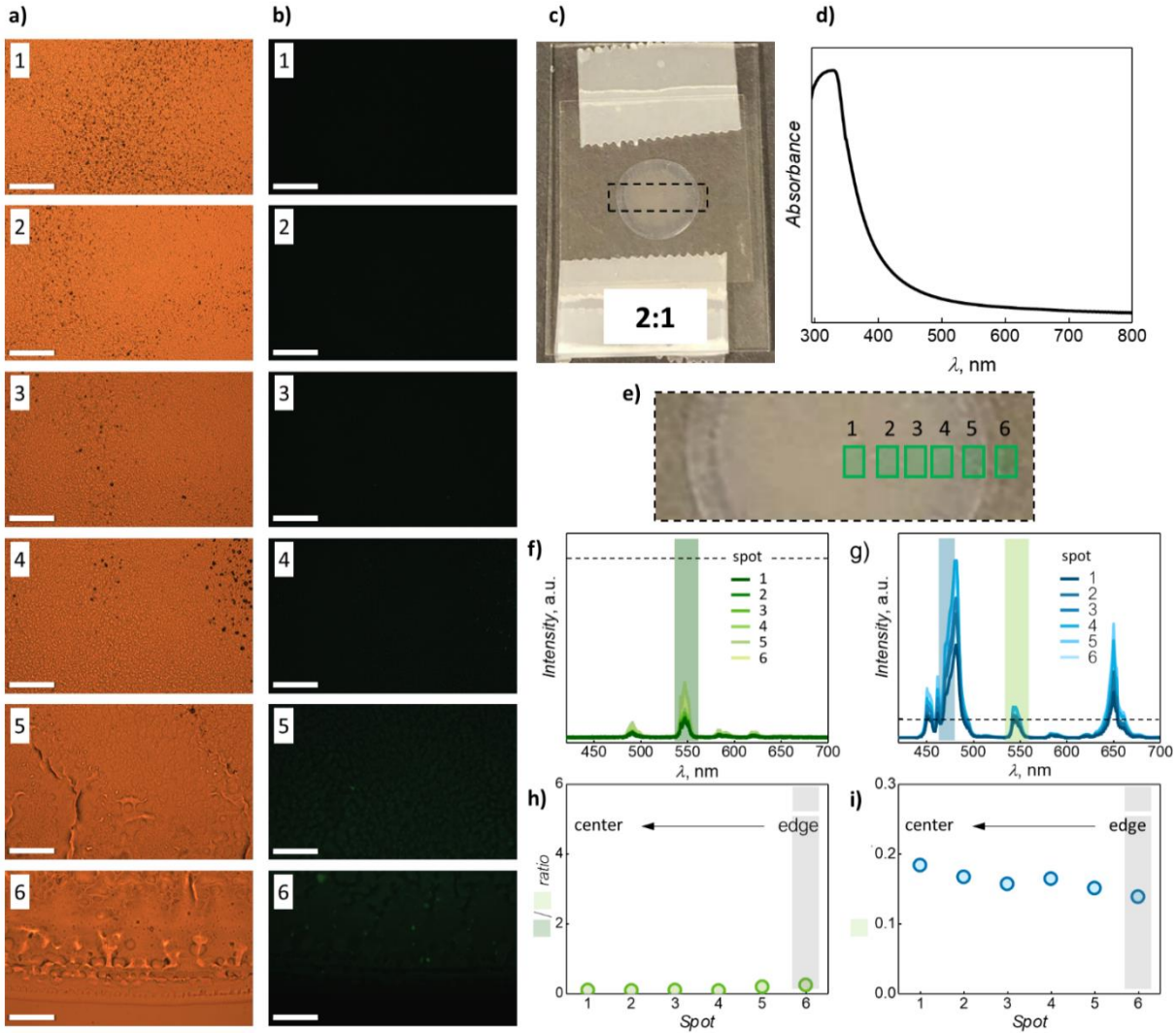

Figure S5. Hybrid system film obtained using a solution with a UCNPs-to-[Tb_2] ratio of 2:1 ([Tb_2] concentration: 40 mg·mL^{-1}). a) Bright-field and b) UV-excited micrographs taken on six different spots of the film. c) Photograph of the film. d) Absorption spectrum of the film. e) Magnification of the film along with the marked spots from where the images were acquired. At each spot, under f) UV and g) (80 nm excitation were recorded. The optical performance of the film was evaluated considering: h) the ratio between the emission of [Tb_2] under UV (direct) and NIR (indirect) excitation, and i) the ratio between the indirectly excited [Tb_2] emission and thulium upconverted blue emission. The spectral ranges used for the integration of the emissions are shown in f) and g) as shaded areas in dark green ([Tb_2] direct excitation), light green ([Tb_2] indirect excitation), and blue (Tm). Scale bars in a) and b) are 100 μm. Dashed lines in f) and g) are drawn in correspondence of the same absolute intensity value (7000 a.u.).

8.4 Effect of the UCNP and [Tb_2] concentration on film morphology

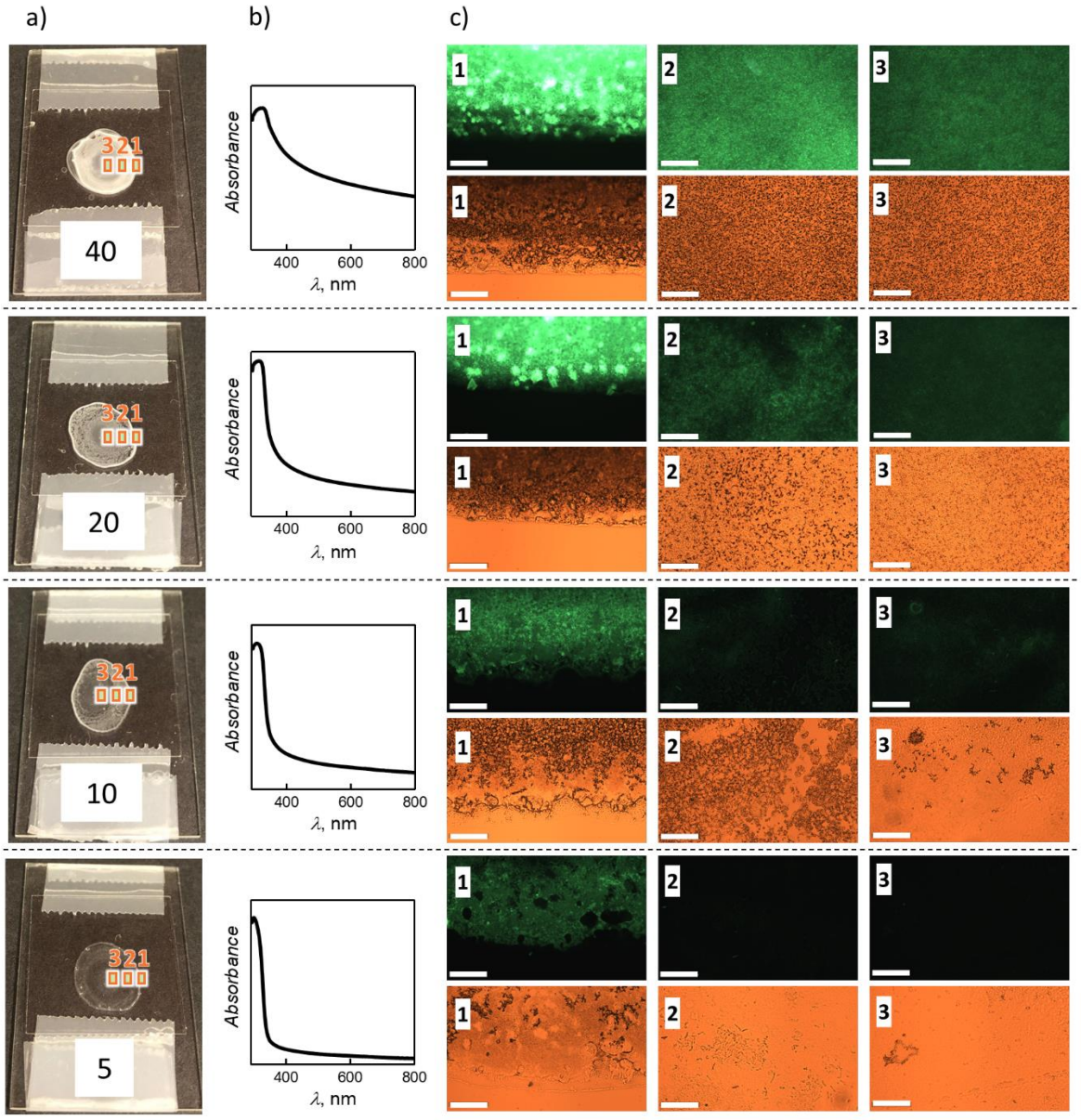

Figure S6. Concentration effect on the formation of hybrid films: the concentration of the UCNPs/[Tb_2] solutions were between 40 and 5 mg·mL^{-1} (for each moiety), while the UCNPs-to-[Tb_2] mass ratio was kept constant (1:1). a) Micrographs of the different films and b) corresponding absorption spectra. c)Bright-field and UV-excited micrographs taken on three different spots (indicated in a) of the film. For the sake of comparison, the excitation power and exposure time were kept constant when acquiring the micrograph under UV illumination. Scale bars in C are 100 μm.

8.5 Additional hyperspectral imaging of the UCNPs + [Tb2] hybrid system

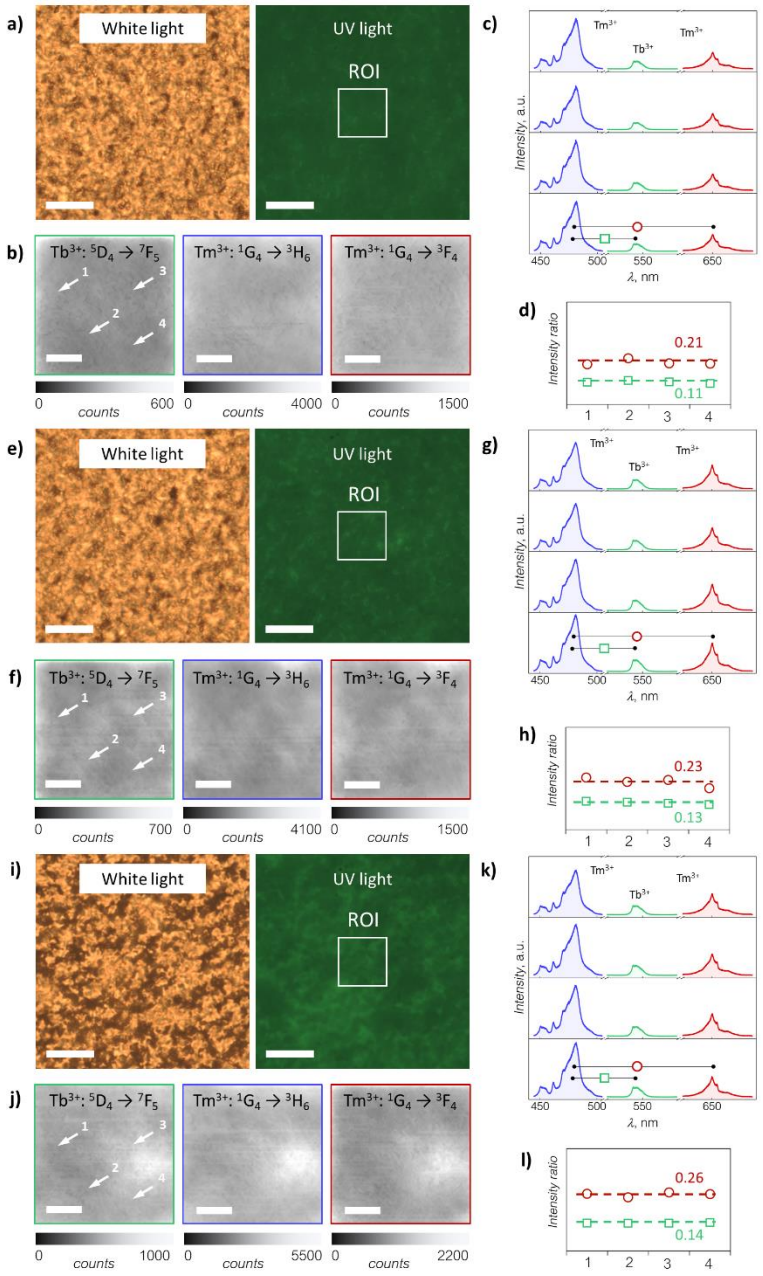

Figure S7. Hyperspectral mapping of three additional ROIs of a hybrid film (UCNPs+[Tb_2], concentration = 40 mg·mL-1, mass ratio was 1:1). a), e) and i) micrographs of the same film under white and UV light illumination along with ROI over which corresponding spectral maps b), f), i) were obtained (λex = 980 nm). Tm^{3+} and indirectly triggered Tb^{3+} emissions were monitored over an area of approximately 20 x 20 μm^2. The absolute intensities of the emission both UCNPs and the complex remained relatively constant within each ROI. It has to be mentioned that this film was prepared from a different batch of sub-10-nm UCNPs. Hence, the slight deviation of the ratio between the complex versus Tm^{3+}: $^1G_4 \rightarrow {}^3H_6$ (squares) and Tm^{3+}: $^1G_4 \rightarrow {}^3F_4$ versus Tm^{3+}: $^1G_4 \rightarrow {}^3H_6$ integrated emissions (circles) from the ones reported in Figure 44c-d is a consequence of unavoidable batch-to-batch variability in the properties of the UCNPs. Scale bars are 20 μm in the micrographs and 5 μm in ROI and spectral maps.

References

1 G. H. Dieke and H. M. Crosswhite, *Appl. Opt.*, 1963, **2**, 675.

2 J. C. G. Bünzli, *Trends Chem.*, 2019, **1**, 751–762.

3 J. Andres, R. D. Hersch, J. Moser and A. Chauvin, *Adv. Funct. Mater.*, 2014, **24**, 5029–5036.

4 J. E. Geusic, H. M. Marcos and L. G. Van Uitert, *Appl. Phys. Lett.*, 1964, **4**, 182–184.

5 K. T. Ranjit, I. Willner, S. H. Bossmann and A. M. Braun, *Environ. Sci. Technol.*, 2001, **35**, 1544–1549.

6 Z. Ahmed and K. Iftikhar, *RSC Adv.*, 2014, **4**, 63696–63711.

7 X. Wu, Y. Zhang, K. Takle, O. Bilsel, Z. Li, H. Lee, Z. Zhang, D. Li, W. Fan, C. Duan, E. M. Chan, C. Lois, Y. Xiang and G. Han, *ACS Nano*, 2016, **10**, 1060–1066.

8 E. Hemmer, P. Acosta-Mora, J. Méndez-Ramos and S. Fischer, *J. Mater. Chem. B*, 2017, **5**, 4365–4392.

9 J. Lee, B. Yoo, H. Lee, G. D. Cha, H. S. Lee, Y. Cho, S. Y. Kim, H. Seo, W. Lee, D. Son, M. Kang, H. M. Kim, Y. Il Park, T. Hyeon and D. H. Kim, *Adv. Mater.*, 2017, **29**, 1603169.

10 B. Jin, S. Wang, M. Lin, Y. Jin, S. Zhang, X. Cui, Y. Gong, A. Li, F. Xu and T. J. Lu, *Biosens. Bioelectron.*, 2017, **90**, 525–533.

11 S. Lahtinen, Q. Wang and T. Soukka, *Anal. Chem.*, 2016, **88**, 653–658.

12 F. Auzel, *Chem. Rev.*, 2004, **104**, 139–174.

13 R. Withnall and J. Silver, in *Handbook of Visual Display Technology*, eds. J. Chen, W. Cranton and M. Fihn, Springer Berlin Heidelberg, Berlin, Heidelberg, 1st edn., 2012, vol. 2, pp. 1019–1027.

14 H. C. Aspinall, *Chemistry of the f-Block Elements*, Routledge, Liverpool, 1st edn., 2018.

15 V. V Utochnikova and N. P. Kuzmina, *Russ. J. Coord. Chem.*, 2016, **42**, 679–694.

16 M. V. DaCosta, S. Doughan, Y. Han and U. J. Krull, *Anal. Chim. Acta*, 2014, **832**, 1–33.

17 Y. Il Park, J. H. Kim, K. T. Lee, K.-S. Jeon, H. Bin Na, J. H. Yu, H. M. Kim, N. Lee, S. H. Choi,

S.-I. Baik, H. Kim, S. P. Park, B.-J. Park, Y. W. Kim, S. H. Lee, S.-Y. Yoon, I. C. Song, W. K. Moon, Y. D. Suh and T. Hyeon, *Adv. Mater.*, 2009, **21**, 4467–4471.

18 R. T. Wegh, H. Donker, K. D. Oskam and A. Meijerink, *Science*, 1999, **283**, 663–6.

19 N. Bloembergen, *Phys. Rev. Lett.*, 1959, **2**, 84–85.

20 F. Auzel, *Comptes rendus Hebd. des séances l'Académie des Sci.*, 1966, **262**, 1016–1019.

21 M. Nyk, R. Kumar, T. Y. Ohulchanskyy, E. J. Bergey and P. N. Prasad, *Nano Lett.*, 2008, **8**, 3834–3838.

22 Y. Huang, E. Hemmer, F. Rosei and F. Vetrone, *J. Phys. Chem. B*, 2016, **120**, 4992–5001.

23 F. Huang, X. Liu, Y. Ma, S. Kang, L. Hu and D. Chen, *Sci. Rep.*, 2015, **5**, 8233.

24 F. Auzel, *Comptes rendus Hebd. des séances l'Académie des Sci.*, 1966, **263**, 819.

25 K. Binnemans, *Coord. Chem. Rev.*, 2015, 295, 1–45.

26 U. Rocha, C. Jacinto da Silva, W. Ferreira Silva, I. Guedes, A. Benayas, L. Martínez Maestro, M. Acosta Elias, E. Bovero, F. C. J. M. van Veggel, J. A. García Solé and D. Jaque, *ACS Nano*, 2013, **7**, 1188–1199.

27 O. Lehmann, H. Meyssamy, K. Kömpe, H. Schnablegger and M. Haase, *J. Phys. Chem. B*, 2003, **107**, 7449–7453.

28 M. C. Pujol, M. Rico, C. Zaldo, R. Solé, V. Nikolov, X. Solans, M. Aguiló and F. Díaz, *Appl. Phys. B*, 1999, **68**, 187–197.

29 A. Skripka, A. Benayas, R. Marin, P. Canton, E. Hemmer and F. Vetrone, *Nanoscale*, 2017, **9**, 3079–3085.

30 B. Chen, W. Kong, N. Wang, G. Zhu and F. Wang, *Chem. Mater.*, 2019, **31**, 4779–4786.

31 B. Amouroux, C. Roux, J. D. Marty, M. Pasturel, A. Bouchet, M. Sliwa, O. Leroux, F. Gauffre and C. Coudret, *Inorg. Chem.*, 2019, **58**, 5082–5088.

32 S. Bhuckory, E. Hemmer, Y.-T. Wu, A. Yahia-Ammar, F. Vetrone and N. Hildebrandt, *Eur. J. Inorg. Chem.*, 2017, **2017**, 5186–5195.

33 F. Vetrone, R. Naccache, V. Mahalingam, C. G. Morgan and J. A. Capobianco, *Adv. Funct.*

Mater., 2009, **19**, 2924–2929.

34 D. L. Dexter, *J. Chem. Phys.*, 1953, **21**, 836–850.

35 Z. Huang, Z. Xu, M. Mahboub, Z. Liang, P. Jaimes, P. Xia, K. R. Graham, M. L. Tang and T. Lian, *J. Am. Chem. Soc.*, 2019, **141**, 9769–9772.

36 R. Roy, S. Hohng and T. Ha, *Nat. Methods*, 2008, **5**, 507.

37 D. Beljonne, C. Curutchet, G. D. Scholes and R. J. Silbey, *J. Phys. Chem. B*, 2009, **113**, 6583–6599.

38 C. B. Murphy, Y. Zhang, T. Troxler, V. Ferry, J. J. Martin and W. E. Jones, *J. Phys. Chem. B*, 2004, **108**, 1537–1543.

39 L. Wang, Y. Zhang, A. Wu and G. Wei, *Anal. Chim. Acta*, 2017, **985**, 24–40.

40 R. Marin, I. Halimi, D. Errulat, Y. Mazouzi, G. Lucchini, A. Speghini, M. Murugesu and E. Hemmer, *ACS Photonics*, 2019, **6**, 436–445.

41 T. Hao, X. Wu, L. Xu, L. Liu, W. Ma, H. Kuang and C. Xu, *Small*, 2017, **13**, 1603944.

42 B. Ling, Y. Ma, H. Chen and L. Wang, *Anal. Methods*, 2017, **9**, 6032–6037.

43 C. Yan, A. Dadvand, F. Rosei and D. F. Perepichka, *J. Am. Chem. Soc.*, 2010, **132**, 8868–8869.

44 M. Haase and H. Schäfer, *Angew. Chemie - Int. Ed.*, 2011, **50**, 5808–5829.

45 H. Suo, X. Zhao, Z. Zhang, R. Shi, Y. Wu, J. Xiang and C. Guo, *Nanoscale*, 2018, **10**, 9245–9251.

46 C. Li, J. Yang, P. Yang, H. Lian and J. Lin, *Chem. Mater.*, 2008, **20**, 4317–4326.

47 E. Hemmer, Y. Kohl, V. Colquhoun, H. Thielecke, K. Soga and S. Mathur, *J. Phys. Chem. B*, 2010, **114**, 4358–4365.

48 E. Hemmer, M. Quintanilla, F. Légaré and F. Vetrone, *Chem. Mater.*, 2015, **27**, 235–244.

49 S. Heer, K. Kömpe, H. Güdel and M. Haase, *Adv. Mater.*, 2004, **16**, 2102–2105.

50 F. Zhao, M. Yuan, W. Zhang and S. Gao, *J. Am. Chem. Soc.*, 2006, **128**, 11758–11759.

51 Q. Ma and Q. Wang, *Displays*, 2015, **39**, 6–10.

52 N. Liu, R. Marin, Y. Mazouzi, G. O. Cron, A. Shuhendler and E. Hemmer, *Nanoscale*, 2019, **11**, 6794–6801.

53 R. Naccache, F. Vetrone, V. Mahalingam, L. A. Cuccia and J. A. Capobianco, *Chem. Mater.*, 2009, **21**, 717–723.

54 G.-S. Yi and G.-M. Chow, *Chem. Mater.*, 2007, **19**, 341–343.

55 H. X. Mai, Y. W. Zhang, R. Si, Z. G. Yan, L. D. Sun, L. P. You and C. H. Yan, *J. Am. Chem. Soc.*, 2006, **128**, 6426–6436.

56 F. Wang, Y. Han, C. S. Lim, Y. Lu, J. Wang, J. Xu, H. Chen, C. Zhang, M. Hong and X. Liu, *Nature*, 2010, **463**, 1061–1065.

57 F. Wang and X. Liu, *J. Am. Chem. Soc.*, 2008, **130**, 5642–5643.

58 B. Shen, S. Cheng, Y. Gu, D. Ni, Y. Gao, Q. Su, W. Feng and F. Li, *Nanoscale*, 2017, **9**, 1964–1971.

59 V. Mahalingam, F. Vetrone, R. Naccache, A. Speghini and J. A. Capobianco, *Adv. Mater.*, 2009, **21**, 4025–4028.

60 N. J. J. Johnson, W. Oakden, G. J. Stanisz, R. Scott Prosser and F. C. J. M. van Veggel, *Chem. Mater.*, 2011, **23**, 3714–3722.

61 C. Liu, Z. Gao, J. Zeng, Y. Hou, F. Fang, Y. Li, R. Qiao, L. Shen, H. Lei, W. Yang and M. Gao, *ACS Nano*, 2013, **7**, 7227–7240.

62 J. F.-C. Loo, Y.-H. Chien, F. Yin, S.-K. Kong, H.-P. Ho and K.-T. Yong, *Coord. Chem. Rev.*, 2019, **400**, 213042.

63 E. Hemmer, N. Venkatachalam, H. Hyodo, A. Hattori, Y. Ebina, H. Kishimoto and K. Soga, *Nanoscale*, 2013, **5**, 11339–11361.

64 E. Hemmer, A. Benayas, F. Légaré and F. Vetrone, *Nanoscale Horizons*, 2016, **1**, 168–184.

65 Q. Zhan, J. Qian, H. Liang, G. Somesfalean, D. Wang, S. He, Z. Zhang and S. Andersson-Engels, *ACS Nano*, 2011, **5**, 3744–3757.

66 F. Ai, Q. Ju, X. Zhang, X. Chen, F. Wang and G. Zhu, *Sci. Rep.*, 2015, **5**, 10785.

67 A. Skripka, V. Karabanovas, G. Jarockyte, R. Marin, V. Tam, M. Cerruti, R. Rotomskis and F. Vetrone, *Adv. Funct. Mater.*, 2019, **29**, 1807105.

68 V. P. Chauhan and R. K. Jain, *Nat. Mater.*, 2013, **12**, 958–962.

69 D. Glancy, Y. Zhang, J. L. Y. Wu, B. Ouyang, S. Ohta and W. C. W. Chan, *J. Control. Release*, 2019, **304**, 102–110.

70 Q. Sun, Z. Zhou, N. Qiu and Y. Shen, *Adv. Mater.*, 2017, **29**, 1606628.

71 R. Naccache, Q. Yu and J. A. Capobianco, *Adv. Opt. Mater.*, 2015, **3**, 482–509.

72 C. F. Gainer and M. Romanowski, *J. Innov. Opt. Health Sci.*, 2014, **07**, 1330007.

73 G. Yi, H. Lu, S. Zhao, Y. Ge, W. Yang, D. Chen and L.-H. Guo, *Nano Lett.*, 2004, **4**, 2191–2196.

74 N. Venkatachalam, Y. Saito and K. Soga, *J. Am. Ceram. Soc.*, 2009, **92**, 1006–1010.

75 J. C. Boyer, F. Vetrone, L. A. Cuccia and J. A. Capobianco, *J. Am. Chem. Soc.*, 2006, **128**, 7444–7445.

76 Z. Li and Y. Zhang, *Nanotechnology*, 2008, **19**, 345606.

77 V. K. LaMer and R. H. Dinegar, *J. Am. Chem. Soc.*, 1950, **72**, 4847–4854.

78 H. Wen, H. Zhu, X. Chen, T. F. Hung, B. Wang, G. Zhu, S. F. Yu and F. Wang, *Angew. Chemie Int. Ed.*, 2013, **52**, 13419–13423.

79 T. Rinkel, J. Nordmann, A. N. Raj and M. Haase, *Nanoscale*, 2014, **6**, 14523–14530.

80 N. Kang, C.-C. Ai, Y.-M. Zhou, Z. Wang and L. Ren, *Nanotechnology*, 2018, **29**, 075601.

81 T. Rinkel, A. N. Raj, S. Dühnen and M. Haase, *Angew. Chemie Int. Ed.*, 2016, **55**, 1164–1167.

82 F. Wang, R. Deng, J. Wang, Q. Wang, Y. Han, H. Zhu, X. Chen and X. Liu, *Nat. Mater.*, 2011, **10**, 968–973.

83 F. Wang, R. Deng and X. Liu, *Nat. Protoc.*, 2014, **9**, 1634–1644.

84 R. Gedye, F. Smith, K. Westaway, H. Ali, L. Baldisera, L. Laberge and J. Rousell, *Tetrahedron Lett.*, 1986, **27**, 279–282.

85 R. J. Giguere, T. L. Bray, S. M. Duncan and G. Majetich, *Tetrahedron Lett.*, 1986, **27**, 4945–4948.

86 C. O. Kappe, *Angew. Chemie Int. Ed.*, 2004, **43**, 6250–6284.

87 I. Bilecka and M. Niederberger, *Nanoscale*, 2010, **2**, 1358–1374.

88 J. P. Tierney and P. Lidström, *Microwave Assisted Organic Synthesis*, Blackwell Publishing Ltd,

Uppsala, Sweden, 1st edn., 2009.

89 S. A. Galema, *Chem. Soc. Rev.*, 1997, **26**, 233–238.

90 X. Wang, K. Qu, B. Xu, J. Ren and X. Qu, *J. Mater. Chem.*, 2011, **21**, 2445–2450.

91 F.-K. Liu, C.-J. Ker, Y.-C. Chang, F.-H. Ko, T.-C. Chu and B.-T. Dai, *Jpn. J. Appl. Phys.*, 2003, **42**, 4152.

92 Y. He, H. T. Lu, L. M. Sai, Y. Y. Su, M. Hu, C. H. Fan, W. Huang and L. H. Wang, *Adv. Mater.*, 2008, **20**, 3416–3421.

93 H.-Q. Wang and T. Nann, *ACS Nano*, 2009, **3**, 3804–3808.

94 M. Quintanilla, F. Ren, D. Ma and F. Vetrone, *ACS Photonics*, 2014, **1**, 662–669.

95 F. Guzzetta, A. Roig and B. Julián-López, *J. Phys. Chem. Lett.*, 2017, **8**, 5730–5735.

96 A. A. Gowen, C. P. O'Donnell, P. J. Cullen, G. Downey and J. M. Frias, *Trends Food Sci. Technol.*, 2007, **18**, 590–598.

97 X. Dong, M. Jakobi, S. Wang, M. H. Köhler, X. Zhang and A. W. Koch, *Appl. Spectrosc. Rev.*, 2019, **54**, 285–305.

98 M. D. P. S. Peña, A. Gottipati, S. Tahiliani, N. M. Neu-Baker, M. D. Frame, A. J. Friedman and S. A. Brenner, *Microsc. Res. Tech.*, 2016, **79**, 349–358.

99 M. B. Wabuyele, F. Yan, G. D. Griffin and T. Vo-Dinh, *Rev. Sci. Instrum.*, 2005, **76**, 63710.

100 T.-Y. Tseng, P.-J. Lai and K.-B. Sung, *Opt. Express*, 2011, **19**, 1291–1300.

101 J. R. Dunklin, G. T. Forcherio and D. K. Roper, *Mater. Res. Express*, 2015, **2**, 85005.

102 M. Mortimer, A. Gogos, N. Bartolomé, A. Kahru, T. D. Bucheli and V. I. Slaveykova, *Environ. Sci. Technol.*, 2014, **48**, 8760–8767.

103 A. Nadort, V. K. A. Sreenivasan, Z. Song, E. A. Grebenik, A. V Nechaev, V. A. Semchishen, V. Y. Panchenko and A. V Zvyagin, *PLoS One*, 2013, **8**, e63292.

104 R. Ilmi and K. Iftikhar, *Polyhedron*, 2015, **102**, 16–26.

105 H. Zhang, Y. Li, I. A. Ivanov, Y. Qu, Y. Huang and X. Duan, *Angew. Chemie - Int. Ed.*, 2010, **49**, 2865–2868.

106 E. Hemmer, N. Venkatachalam, H. Hyodo and K. Soga, *Adv. Mater. Sci. Eng.*, 2012, **2012**, 1–15.

107 I. Halimi, E. Martinazzo Rodrigues, S. L. Maurizio, T. Sun, M. Grewal, E. M. Boase, N. Liu, R. Marin and E. Hemmer, *J. Mater. Chem. C*, 2019, **7**, 15364–15374.

108 S. Dühnen, T. Rinkel and M. Haase, *Chem. Mater.*, 2015, **27**, 4033–4039.

109 K. L. Reddy, N. Prabhakar, R. Arppe, J. M. Rosenholm and V. Krishnan, *J. Mater. Sci.*, 2017, **52**, 5738–5750.

110 H. Eloussifi, J. Farjas, P. Roura, J. Camps, M. Dammak, S. Ricart, T. Puig and X. Obradors, *J. Therm. Anal. Calorim.*, 2012, **108**, 589–596.

111 S. Mishra and S. Daniele, *Chem. Rev.*, 2015, **115**, 8379–8448.

112 K. C. Patil, G. V Chandrashekhar, M. V George and C. N. R. Rao, *Can. J. Chem.*, 1968, **46**, 257–265.

113 V. K. LaMer, *Ind. Eng. Chem*, 1952, **44**, 1270–1277.

114 N. T. K. Thanh, N. Maclean and S. Mahiddine, *Chem. Rev.*, 2014, **114**, 7610–7630.

115 H.-X. Mai, Y.-W. Zhang, L.-D. Sun and C.-H. Yan, *J. Phys. Chem. C*, 2007, **111**, 13721–13729.

116 A. Stolow, A. E. Bragg and D. M. Neumark, *Chem. Rev.*, 2004, **104**, 1719–1757.

117 J. Bergstrand, Q. Liu, B. Huang, X. Peng, C. Würth, U. Resch-Genger, Q. Zhan, J. Widengren, H. Ågren and H. Liu, *Nanoscale*, 2019, **11**, 4959–4969.

118 C. Würth, S. Fischer, B. Grauel, A. P. Alivisatos and U. Resch-Genger, *J. Am. Chem. Soc.*, 2018, **140**, 4922–4928.

119 D. J. Gargas, E. M. Chan, A. D. Ostrowski, S. Aloni, M. V. P. Altoe, E. S. Barnard, B. Sanii, J. J. Urban, D. J. Milliron, B. E. Cohen and P. J. Schuck, *Nat. Nanotechnol.*, 2014, **9**, 300–305.

120 E. M. Rodrigues, D. A. Gálico, M. A. Lemes, J. Bettini, E. T. Neto, I. O. Mazali, M. Murugesu and F. A. Sigoli, *New J. Chem.*, 2018, **42**, 13393–13405.

121 N. Niu, F. He, S. Gai, C. Li, X. Zhang, S. Huang and P. Yang, *J. Mater. Chem.*, 2012, **22**, 21613–21623.

122 Y. Bao, Q. A. N. Luu, Y. Zhao, H. Fong, P. S. May and C. Jiang, *Nanoscale*, 2012, **4**, 7369–7375.

123 K. A. Abel, J.-C. Boyer and F. C. J. M. van Veggel, *J. Am. Chem. Soc.*, 2009, **131**, 14644–14645.

124 T. Cheng, R. Marin, A. Skripka and F. Vetrone, *J. Am. Chem. Soc.*, 2018, **140**, 12890–12899.

125 H. Dong, L. D. Sun and C. H. Yan, *Nanoscale*, 2013, **5**, 5703–5714.

126 M. Kaiser, C. Würth, M. Kraft, I. Hyppänen, T. Soukka and U. Resch-Genger, *Nanoscale*, 2017, **9**, 10051–10058.

127 R. Deng, J. Wang, R. Chen, W. Huang and X. Liu, *J. Am. Chem. Soc.*, 2016, **138**, 15972–15979.

128 D. Errulat, B. Gabidullin, M. Murugesu and E. Hemmer, *Chem. - A Eur. J.*, 2018, **24**, 10146–10155.

129 N. Bogdan, F. Vetrone, G. A. Ozin and J. A. Capobianco, *Nano Lett.*, 2011, **11**, 835–840.

130 J.-C. G. Buenzli, *Coord. Chem. Rev.*, 2015, **293**, 19–47.

131 M. Quintanilla, I. X. Cantarelli, M. Pedroni, A. Speghini and F. Vetrone, *J. Mater. Chem. C*, 2015, **3**, 3108–3113.

132 B. Tian, A. Fernandez-Bravo, H. Najafiaghdam, N. A. Torquato, M. V. P. Altoe, A. Teitelboim, C. A. Tajon, Y. Tian, N. J. Borys and E. S. Barnard, *Nat. Commun.*, 2018, **9**, 3082.

133 I. Medintz and N. Hildebrandt, *FRET - Förster Resonance Energy Transfer: From Theory to Applications*, John Wiley & Sons, 1st edn., 2013.

134 X. Wang, R. R. Valiev, T. Y. Ohulchanskyy, H. Ågren, C. Yang and G. Chen, *Chem. Soc. Rev. Chem. Soc. Rev*, 2017, **4150**, 4150–4167.

135 P. A. Rojas-Gutierrez, S. Bhuckory, C. Mingoes, N. Hildebrandt, C. DeWolf and J. A. Capobianco, *ACS Appl. Nano Mater.*, 2018, **1**, 5345–5354.

136 J.-C. Boyer, M.-P. Manseau, J. I. Murray and F. C. J. M. van Veggel, *Langmuir*, 2010, **26**, 1157–1164.

137 J. Zhao, J. Gao, W. Xue, Z. Di, H. Xing, Y. Lu and L. Li, *J. Am. Chem. Soc.*, 2018, **140**, 578–581.

138 D. Kong, Z. Quan, J. Yang, P. Yang, C. Li and J. Lin, *J. Nanoparticle Res.*, 2009, **11**, 821–829.

139 M. Wang, C.-C. Mi, W.-X. Wang, C.-H. Liu, Y.-F. Wu, Z.-R. Xu, C.-B. Mao and S.-K. Xu, *ACS Nano*, 2009, **3**, 1580–1586.

140 Z. Li, J. C. Barnes, A. Bosoy, J. F. Stoddart and J. I. Zink, *Chem. Soc. Rev.*, 2012, **41**, 2590–2605.

141 S. T. Selvan, *Biointerphases*, 2010, **5**, FA110–FA115.

142 J.-N. Liu, W.-B. Bu and J.-L. Shi, *Acc. Chem. Res.*, 2015, **48**, 1797–1805.

143 S. Jiang and Y. Zhang, *Langmuir*, 2010, **26**, 6689–6694.

144 R. Arppe, I. Hyppänen, N. Perälä, R. Peltomaa, M. Kaiser, C. Würth, S. Christ, U. Resch-Genger, M. Schäferling and T. Soukka, *Nanoscale*, 2015, **7**, 11746–11757.

145 L. F. Koao, H. C. Swart, R. I. Obed and F. B. Dejene, *J. Lumin.*, 2011, **131**, 1249–1254.

146 C. Liu, H. Wang, X. Li and D. Chen, *J. Mater. Chem.*, 2009, **19**, 3546–3553.

147 A. Kolate, D. Baradia, S. Patil, I. Vhora, G. Kore and A. Misra, *J. Control. Release*, 2014, **192**, 67–81.

148 C. D. Medley, S. Bamrungsap, W. Tan and J. E. Smith, *Anal. Chem.*, 2011, **83**, 727–734.